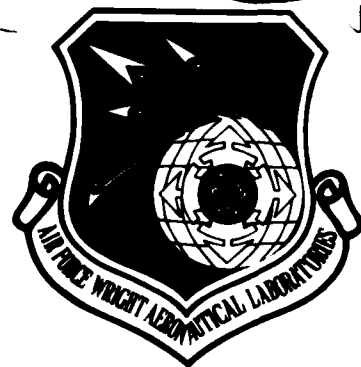


AFWAL-TR-80-2108

LEVEL II

2



ADA097141

AN EXPERIMENTAL AND NUMERICAL COMPARISON OF
TURBULENT FLOW OVER A STEP

ROBIN BREMMER
H. DOYLE THOMPSON
W. H. STEVENSON

SCHOOL OF MECHANICAL ENGINEERING
PURDUE UNIVERSITY
WEST LAFAYETTE, INDIANA 47907

DTIC
ELECTE
APR 01 1981
F

DECEMBER 1980

TECHNICAL REPORT AFWAL-TR-80-2108

Interim Technical report for period June 1978 - July 1980

Approved for public release; distribution unlimited.

AERO PROPULSION LABORATORY
AIR FORCE WRIGHT AERONAUTICAL LABORATORIES
AIR FORCE SYSTEMS COMMAND
WRIGHT-PATTERSON AIR FORCE BASE, OHIO 45433

DTIC FILE COPY

814 01 016

NOTICE

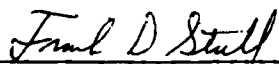
When Government drawings, specifications, or other data are used for any purpose other than in connection with a definitely related Government procurement operation, the United States Government thereby incurs no responsibility nor any obligation whatsoever; and the fact that the government may have formulated, furnished, or in any way supplied the said drawings, specifications, or other data, is not to be regarded by implication or otherwise as in any manner licensing the holder or any other person or corporation, or conveying any rights or permission to manufacture, use, or sell any patented invention that may in any way be related thereto.

This report has been reviewed by the Office of Public Affairs (ASD/PA) and is releasable to the National Technical Information Service (NTIS). At NTIS, it will be available to the general public, including foreign nations.

This technical report has been reviewed and is approved for publication.




Roger R. Craig
Project Engineer



Frank D. Stull, Chief
Ramjet Technology Branch
Ramjet Engine Division

FOR THE COMMANDER



E.T. Curran, Deputy Director
Ramjet Engine Division

"If your address has changed, if you wish to be removed from our mailing list, or if the addressee is no longer employed by your organization please notify AFWAL/PORT Attn: Roger Craig W-PAFB, OH 45433 to help us maintain a current mailing list".

Copies of this report should not be returned unless return is required by security considerations, contractual obligations, or notice on a specific document.

SECURITY CLASSIFICATION OF THIS PAGE (When Data Entered)

19. REPORT DOCUMENTATION PAGE		READ INSTRUCTIONS BEFORE COMPLETING FORM	
1. REPORT NUMBER	2. GOVT ACCESSION NO.	3. RECIPIENT'S CATALOG NUMBER	
AFWAL-TR-80-2108	AD-A097242		
4. TITLE (and Subtitle)		5. TYPE OF REPORT & PERIOD COVERED	
AN EXPERIMENTAL AND NUMERICAL COMPARISON OF TURBULENT FLOW OVER A STEP.		Interim Technical Report, June 1978-July 1980	
6. PERFORMING ORG. REPORT NUMBER		7. AUTHOR(s)	
		Robin J. Bremner, H. Doyle Thompson, and W. H. Stevenson	
8. CONTRACT OR GRANT NUMBER(s)		9. PERFORMING ORGANIZATION NAME AND ADDRESS	
F33615-77-C-2010		School of Mechanical Engineering Purdue University West Lafayette, Indiana 47907	
10. PROGRAM ELEMENT, PROJECT, TASK AREA & WORK UNIT NUMBERS		11. CONTROLLING OFFICE NAME AND ADDRESS	
2308-51-02		Aero Propulsion Laboratory (AFWAL/PORT) Air Force Wright Aeronautical Laboratories (AFSC) Wright-Patterson Air Force Base, Ohio 45433	
12. REPORT DATE		13. NUMBER OF PAGES	
December 1980		142	
14. MONITORING AGENCY NAME & ADDRESS (if different from Controlling Office)		15. SECURITY CLASS. (of this report)	
G-1001		UNCLASSIFIED	
15a. DECLASSIFICATION/DOWNGRADING SCHEDULE			
16. DISTRIBUTION STATEMENT (of this Report)			
Approved for public release; distribution unlimited			
17. DISTRIBUTION STATEMENT (of the abstract entered in Block 20, if different from Report)			
18. SUPPLEMENTARY NOTES			
19. KEY WORDS (Continue on reverse side if necessary and identify by block number)			
Turbulence measurements Laser velocimeter Recirculating flows Numerical analysis			
20. ABSTRACT (Continue on reverse side if necessary and identify by block number)			
An experimental investigation was made of air flow in a four inch square duct over a single four inch high rearward-facing step. The Reynolds number based on step height was 1.68×10^5 and the boundary layer approaching the step was turbulent. The pressure coefficient (C_p) distribution was found to be in relatively good agreement with similar measurements published in the literature. A laser Doppler velocimeter was used to measure an ensemble of 4500 individual velocities at angles of 0° , $+30^\circ$, and -30° to the duct axis from			

DD FORM 1 JAN 73 1473

EDITION OF 1 NOV 65 IS OBSOLETE
S/N 0102-014-6601

SECURITY CLASSIFICATION OF THIS PAGE (When Data Entered)

2975000

which the following mean velocities and turbulence parameters at 180 points in the flow field were derived: \bar{u} , \bar{v} , $\sqrt{\overline{u'^2}}$, $\sqrt{\overline{v'^2}}$, $\frac{1}{2}(\overline{u'^2} + \overline{v'^2})$, and $\overline{u'v'}$. The results, in general, compare favorably with those found in the literature. A two-dimensional numerical prediction of the flow field was made using the $k - \epsilon$ turbulence model. The comparison with the experimental results illustrates the three-dimensionality of the flow.

PPARC. EPSIL

PREFACE

This interim report was submitted by the School of Mechanical Engineering of Purdue University, under Contract No. F33615-77-C-2010 and covers the period 1 June 1978 - 31 July 1980. The effort was sponsored by the Aero Propulsion Laboratory, Air Force Wright Aeronautical Laboratories, Wright-Patterson AFB, Ohio under Project No. 2308 with Roger R. Craig/AFWAL/PORT as Project Engineer. Warren H. Stevenson and H. Doyle Thompson of Purdue University were technically responsible for the work.

Accession For	
NTIS GRA&I	<input checked="checked" type="checkbox"/>
DTIC TAB	<input type="checkbox"/>
Unannounced	<input type="checkbox"/>
Justification	
By	
Distribution/	
Availability Codes	
Dist	Avail and/or Special
A	

TABLE OF CONTENTS

	Page
I. INTRODUCTION	1
II. FLOW CHARACTERISTICS OF SUDDEN EXPANSIONS	2
1. Range of Past Experiments	2
2. Types of Separated Flow	5
3. Separated Flow Regions	13
4. Reattachment Length	18
a. Reynolds Number	19
b. Area Ratio	24
c. Aspect Ratio	27
d. Inlet Flow Conditions	30
5. Typical Flow Field Profiles	31
a. Mean Velocity Profiles	31
b. Turbulence Intensity Profiles	33
6. Pressure Distribution	37
7. Experimental Technique	39
8. Analytical Models of Sudden Expansions	43
III. EXPERIMENTAL APPARATUS	46
1. Flow System	46
2. Laser Doppler Velocimeter Optical System	52
3. Data Collection, Storage, and Processing System	59
IV. EXPERIMENTAL TECHNIQUE	63
1. Pressure Coefficient, C_p	63
2. Mean Velocity and Turbulence Parameters \bar{u} , \bar{v} , $\sqrt{\overline{u'^2}}$, $\sqrt{\overline{v'^2}}$, $\frac{1}{2}(\overline{u'^2} + \overline{v'^2})$, $\overline{u'v'}$	66
3. Stream Function, ψ	73
4. Reattachment Length, x_r	74
V. EXPERIMENTAL RESULTS	75

	Page
1. Pressure Coefficient, C_p	75
a. Pressure Coefficient Distribution	75
b. Experimental Error in C_p	79
2. Mean Velocities \bar{u} and \bar{v} and \bar{p} Streamwise Turbulence Intensity	80
a. Mean Streamwise Velocity, \bar{u}	80
b. Reattachment Length, x_r	85
c. Stream Function, ψ	85
d. Mean Transverse Velocity, \bar{v}	85
e. Streamwise Turbulence Intensity, $\sqrt{u'^2}/U_m$	88
3. Correlated Turbulence Parameters, $\sqrt{v'^2}/U_m$, $\frac{1}{2}(\overline{u'^2} + \overline{v'^2})$, $\overline{u'v'}$	90
4. Data Scatter due to Uncertainty in LDV Measurements	95
a. Single Measurement Error	95
b. Uncertainty in Ensemble Measurements	97
 VI. NUMERICAL ANALYSIS AND COMPARISON WITH EXPERIMENTAL RESULTS	 102
1. Background	102
2. Matching Reattachment Length	106
3. Mean Velocities	107
a. Numerical Results and Comparisons	107
b. Grid Dependence	115
4. Turbulence Parameters	119
a. Numerical Results and Comparisons	119
b. Grid Dependence	119
 VII. CONCLUSIONS AND RECOMMENDATIONS	 129
 REFERENCES	 131
 APPENDIX	 136

LIST OF TABLES

Table	Page
1. Details of previous axisymmetric annular step investigations	6
2. Details of previous two-dimensional single duct step investigations.	7
3. Details of previous two-dimensional double duct step investigations.	8
4. Details of previous two-dimensional single open channel step investigations.	8
5. Details of previous two-dimensional double open channel step investigations.	9
6. Details of previous two-dimensional surface step investigations.	10
7. Static pressure tap locations.	65
8. LDV system parameter settings.	67
9. Uncertainty in \bar{v} for 2 percent uncertainty in $(\bar{V})_\phi$	99
10. Uncertainty in $\overline{v'^2}$ for 4 percent uncertainty in $(\overline{V'^2})_\phi$	101
11. Conservation equations corresponding to Equation (23).	104
12. $k \sim \epsilon$ turbulence model constants from Ref. [31].	105

LIST OF ILLUSTRATIONS

Figure	Page
1. Sudden expansion models.	4
2. Separated flow regions	14
3. Secondary flow pattern in the separated flow region (from Goldstein et al. [10]).	17
4. Reattachment length vs. Reynolds number (from Back and Roschke [15])	20
5. Area ratio vs. reattachment length (from Abbott and Kline [11])	25
6. Aspect ratio vs. Reynolds number (from Cherdron et al. [22]).	29
7. Mean streamwise velocity profiles (from Cherdron, Durst, and Whitelaw [22]).	32
8. Mean streamwise velocity profiles (from Smyth [27]).	34
9. Streamwise turbulence intensity profiles (from Smyth [27]).	35
10. Turbulent kinetic energy and Reynolds stress profiles (from Smyth [27])	36
11. Pressure coefficient distribution (from Tani et al. [19]).	38
12. Pressure coefficient distribution (from Tani et al. [19] and Moss et al. [28])	40
13. Radial blade blower.	47
14. Flow system.	48
15. Flow conditioning section.	50

Figure		Page
16.	Test section.	50
17.	Static pressure tap detail.	51
18.	Particle generator system	53
19.	LDV optical system diagram.	54
20.	XYZ positioning system electronics.	58
21.	Data collection, storage, and processing system	60
22.	Data collection storage, and processing system schematic.	61
23.	Setup for measuring beam angle.	68
24.	Experimental grid	72
25.	Pressure coefficient distribution for flow over a two-dimensional single duct step.	76
26.	Comparison of measured pressure coefficients with Refs. [19] and [28]	78
27.	Measured streamwise velocity profiles	81
28.	\dot{m} vs. x/h	82
29.	Measured spanwise velocity profiles	84
30.	Measured stream function contours	86
31.	Experimental velocity vector plot	87
32.	Measured streamwise turbulence intensity profiles	89
33.	Measured transverse turbulence intensity profiles	91
34.	Measured turbulent kinetic energy profiles.	92
35.	Measured turbulent kinetic energy contours.	93
36.	Measured Reynolds stress profiles	94
37.	Measured Reynolds stress contours	96
38.	Turbulent dissipation rate coefficient, C_2 , vs. reattachment length	108

Figure	Page
39. Calculated streamwise velocity profiles.	109
40. Calculated stream function contours.	110
41. Calculated velocity vector plot.	111
42. Comparison of calculated and measured streamwise velocity profiles at $x/h = 2$	112
43. Comparison of calculated and measured streamwise velocity profiles at $x/h = 4$	113
44. Comparison of calculated and measured streamwise velocity profiles at $x/h = 8$	114
45. Grid dependence for calculated streamwise velocity profiles at $x/h = 1.0$	116
46. Grid dependence for calculated streamwise velocity profiles at $x/h = 5.0$	117
47. Grid dependence for calculated streamwise velocity profiles at $x/h = 10.0$	118
48. Calculated turbulent kinetic energy profiles	120
49. Calculated turbulent kinetic energy contours	121
50. Comparison of calculated and measured turbulent kinetic energy profiles at $x/h = 2.0$	122
51. Comparison of calculated and measured turbulent kinetic energy profiles at $x/h = 4.0$	123
52. Comparison of calculated and measured turbulent kinetic energy profiles at $x/h = 8.0$	124
53. Grid dependence for calculated turbulent kinetic energy profiles at $x/h = 1.0$	125
54. Grid dependence for calculated turbulent kinetic energy profiles at $x/h = 5.0$	126
55. Grid dependence for calculated turbulent kinetic energy profiles at $x/h = 10.0$	127
A-1. Probe volume geometry.	137
A-2. Flow system geometry	137

NOMENCLATURE

A	$1/F_R$
A_R	Area ratio
b	Width of free shear layer
C_1, C_2, C_3	Turbulence constants
C_p	Pressure coefficient
D	Diameter downstream of an axisymmetric annular step
D_m	Digital mantissa
D_o	Diameter upstream of an axisymmetric annular step
\hat{e}_1, \hat{e}_2	Unit vectors along incident intersecting beams
\hat{e}_n	Unit vector normal to bisector and in the plane of incident intersecting beams
\hat{e}_t	Unit vector tangent to bisector and in the plane of incident intersecting beams
$\hat{e}_x, \hat{e}_y, \hat{e}_z$	Unit vectors in the x, y, and z directions
E	Constant in the log-law, = 9.0 for smooth walls
f	$\bar{f} + f'$, measured Doppler frequency
F_R	Fringe spacing
f_s	Frequency shift
G_k	See Table 11
h	Step height
k	$\frac{1}{2}(\overline{u'^2} + \overline{v'^2})$, turbulent kinetic energy (two-dimensional)
L	Length in streamwise direction
\dot{m}	Mass flow rate

M	Mach number
n	Refractive index of medium
n	Exponent on TSI processor
N	Number of cycles/burst on TSI processor
p	Pressure
P	Static pressure
P_0	Upstream (reference) static pressure
r	Cylindrical coordinate
Re_b	Reynolds number based on b
Re_{δ^*}	Reynolds number based on δ^*
$Re_{\delta_S^*}$	Reynolds number based on δ_S^*
Re_{D_0}	Reynolds number based on D_0
Re_h	Reynolds number based on h
S_ϕ	Source term for variable ϕ
u	$\bar{u} + u'$, instantaneous streamwise velocity
$\overline{u'v'}$	Reynolds stress
U_m	Mean inlet velocity
U_{max}	Maximum \bar{u} in inlet profile
U_0	Upstream (reference) mean streamwise velocity
v	$\bar{v} + v'$, instantaneous transverse velocity
V	$\bar{V} + V'$, instantaneous velocity
V	$u\hat{e}_x + v\hat{e}_y + w\hat{e}_z$, total instantaneous velocity vector
w	$\bar{w} + w'$, instantaneous cross-stream velocity
W	Uncertainty
W_0	Channel width or duct height upstream of step
W_1	Channel width or duct height downstream of step

x	Streamwise coordinate direction
x_r	Reattachment length
x_{r1}	Shorter reattachment length in plane asymmetric flows
x_{r2}	Longer reattachment length in plane asymmetric flows
y	Transverse coordinate
y_1	Vertical distance from wall
z	Cross-stream coordinate

Greek Symbols

Γ	Exchange coefficient
δ	Boundary layer thickness
δ_s	Boundary layer thickness at point of separation
δ^*	Boundary layer displacement thickness
δ_s^*	Boundary layer displacement thickness at point of separation
ΔP	$P - P_o$
ϵ	Rate of dissipation of turbulent kinetic energy (k)
θ	Angle between incident intersecting beams
κ	Constant in the log-law, = 0.4
λ	Wavelength of laser light
μ_{lam}	Laminar viscosity
μ_t	Turbulent viscosity
μ_{eff}	$\mu_{lam} + \mu_t$, effective viscosity
ρ	Fluid density
σ	Standard deviation
σ_ϵ	Turbulent Prandtl number for ϵ
σ_k	Turbulent Prandtl number for k

τ_w	Wall shear stress
ϕ	Angle of rotation of the optical system about its axis
Φ	A general variable
ψ	Stream function
ψ_{TOP}	Stream function at top wall of grid line
ψ^*	ψ/ψ_{TOP} , non-dimensionalized stream function

Math Symbols

\sum	Summation
$\frac{\partial}{\partial x}, \frac{\partial}{\partial r}$	Space derivatives
$\frac{\partial}{\partial t}$	Time derivative
\int	Integral
$\overline{\quad},'$	Time average and its fluctuation quantity

Subscripts

$[\]_\phi$	Quantity evaluated at rotation angle ϕ
--------------	---

SECTION I

INTRODUCTION

The primary objective of this research program is to investigate the application of laser Doppler velocimetry to turbulent and mixing flows. Of particular interest is the mapping of the flow field in a cold flow model of a dump combustor (sudden expansion). The flow field characteristics of a dump combustor in the present study are modeled by a two-dimensional single duct step.

The subject of this report is the flow field characteristics of a two-dimensional single duct step measured with a laser-Doppler velocimeter and predicted by a numerical model. The general flow characteristics of sudden expansions are reviewed in Section II. Sections III, IV, and V describe the apparatus, techniques and results of the experimental measurements. Presentation of the numerical model as well as a discussion of experimental and analytical results is given in Section VI. Final conclusions and recommendations are given in Section VII.

SECTION II

FLOW CHARACTERISTICS OF SUDDEN EXPANSIONS

Separated flow is a very common type of flow found in everyday engineering practice. It occurs on aerofoils with large angles of attack, in wide-angle diffusers, over cylinders and bluff bodies, and in sudden expansions. A sudden expansion is typical of piping systems where flow separation can not be avoided and is a nuisance as it causes increased pressure loss. A dump combustor on the other hand, uses a sudden expansion to create a recirculation zone which is used as a flameholder and is critical to the overall combustion process. Certainly the general flow characteristics of sudden expansions are of engineering interest and have been the center of many recent experimental and analytical investigations.

The investigations reported in the literature have found that both geometrical parameters and inlet flow conditions have a significant effect on the flow field of sudden expansions. The purpose of this section is to describe how these variables influence the flow field of sudden expansions. It is also within the scope of this section to identify some of the relevant mechanisms responsible for the character of the flow field.

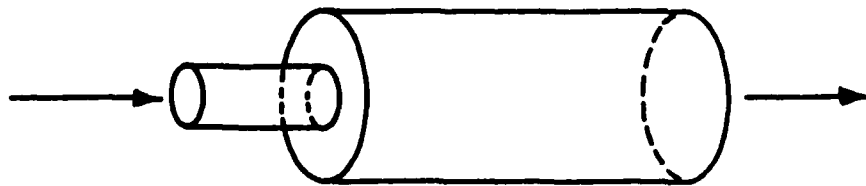
1. Range of Past Experiments

A wide range of instruments have been used by investigators to obtain qualitative as well as quantitative information about sudden

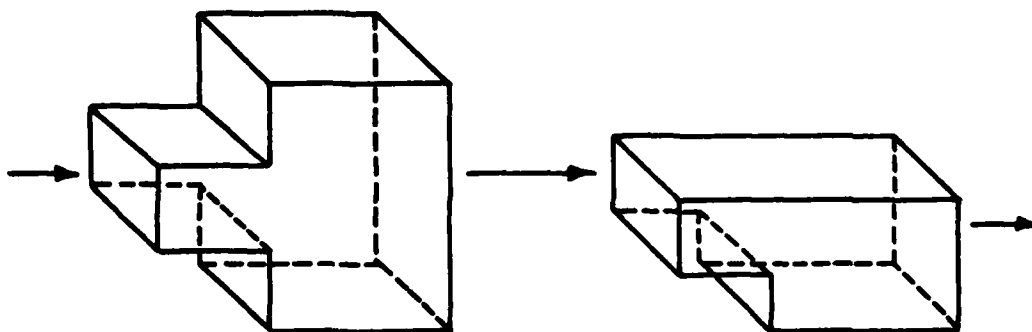
expansions. Pitot tubes, pressure taps, hot wires, and laser Doppler velocimeters have been the major quantitative instruments used. Various flow visualization techniques including smoke and dye studies have been used. Numerical solutions of the governing equations have provided qualitative, and in some instances quantitative information. Air and water have been the basic fluids used, with some work done with combustion gases. Reynolds numbers typically studied range from 10 to 10^7 based on average inlet velocity and inlet diameter. The boundary layer at the point of separation has been either laminar or turbulent. Supersonic sudden expansion flows have been examined [1,2,3] but will not be included in the discussions of this chapter.

Various models have been used to simulate sudden expansions. The four basic types are: (1) axisymmetric annular step, (2) two-dimensional duct step, (3) two-dimensional open channel step, and (4) two-dimensional surface step. Both (2) and (3) can be either of the single or double step type as shown in Figure 1. Two-dimensional surface steps are typically found in wind tunnel studies as a stepped flat plate where the wall opposite the step is a significant distance away. Other bluff body models as well as combustion models have been used but will not be included in this discussion.

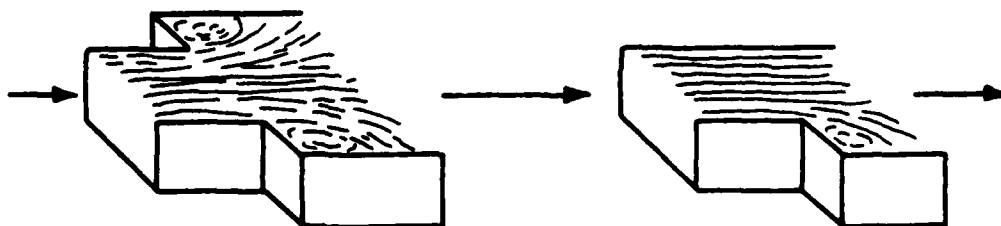
-
- [1] Bowyer Jr., J.M., and Carter, W.V., "Separated Flow Behind a Rearward-Facing Step with and without Combustion," AIAA Journal, Vol. 3, No. 1, pp. 181-183, January, 1965.
 - [2] Burggraf, O.R., "Computational Study of Supersonic Flow over Backward-Facing Steps at High Reynolds Number, ARL-70-0257, Aerospace Research Laboratories, Wright-Patterson Air Force Base, Ohio, November, 1970.
 - [3] Sfeir, A., "Supersonic Flow Separation on a Backward Facing Step," University of California, Berkeley, Report No. AS-66-18, December, 1966.



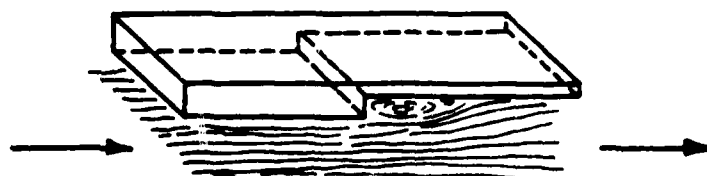
(1) Axisymmetric Annular Step



(2) Two-Dimensional Duct Step



(3) Two-Dimensional Open Channel Step



(4) Two-Dimensional Surface Step

Figure 1. Sudden expansion models.

Tables 1 through 6 are a compilation of recent investigations on the various sudden expansion models. These are certainly not complete lists but include those studies pertinent to this discussion. Included in Tables 1 through 6 are the technique(s), fluid(s), and velocity characteristic of that particular experiment. As will be discussed later in this section, the step height h , or the corresponding area ratio A_R , is an important parameter affecting the flow field and is also included in Tables 1 through 6.

2. Types of Separated Flow

Chapman, Kuehn, and Larson [4] emphasized that three types of separated flows can occur: laminar, transitional, and turbulent. Laminar separated flow occurs when a laminary boundary layer separates and reattaches as a laminar boundary layer. Transitional separated flow finds transition to turbulence occurring after separation but before reattachment. Hence a turbulent boundary layer grows immediately after reattachment. Turbulent separated flow occurs when a turbulent boundary layer separates and reattaches as a turbulent boundary layer.

Owen and Klanfer [5] proposed a simple criterion for determining whether a laminar boundary layer will reattach as a laminar boundary layer or will undergo transition and reattach as a turbulent boundary layer. Their criterion states that if $Re_{\delta_s}^*$ (Reynolds number based on

-
- [4] Chapman, D.R., Kuehn, D.M., and Larson, H.K., "Investigation of Separated Flows in Supersonic and Subsonic Streams with Emphasis on the Effect of Transition," NACA TN-3869, 1957.
 - [5] Owen, P.R., and Klanfer, L., "On the Laminar Boundary Layer Separation From the Leading Edge of a Thin Aerofoil," Royal Aircraft Establishment Report No. Aero. 2508, October, 1953.

Table 1. Details of previous axisymmetric annular step investigations.

Model: Axisymmetric annular step					
Year	Author(s)	Technique(s)	Fluid(s)	Velocity	h or A_R
1967	Macagno and Hung [13]	numerical, aluminum powder visualization	oil	$36 \leq Re_{D_0} \leq 4500$	$A_R = 2$
1972	Back and Roschke [15]	dye studies	water	$20 \leq Re_{D_0} \leq 4500$	$A_R = 2.6$
1974	Teyssandier and Wilson [29]	numerical	air	$Re_b = 114$	$1.43 \leq A_R \leq 3.33$
1975	Freeman [46]	LDV	water	$Re_{D_0} = 3 \times 10^4$	$A_R = 2.1$
1977	Gosman, Khali and Whitelaw [33]	numerical	air	$Re_{D_0} = 5 \times 10^4$	$A_R = 2.6$
1977	Moon and Rudinger [26]	numerical, LDV	air	40 - 90 mps	$A_R = 1.43$
1978	Drewry [47]	pressure taps, gas-sampling, oil visualization	air	450 - 1010 fps	$A_R = 1.28, 1.536, 1.92$
1979	Kangovi and Page [48]	pressure taps, Pitot tube, hot wire	air	$0.12 \leq M \leq 0.95$	$h = 0.6, 1.3, 1.9, 2.5 \text{ cm}$

Table 2. Details of previous two-dimensional single duct step investigations.

Model: 2-D single duct step					
Year	Author(s)	Technique(s)	Fluid(s)	Velocity	h or A_R
1970	Goldstein, Erickson, Olson, and Eckert [10]	hot wire, smoke studies	air	0.61 - 2.44 mps	$0.36 \text{ cm} < h \leq 1.02 \text{ cm}$
1972	Bradshaw and Wong [49]	Pitot tube, Preston tube, hot wire	air	25 mps	$A_R = 1.4$
1974	Durst, Melling and Whitelaw [12]	LDV, smoke studies	air	$Re_h = 56, 114, 252$	$A_R = 3$
1977	Gosman, Khalil, and Whitelaw [33]	numerical	air	$Re_{W_0} = 5 \times 10^4$	$1.125 \leq A_R \leq 2.5$
1977	Davies and Snell [25]	hot wire	air	$Re_{W_0} = 1 \times 10^5$	$h = 5, 7.5 \text{ cm}$
1979	Eaton, Johnston, and Jeans [17]	Pitot tube, thermal tuft	air	13 mps	$h = 5.08 \text{ cm}$

Table 3. Details of previous two-dimensional double duct step investigations.

Model: 2-D double duct step					
Year	Author(s)	Technique(s)	Fluid(s)	Velocity	h or A_R
1978	Cherdron, Durst, and Whitelaw [22]	LDV, oil visualization, smoke studies	air	$110 \leq Re_h < 500$	$A_R = 2, 3$
1978	Restivo and Whitelaw [50]	LDV	air	$494 \leq Re_{W_0} < 2995$	$A_R = 3$

Table 4. Details of previous two-dimensional single open channel step investigations.

Model: 2-D single open channel step					
Year	Author(s)	Technique(s)	Fluid(s)	Velocity	h or A_R
1962	Abbott and Kline [11]	hot film, dye studies	water	$2 \times 10^4 \leq Re_{W_0}$ $\leq 5 \times 10^4$	$1.25 \leq A_R \leq 5$
1978	Etheridge and Kemp [26]	LDV, aluminum powder visualization	water	-----	$h = 1.3 \text{ cm}$

Table 5. Details of previous two-dimensional double open channel step investigations.

Model: 2-D double open channel step					
Year	Author(s)	Technique(s)	Fluid(s)	Velocity	h or A_R
1962	Abbott and Kline [11]	hot film, dye studies	water	$2 \times 10^4 \leq Re_{W_0}$	$1.25 \leq A_R \leq 5$
1976	Smyth [51]	LDV	water	0.49 mps	$A_R = 3$
1979	Smyth [27]	LDV	water	$Re_{W_1} = 30, 210$	$A_R = 1.5$

Table 6. Details of previous two-dimensional surface step investigations.

Model: 2-D surface step					
Year	Author(s)	Technique(s)	Fluid(s)	Velocity	h or A_R
1959	Seban, Emery, and Levy [18]	impact and static tubes, pressure taps, thermocouples	air	150 - 500 fps	$h = 0.25, 0.81$ in.
1960	Moore [8]	Pitot-static tubes, pressure taps, liquid film, smoke studies	air	32 - 50 fps	$h = 0.060, 0.138$ in.
1961	Tani, Iuchi, and Komoda [19]	Pitot tubes, pressure taps, hot wire, aluminum powder visualization	air, water	10, 16, 22, and 28 mps	$h \leq 6$ cm
1965	Roshko and Lau [9]	Pitot tube, pressure	air	29.5 fps	$h = 0.034$ in.
1977	Moss, Baker, and Bradbury [28]	pulsed-wire anemometer, pressure taps	air	$Re_h = 5 \times 10^4$	$h = 7.6$ cm

δ_s^* , the boundary layer displacement thickness at the point of separation) is greater than 400-500, the flow is transitional. For a flat plate in parallel flow at zero incidence, $Re_{\delta_s^*,crit}$ (Reynolds number, based on δ_s^* , at which a laminar boundary begins transition to a turbulent boundary layer) is approximately 950. Crabtree [6] gave a physical explanation for this type of separated flow on the basis of Schubauer and Klebanoff's [7] condition for the growth of turbulent spots in a boundary layer. He proposed that Owen and Klanfer's critical value determined whether turbulent spots would grow in the shear layer thus provoking transition to turbulence, or that their failure to grow would allow laminar reattachment. This argument can not be substantiated as turbulent spots have yet to be identified as a mechanism in free shear layers. Vortex shedding and interaction appear to be the prime mechanisms that occur in free shear layers. Moore's [8] experimental results supported Crabtree's interpretation of Owen and Klanfer's critical value. Moore, using a Pitot-static tube for traversing the boundary layer, found that laminar boundary layer growth downstream of a two-dimensional surface step occurred for values of $Re_{\delta_s^*}$ less than 500. Turbulent boundary layer growth occurred for $Re_{\delta_s^*}$ greater than 500.

-
- [6] Crabtree, L.F., "Effects on Leading-Edge Separation on Thin Wings in Two-Dimensional Incompressible Flow," Journal of the Aeronautical Sciences, Vol. 24, No. 8, pp. 597-604, August, 1957.
 - [7] Schubauer, G.B., and Klenbanoff, P.S., "Contributions to the Mechanics of Boundary Layer Transition," NACA TN-3489, 1955.
 - [8] Moore, T.W.F., "Some Experiments on the Reattachment of a Laminar Boundary Layer Separating From a Rearward Facing Step on a Flat Plate Aerofoil," Journal of the Royal Aeronautical Society, Vol. 64, pp. 668-672, November, 1960.

Moore's results, however, were based solely upon the shape of the mean velocity profile.

Roshko and Lau [9] used a surface Pitot tube and hot wire in their investigation of the shear layer following a two-dimensional surface step. Transition to turbulence occurred before reattachment in all cases. However, they predicted on the basis of their data and analysis that the criterion for laminar reattachment is $\delta_s/h \geq 1$, where δ_s is the boundary layer thickness at the point of separation. For a Blasius profile at the step, this requirement can be written as $\delta_s^*/h \geq 0.34$. From this requirement it can be seen that it is impossible to have laminar separated flow when the shear layer thickness is small compared to the step height. Goldstein, Erickson, Olson, and Eckert [10] felt that this criterion agreed closely with their data but was not sufficient. Their hot wire results showed that the criterion for laminar reattachment included not only $\delta_s^*/h \geq 0.4$ but also that Re_h (Reynolds number based on step height h) must be less than 520 with the stipulation that both conditions be met simultaneously.

The criterion of Goldstein et al. [10] appears to be the most accurate of those mentioned for determining whether reattachment is laminar or transitional. The applicability of their criterion would include both two-dimensional single duct step models and two-dimensional

[9] Roshko, A., and Lau, J.C., "Some Observations on Transition and Reattachment of a Free Shear Layer in Incompressible Flow," Proceedings of the 1965 Heat Transfer and Fluid Mechanics Institute, edited by A.F. Charwat, Stanford University Press, Stanford, pp. 157-167.

[10] Goldstein, R.J., Erickson, V.L., Olson, R.M., and Eckert, E.R.G., "Laminar Separation, Reattachment, and Transition of the Flow Over a Downstream-Facing Step," Journal of Basic Engineering, Vol. 92, pp. 732-741, December, 1970.

surface step models. Applying this criterion to other models would be speculative as investigative results remain incomplete. Moore [8] stated that one of his runs "displays profiles which are more consistent with the notion that the boundary layer has reattached while still in the laminar state." Goldstein et al. pointed out that if the boundary layer in Moore's test grew as though it were on a flat plate, the values of Re_h and δ_s^*/h would be 800 and 0.425, respectively. These values fall outside their range of laminar regime and indicate that Moore's run probably does not represent steady, laminar separated flow, but rather is transitional. Laminar flow reattaching as turbulent flow is not usually discernible just from mean velocity profiles; both visual observations and turbulent intensity measurements give a more complete picture. Since Moore only made mean velocity measurements with a Pitot-static tube, it is probable that the observations of Goldstein et al. are valid.

3. Separated Flow Regions

Abbott and Kline's [11] dye studies showed that the recirculation zone found in sudden expansions was not "dead" as described by Moore [8] but was complex in nature and could be characterized by three distinct regions as shown in Figure 2. The three regions are:

[11] Abbott, D.E., and Kline, S.J., "Experimental Investigation of Subsonic Flow Over Single and Double Backward Facing Steps," Journal of Basic Engineering, Vol. 84, pp. 317-325, September, 1962.

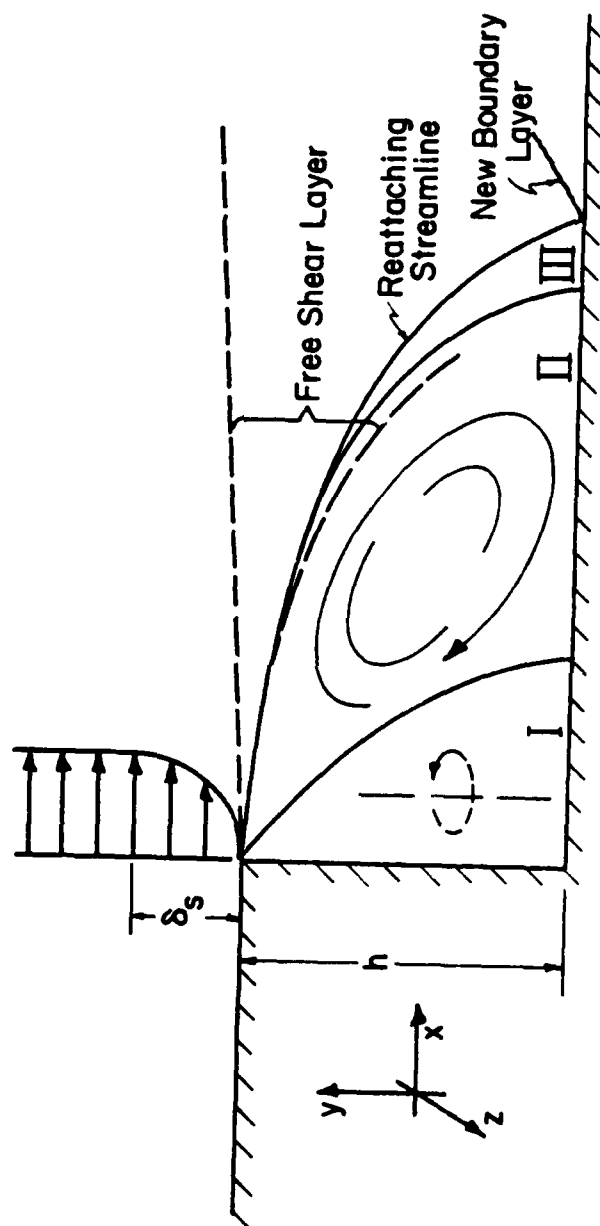


Figure 2. Separated flow regions.

(I) A three-dimensional region of separation characterized by one or more vortices rotating about an axis parallel to the y-axis. Although three-dimensional in space, these vortices can change size with respect to time. Vortices adjacent to one another can be of different size and are counter-rotating. The number of vortices varies, depending on the step geometry.

(II) A two-dimensional region containing the classic pattern of separation; trapped eddies with axes parallel to the z-axis. Maximum velocities in this region are approximately one-fifth the freestream velocity upstream of the step.

(III) The reattachment region where bifurcation of the shear layer occurs and part of the flow is deflected upstream into region (II) to supply entrainment. Basically, the part of the shear layer that does not have enough momentum to overcome the pressure rise associated with reattachment is turned upstream to form the recirculation region. Downstream of the reattachment point a new boundary layer begins, whether it be laminar or turbulent.

When the separated flow is of the transitional or turbulent type, regions (I), (II), and (III) are maintained in equilibrium such that the pressures exerted by the solid surfaces are balanced by the turbulent shear stress which is set up in the mixing region.

Although these regions were identified by Abbott and Kline [11] for turbulent flow in a two-dimensional open channel, other investigators have either specifically identified these regions or noted their

effects for laminar flow in sudden expansions. Durst, Melling, and Whitelaw [12] related their observed three-dimensional streamlines within the separation region for laminar flow to the presence of corner vortices similar to those described by Abbott and Kline. They utilized smoke injection for a two-dimensional single duct step. Goldstein et al. [10] observed that for the laminar case, smoke injected through the side wall of the test section just upstream of a two-dimensional single duct step entered the separation region and recirculated in a spiral like fashion. It then left the separated zone in the plane of the centerline as shown in Figure 3. However, smoke introduced in the plane of the centerline remained in that plane. If that pattern also applied to the turbulent separated flow case it could account for Abbott and Kline's characterization of region II as two-dimensional.

Axisymmetric annular step investigations have shown the occurrence of regions II and III. Region I, however, has yet to be identified. This is probably due to the self-correcting geometry of the axisymmetric annular step. In a laminar flow study, Macagno and Hung [13] showed that symmetric flow patterns are maintained over a range of Reynolds number for axisymmetric annular steps. Future discussion will show that symmetric flow patterns (equal reattachment lengths) are not always prevalent for plane flows. In the axisymmetric case

[12] Durst, F., Melling, A., and Whitelaw, J.D., "Low Reynolds Number Flow Over a Plane Symmetric Sudden Expansion," Journal of Fluid Mechanics, Vol. 64, pt. 1, pp. 111-128, 3 June, 1974.

[13] Macagno, E.D., and Hung, T.K., "Computational and Experimental Study of a Captive Annular Eddy," Journal of Fluid Mechanics, Vol. 28, pt. 1, pp. 43-64, 12 April, 1967.

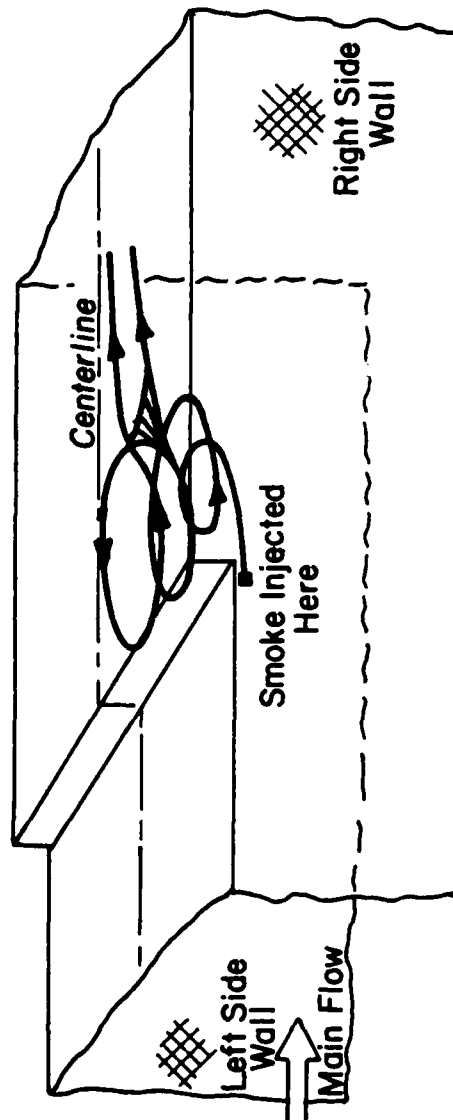


Figure 3. Secondary flow pattern in the separated flow region (from Goldstein et al. [10]).

there is only a single, annular separation region. Asymmetric flow would cause a local change in pressure distribution in the separation region. This would be offset by a redistribution of pressure within the separation region, hence a symmetric flow field. Nevertheless, asymmetric flow patterns were reported by Zemanick and Dougall [14] for turbulent flow in an axisymmetric annular expansion. However, the extent of asymmetry was small when compared with that in a plane expansion.

The type of pressure correcting mechanism found in axisymmetric flows does not exist in plane flows as long as the separation regions are disconnected. No conclusive evidence has been presented of pressure distribution mechanisms acting through interacting shear layers.

4. Reattachment Length

The streamwise distance between the point of separation and reattachment for flow through sudden expansions has been the subject of many investigations. Functional relationships between reattachment length and Reynolds number, area ratio, aspect ratio, and inlet flow conditions have been postulated and are presented in this section.

-
- [14] Zemanick, P.P., and Dougall, R.S., "Local Heat Transfer Downstream of an Abrupt Circular Channel Expansion," ASME Journal of Heat Transfer, Vol. 92, pp. 53-60, February, 1970.

a. Reynolds Number

Back and Roschke [15] experimentally investigated the reattachment lengths for water flow through an axisymmetric annular step for a Reynolds number (Re_D) range of 20 to 4200. Their dye study results, presented in Figure 4, show that laminar, transitional, and turbulent separated flow occur over this Reynolds number range with the reattachment length varying significantly. The laminar separated flow reattachment point increases in length with increasing Reynolds number until the transitional separated flow effects become influential. In turbulent separated flow the reattachment length is fairly constant. The transitional flow simply acts as an interface between the other two types of flow.

The laminar separated flow reattachment point moved downstream with increasing Reynolds number as would be expected if the free shear layer spread by diffusion. According to Back and Roschke's [15] data, the maximum reattachment point occurred approximately 25 step heights downstream. Cramer [16], in an attempt to obtain a theoretical basis for this phenomenon, assumed the flow downstream of a stepped flat plate grew toward the wall like a spreading laminar jet. He further assumed that the flow was incompressible, the step height was small,

-
- [15] Back, L.H., and Roschke, E.J., "Shear-Layer Flow Regimes and Wave Instabilities and Reattachment Lengths Downstream of an Abrupt Circular Channel Expansion," ASME Journal of Applied Mechanics, Vol. 94E, pp. 677-681, September, 1972.
- [16] Cramer, K.R., "On Laminar Separation Bubbles," Journal of the Aeronautical Sciences, Vol. 25, No. 2, pp. 143-144, February, 1958.

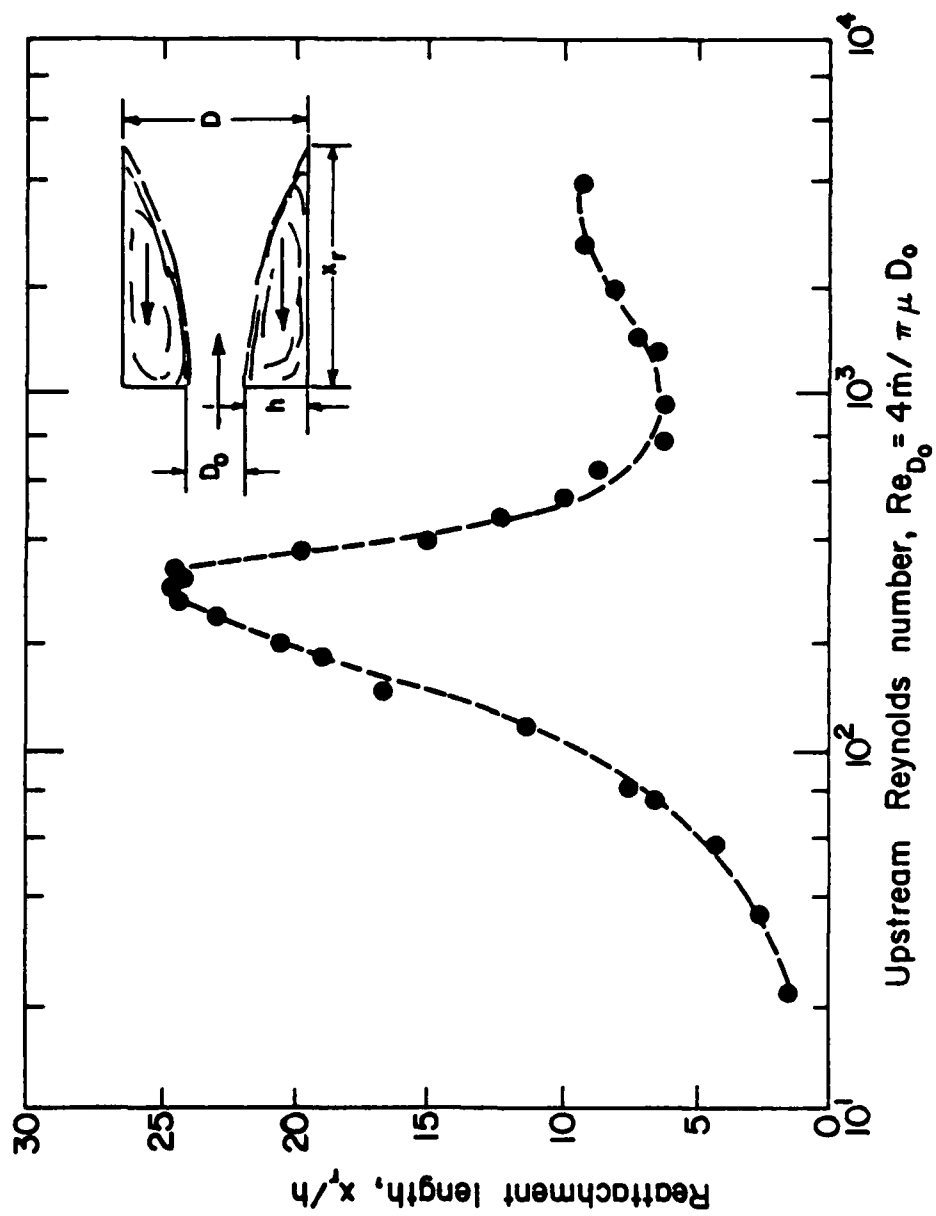


Figure 4. Reattachment length vs. Reynolds number
(from Back and Roschke [15]).

the air in the recirculation region was stagnant, and that "the usual boundary-layer assumptions are valid."

With this analytical model, Cramer [16] predicted the increase in the laminar reattachment length x_r , to be

$$\frac{x_r}{\delta_s^*} = \frac{Re_{\delta_s^*}}{3} \left[\left(\frac{h}{\delta_s^*} + 1 \right)^2 - 1 \right]. \quad (1)$$

Using the criterion set forth by Goldstein et al. [10] for laminar reattachment, Equation (1) yields a maximum reattachment length of over 300 step heights, which is over 10 times larger than the maximum observed by Back and Roschke [15].

Goldstein et al. [10], using a least squares fit to their data, found

$$\frac{x_r}{h} = 2.13 + 0.021 Re_h \quad (2)$$

to be the relationship describing laminar reattachment. This yields a maximum reattachment length of 13 step heights, which is closer to experimental values but significantly less than the maximum of 25 found by Back and Roschke [15].

Using a Blasius profile at the step allows Equation (2) to be compared with Equation (1), hence

$$\frac{x_r}{\delta_s^*} = 0.01325 Re_{\delta_s^*} \left[\left(\frac{h}{\delta_s^*} + 1 \right)^2 - 1 \right]. \quad (3)$$

The constant in this equation is much less than the 1/3 Cramer used. This difference is not surprising since visual observations indicate that the free shear layer is deflected toward the wall considerably. Cramer's assumption of shear layer growth toward the wall like a spreading laminar jet predicts reattachment lengths that are longer than the experimentally observed values.

Back and Roschke's [15] transitional separated flow occurred as the Reynolds number increased from 250 to 1000, characterized by flow in which smooth wave motions in the free shear layer were replaced by more random fluctuating behavior. They observed small shear layer waves at $Re_{D_0} \approx 200$ moving downstream with the flow and growing in amplitude as the inertial forces increased relative to the viscous forces, i.e., as the Reynolds number increased. This is the type of free shear layer mechanisms that Crabtree [6] incorrectly explained. At $Re_{D_0} = 290$ the lateral extent of the shear layer wave resembled a vortex sheet and the reattachment point moved upstream as the vortex sheet rapidly thickened with increasing Reynolds number. Eaton, Johnston, and Jeans [17] found the existence of a spanwise vortex structure in the free shear layer based upon their hot wire results. Their velocity histograms near the upper edge of the shear layer showed a structure similar to that described by Back and Roschke.

[17] Eaton, J.D., Johnston, J.P., and Jeans, A.H., "Measurements in a Reattaching Turbulent Shear Layer," 2nd Symposium on Turbulent Shear Flows, Imperial College, London, 2-4 July, 1979.

At Reynolds numbers greater than 1000, the reattachment length of Back and Roschke's [15] data appeared fairly constant (6-8 step heights) and the fluid appeared to have a random eddying motion. The shear layer spreads rapidly in this case because of enhanced lateral transport by more random, and relatively more pronounced, fluctuations in the flow. Seban, Emery, and Levy [18] using impact and static tubes found the reattachment point for turbulent separated flow to occur at six step heights. Tani, Iuchi, and Komoda [19] located the reattachment point for turbulent separated flow at seven step heights using hot wire results and flow visualization. Moon and Rudinger [20], in a turbulent axisymmetric annular step experiment, found the reattachment point to occur at 8-9 step heights by interpreting mean velocity profiles obtained with a laser Doppler velocimeter. Eaton, Johnston, and Jeans [17] commented on this discrepancy of reattachment length, or rather, the unsteadiness of the reattachment point by suggesting that the recirculation region is slowly growing and shrinking. The entrainment rate balances the backflow rate but only in the mean, not instantaneously. For example, the occurrence of a very large entrainment rate

-
- [18] Seban, R.A., Emery, A., and Levy, A., "Heat Transfer to Separated and Reattached Subsonic Turbulent Flows Obtained Downstream of a Surface Step," Journal of the Aero/Space Sciences, Vol. 26, No. 12, pp. 809-814, December, 1959.
- [19] Tani, I., Iuchi, M., and Komoda, H., "Experimental Investigation of Flow Separation Associated with a Step or Groove," Aeronautical Research Institute, University of Tokyo, Report No. 364, pp. 119-137, April, 1961.
- [20] Moon, L.F., and Rudinger, G., "Velocity Distribution in an Abruptly Expanding Circular Duct," ASME Journal of Fluids Engineering, Vol. 99, pp. 226-230, March, 1977.

would shorten the whole region. The free shear layer would then be too short to entrain all of the backflow, implying that the whole region would grow. This phenomenon of unsteady reattachment location was observed to be of a relatively long time scale.

Theoretical prediction of turbulent reattachment is a very difficult task and generally requires a numerical solution of the time-averaged Navier-Stokes equations. This solution in terms of mean streamwise velocity profiles is then used to determine the reattachment point. Further discussion of this topic can be found in Section II-8.

b. Area Ratio

The area ratio (A_R) of a sudden expansion is defined as the ratio of the area downstream of the step to the area upstream of the step. The area ratio is important when correlations between single-step and double-step models are attempted as the reattachment length is not necessarily the same in both cases.

Abbott and Kline [11], in an open channel study of turbulent separated flow found the reattachment length to be markedly dependent on the area ratio for both single and double-steps. The reattachment length increased with an increase in area ratio; however, for area ratios greater than 1.5 the lengths of the recirculation regions were different for the two sides of the double-step. Figure 5 shows that the reattachment length can be up to four times larger for one side of the double-step than the other. For area ratios less than 1.5 the reattachment lengths on each side of the double step are equal and match the lengths for a single-step of the same area ratio.

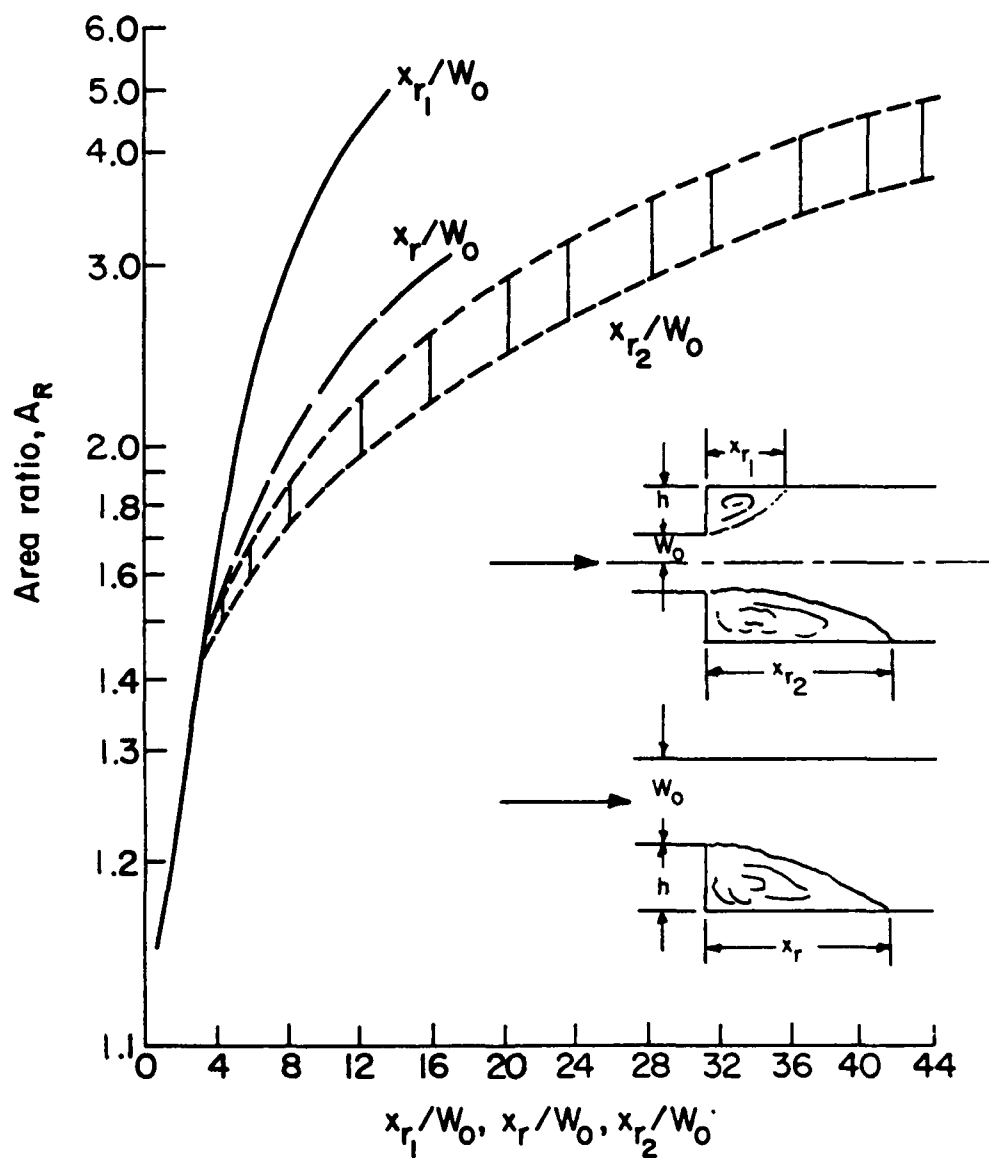


Figure 5. Area ratio vs. reattachment length (from Abbott and Kline [11]).

Durst, Melling, and Whitelaw [12] in an investigation of laminar two-dimensional double duct step flow with a 3:1 area ratio found unequal reattachment lengths at a Reynolds number of 114 (based on step height h). However, in an earlier investigation by the same authors in which a 2:1 area ratio was used [21], equal reattachment lengths were observed at a Reynolds number of 114. Thus, laminar separated flow also exhibits an area ratio dependent, unequal reattachment length phenomenon.

Cherdron, Durst, and Whitelaw [22] suggested that the origin of the asymmetry (unequal reattachment lengths) is related to the shear layers and the coherent flow structures embedded within them. Winant and Browand [23] showed that such structures do exist in shear layers and can interact with each other, yielding an asymmetric flow field phenomena. Apparently, the eddies originate separately in the two shear layers, but because of the confinement of the model, are very much interdependent. The influence of these eddies extends from the shear layer to the duct centerline. If the main flow is dominant enough to discourage shear layer interaction (high inlet velocity) or if the geometry of the duct is such that shear layers are far apart (large inlet area), then symmetric vortex shedding occurs and symmetric

-
- [21] Durst, F., Melling, A., and Whitelaw, J.H., "Optical Anemometer Measurements in Recirculating Flows and Flames," In: Proceedings DISA Conference, Vol. 1, paper II, Leicester University Press, 1972.
 - [22] Cherdron, W., Durst, F., and Whitelaw, J.H., "Asymmetric Flows and Instabilities in Symmetric Ducts with Sudden Expansions," Journal of Fluid Mechanics, Vol. 84, pt. 1, pp. 13-31, 16 January, 1978.
 - [23] Winant, C.D., and Browand, F.K., "Vortex Pairing: The Mechanism of Turbulent Mixing Layer Growth at a Moderate Reynolds Number," Journal of Fluid Mechanics, Vol. 63, pt. 2, pp. 237-255, 3 April, 1974.

mean flow patterns will be predominant. If the shear layers interact a stable flow will exist only if the normal fluctuating velocities are out of phase with each other. In the case of Durst et al. [12], unequal reattachment lengths would be caused by fluctuating velocities in phase with each other. Abbott and Kline's [11] data (Figure 5) shows more and more asymmetry as the area ratio is increased. This area ratio increase was implemented by decreasing the inlet area. This allowed the shear layers to interact producing asymmetric mean flow patterns.

Figure 5 shows that a two-dimensional single open channel step model directly correlates to a double-step model, with respect to reattachment length, for turbulent flow if the area ratio is less than 1.5. Similar types of correlations certainly can exist for other types of models and separated flows. However, Abbott and Kline's work remains as one of the prime sources for turbulent sudden expansion flows. Laminar and transitional sudden expansion flows are much less predictable.

c. Aspect Ratio

Aspect ratio (A_s) is defined as the ratio of spanwise width to the inlet height. The general concern about aspect ratio is that it should be large enough so that wall effects do not dominate the flow field in a two-dimensional duct or surface step model. This would allow center-line measurements of a two-dimensional model to be compared with the flow field data of an axisymmetric annular step providing that the flow field of the two-dimensional model was symmetric.

Rothe and Johnston [24] concluded that for turbulent two-dimensional single duct step flow the aspect ratio had little or no effect upon the reattachment point. Their hydrogen bubble and dye studies showed reattachment occurring at seven step heights over an aspect ratio range of two to fifteen.

No conclusive evidence is known about aspect ratio effects for laminar separated flows. Cherdron, Durst, and Whitelaw [22], however, showed that a decrease in aspect ratio for both a 2:1 and 3:1 area ratio had a stabilizing effect which extended the range of Reynolds numbers over which symmetric laminar separated flow could exist. Their measurements were made in a two-dimensional double duct step using a one-component laser Doppler velocimeter. Figure 6 which maps the regions of symmetric and asymmetric flow, for example, shows that for an expansion ratio of 2:1 and an aspect ratio of 4:1, the recirculating flow regions on the two sides of the duct are identical in size if the Reynolds number (Re_h) is 210 or less. For a Reynolds number of 210, and an aspect ratio of 8:1, the flow would become asymmetric.

Most investigations involving two-dimensional flow models have only considered aspect ratio in terms of the physical size of the model and not as a dimension critical to the character of the flow field. This may or may not be a correct assumption.

[24] Rothe, P.H., and Johnston, J.P., "Free Shear Layer Behavior in Rotating Systems," ASME Journal of Fluids Engineering, Vol. 101, pp. 117-120, March, 1979.

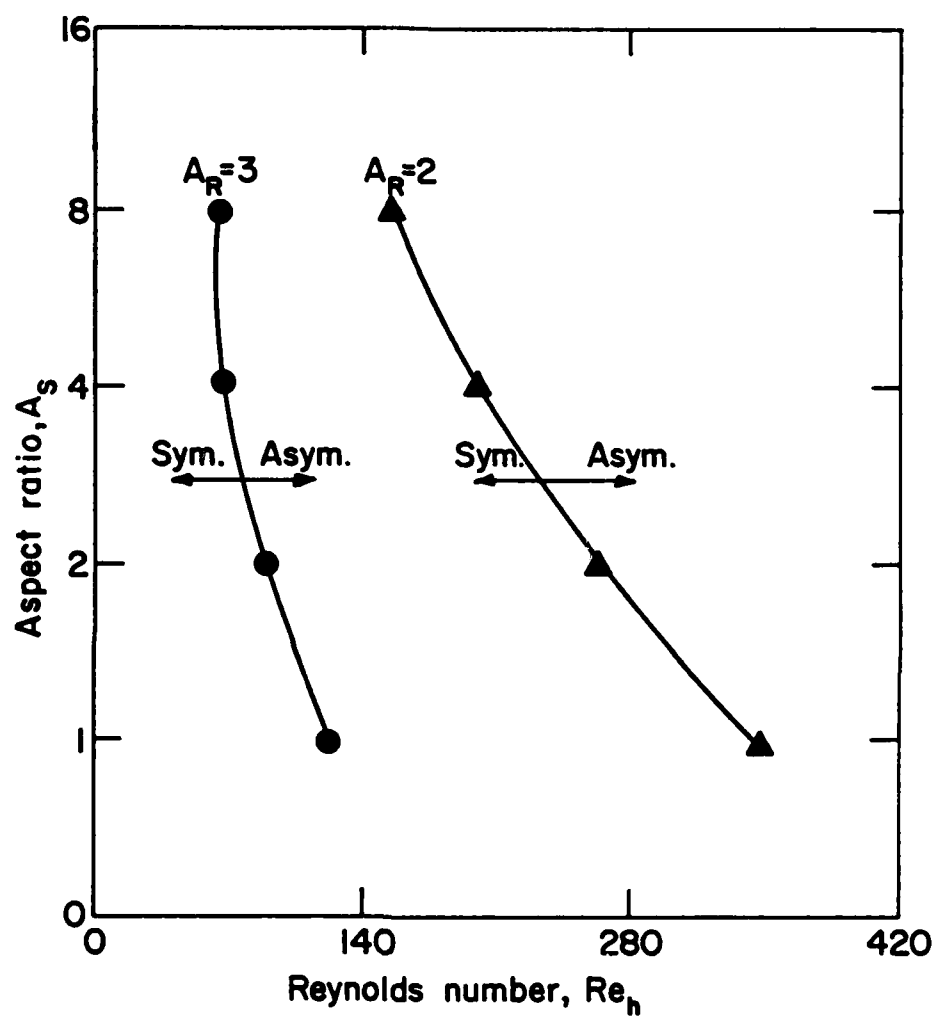


Figure 6. Aspect ratio vs. Reynolds number
(from Cherdron et al. [22]).

d. Inlet Flow Conditions

The popularly held view concerning inlet flow conditions for turbulent flows is that the high degree of turbulence generated at separation overwhelms any contribution to the character of the flow field made by the approaching flow conditions. Thus, reattachment lengths are unaffected by inlet flow conditions. This includes both the inlet free-stream (core) and the inlet boundary layer conditions. It is important to note that laminar or transitional separated flows are dependent on the inlet boundary layer conditions, particularly δ_s^* (Section 11-2.).

Davies and Snell [25] varied the upstream conditions in a two-dimensional single duct step and found insignificant changes in the mean velocity distribution. Their hot wire anemometer measurements were made for inlet conditions including natural boundary layer growth, boundary layer suppression, and the introduction of upstream shear. They did find, however, noticeable changes in the distributions of turbulence intensity and shear stress across the shear layer. Eaton, Johnston, and Jeans [17] found the mean velocity profiles to be similar when comparing their results with those of Etheridge and Kemp [26]. Their investigation involved a boundary thickness of 0.2 step heights while that of Etheridge and Kemp was 2 step heights thick. They also found that the turbulence profiles were in good agreement. Previous to these investigations most observers based their conclusions on the

[25] Davies, T.W., and Snell, D.J., "Turbulent Flow Over a Two-Dimensional Step and Its Dependence Upon Upstream Flow Conditions," *Turbulent Shear Flows I*, Springer-Verlag, New York, pp. 13.29-13.33, 1977.

[26] Etheridge, D.W., and Kemp, P.H., "Measurements of Turbulent Flow Downstream of a Rearward-Facing Step," Journal of Fluid Mechanics, Vol. 86, pt. 3, pp. 546-566, 14 June, 1978.

very slight changes in mean velocity profiles. Davies and Snell added that the uncertainties associated with measurement techniques in highly turbulent flows prevented any definite conclusion about the inlet flow influence.

Davies and Snell [25], however, felt that the variations in turbulence intensity and shear stress distribution caused by the approaching flow conditions were large enough to explain differences between results on very similar geometrical configurations [11], [19]. Eaton, Johnston, and Jeans [17] felt that these differences could better be explained by differences in the streamwise pressure gradient as well as differences in reattachment length between the models.

5. Typical Flow Field Profiles

a. Mean Velocity Profiles

Figure 7 shows the development of the mean streamwise velocity profiles obtained by Cherdron, Durst, and Whitelaw [22]. The two Reynolds numbers presented correspond to the range in which asymmetric flow patterns exist as shown in Figure 6. The asymmetry described in previous sections can clearly be seen for the higher Reynolds number. In this case of laminar separated flow, the maximum recirculation region velocity is approximately one tenth that of the maximum velocity (U_{\max}) in the profile. The same general trend occurs for turbulent separated flow in a double duct step as the profiles of Smyth [27]

[27] Smyth, R., "Turbulent Flow Over a Plane Symmetric Sudden Expansion," ASME Journal of Fluids Engineering, Vol. 101, pp. 348-353, September, 1979.

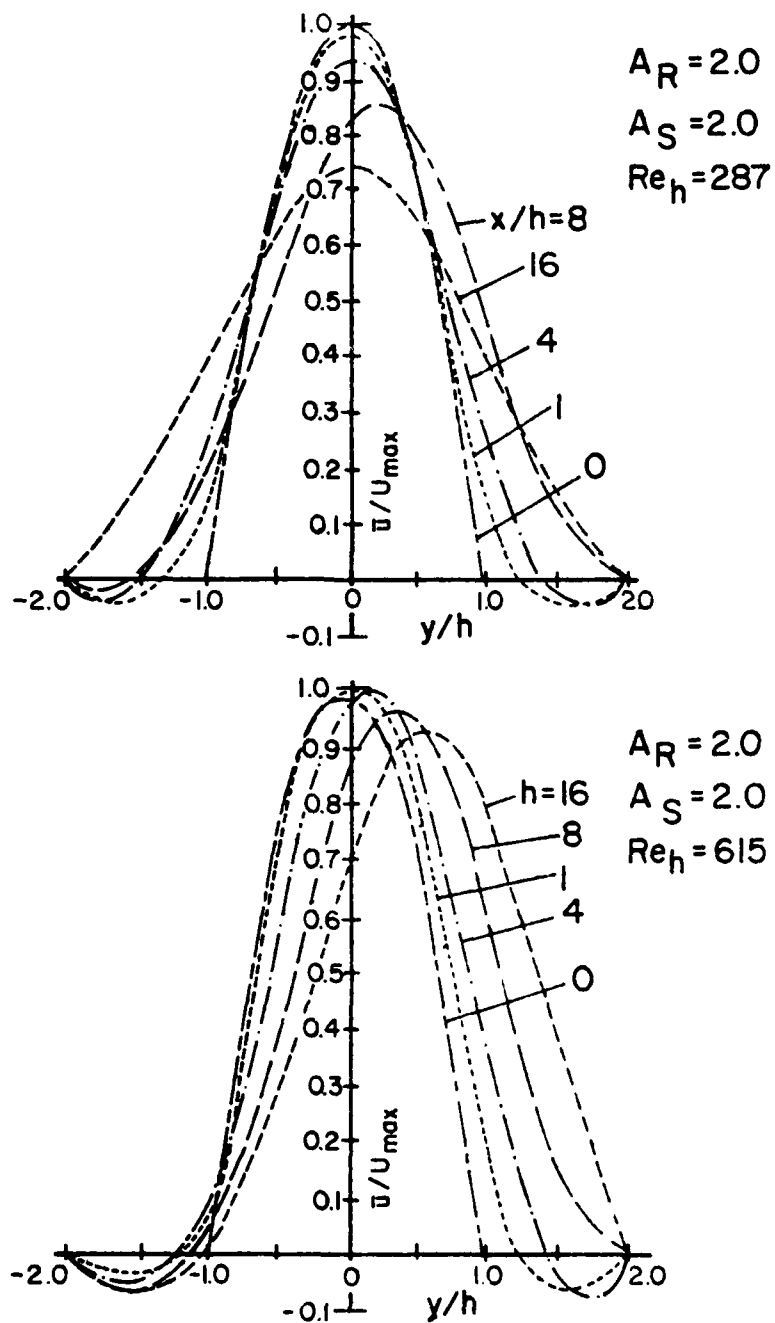


Figure 7. Mean streamwise velocity profiles (from Cherdron, Durst, and Whitelaw [22]).

show in Figure 8. In this case the flow was symmetrical and $Re_h = 3.021 \times 10^4$ with $U_m = 0.67$ meters per second. His single component LDV results show the maximum recirculation velocity was eight percent of the mean inlet velocity, U_m . The flow reattaches at approximately nine step-heights downstream of the double step.

b. Turbulence Intensity Profiles

Figure 9 shows the streamwise turbulence intensity downstream of a step from the data of Smyth [27] and corresponds to the profiles presented in Figure 8. The minimum intensity occurs at the center of the duct and is approximately 6.5 per cent. The maximum turbulence intensity (non-dimensionalized with U_m) is approximately 19.5 per cent at $x/D = 0.2$, and at $x/D > 3$ the peaks of the maximum turbulence intensity begin to disappear as a new turbulent boundary layer grows. Further downstream the turbulence intensity appeared similar to that upstream of the step. It is this type of profile that Davies and Snell [25] claim is significantly affected by inlet flow conditions. For the case of asymmetric mean velocity profiles, the streamwise turbulence intensity profile would also be asymmetric.

Figure 10 shows the turbulent kinetic energy and the Reynolds stress distributions from the data of Smyth [27]. The minimum turbulent kinetic energy occurs downstream of the step at the center of the duct while a maximum value of 6.2 per cent occurs near the edge of the recirculation region at $x/L = -.8$. Downstream of the step there is negligible Reynolds stress at the center of the duct with a maximum value of -1.5 per cent occurring near the edge of the recirculation region at $x/L = 0.4$. It is these regions of maximum shear stress that,

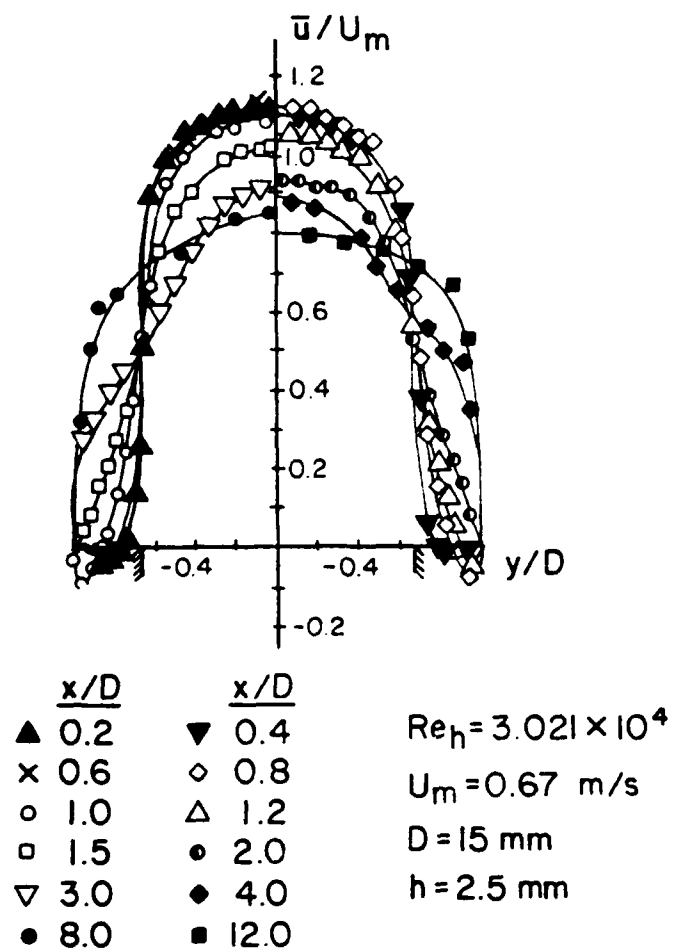


Figure 8. Mean streamwise velocity profiles (from Smyth [27]).

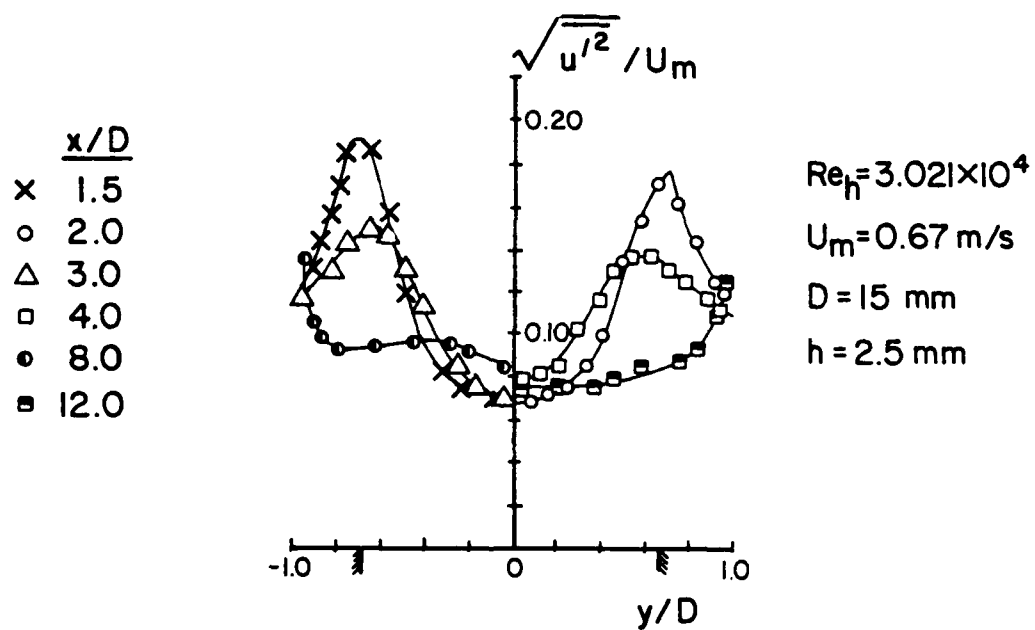
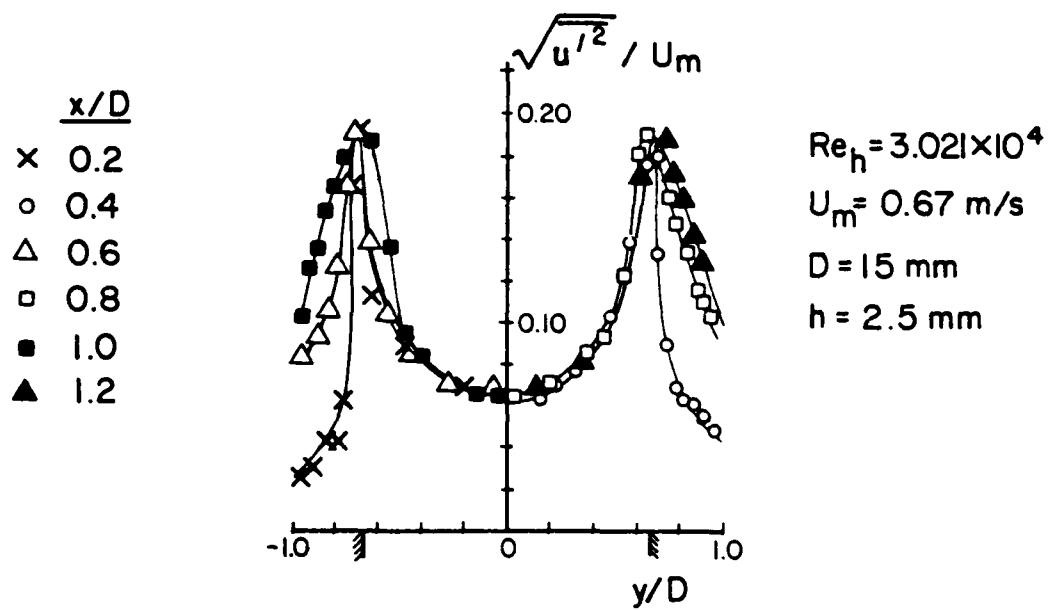


Figure 9. Streamwise turbulence intensity profiles (from Smyth [27]).

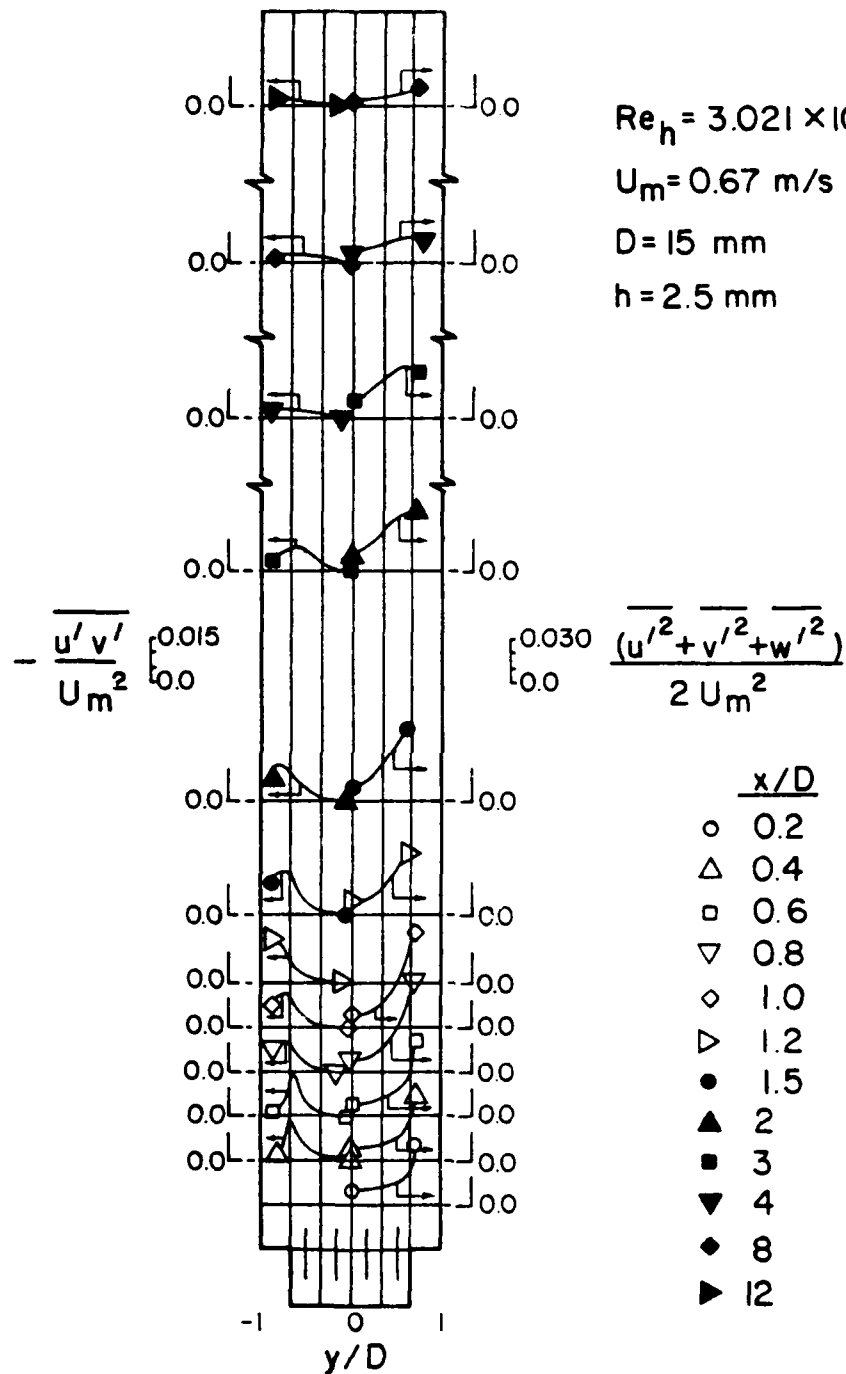


Figure 10. Turbulent kinetic energy and Reynolds stress (from Smyth [27]).

along with entrainment mechanisms, maintain the equilibrium of the separated flow regions.

6. Pressure Distribution

Chapman, Kuehn, and Larson [4], in further defining the three types of flow, noted that there is an abrupt pressure rise associated with the transitional regime. They concluded that any change in a parameter which affects transition (Reynolds number, surface roughness, turbulence level, etc.) can also change the pressure distribution directly through the change in the location and magnitude of this steep pressure rise. They noted, however, that the closer the transitional point was to reattachment, the greater the pressure rise associated with transition would become.

Tani, Iuchi, and Komoda [19] provided pressure coefficient data for turbulent flow over two-dimensional surface steps as shown in Figure 11. In this case C_p is equal to the static pressure P minus the upstream pressure P_0 and is non-dimensionalized by the dynamic pressure $1/2 \rho U_0^2$. The values of x/h lying between -1 and 0 correspond to locations on the step face, while the positive values of x/h correspond to those on the bottom surface downstream of the step.

Figure 11 shows that the pressure distribution is rather insensitive to step height, with a negative pressure coefficient on the step face. This is followed initially by a slight drop in pressure coefficient downstream of the step, and then by a rather rapid rise in pressure indicating the reattachment of the separated flow.

Tani et al. [19] also found that no appreciable change occurred in the pressure distribution when a triangular fillet was inserted

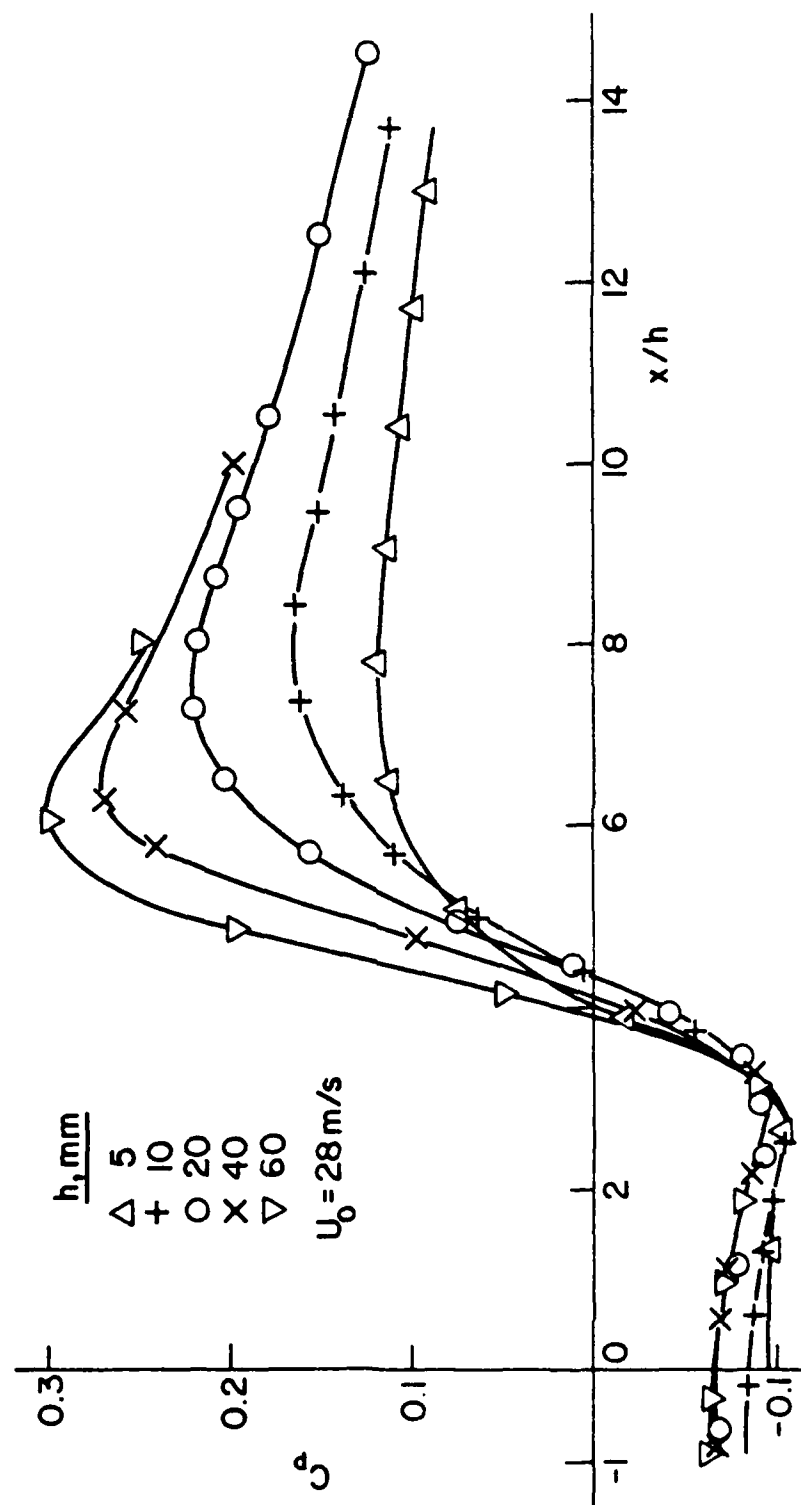


Figure 11. Pressure coefficient distribution
(from Tani et al. [19]).

behind the step until the fillet height exceeded one half of the step height. When a fence one half the step height was placed at various positions on the bottom surface the most appreciable effect occurred when it was placed two step heights downstream from the step. This suggests that the interaction between the recirculation region and the main flow remains unchanged unless the recirculation region is significantly altered, such as when the fence was two step heights downstream.

In comparison to the work of Tani et al. [19], Moss, Baker, and Bradbury [28] also found a similar pressure distribution as shown in Figure 12. Their work was also with turbulent flow over a two-dimensional surface step though the step was larger and the average inlet velocity was smaller. They also concluded that the upstream boundary layer thickness effects on the pressure distribution for turbulent flow were very small.

7. Experimental Technique

Sudden expansions pose three distinct flow field features:

(1) a recirculating flow region (reverse flow) where the mean velocity is small but the turbulence intensity is high, (2) a strong shear layer with high turbulence intensity, and (3) three-dimensional flow.

Various instruments and techniques have been used to determine the nature of sudden expansion flow fields.

[28] Moss, W.D., Baker, S., and Bradbury, L.J.S., "Measurements of Mean Velocity and Reynolds Stresses in Some Regions of Recirculating Flow," Turbulent Shear Flows I, Springer-Verlag, New York, pp. 13.1-13.7, 1977.

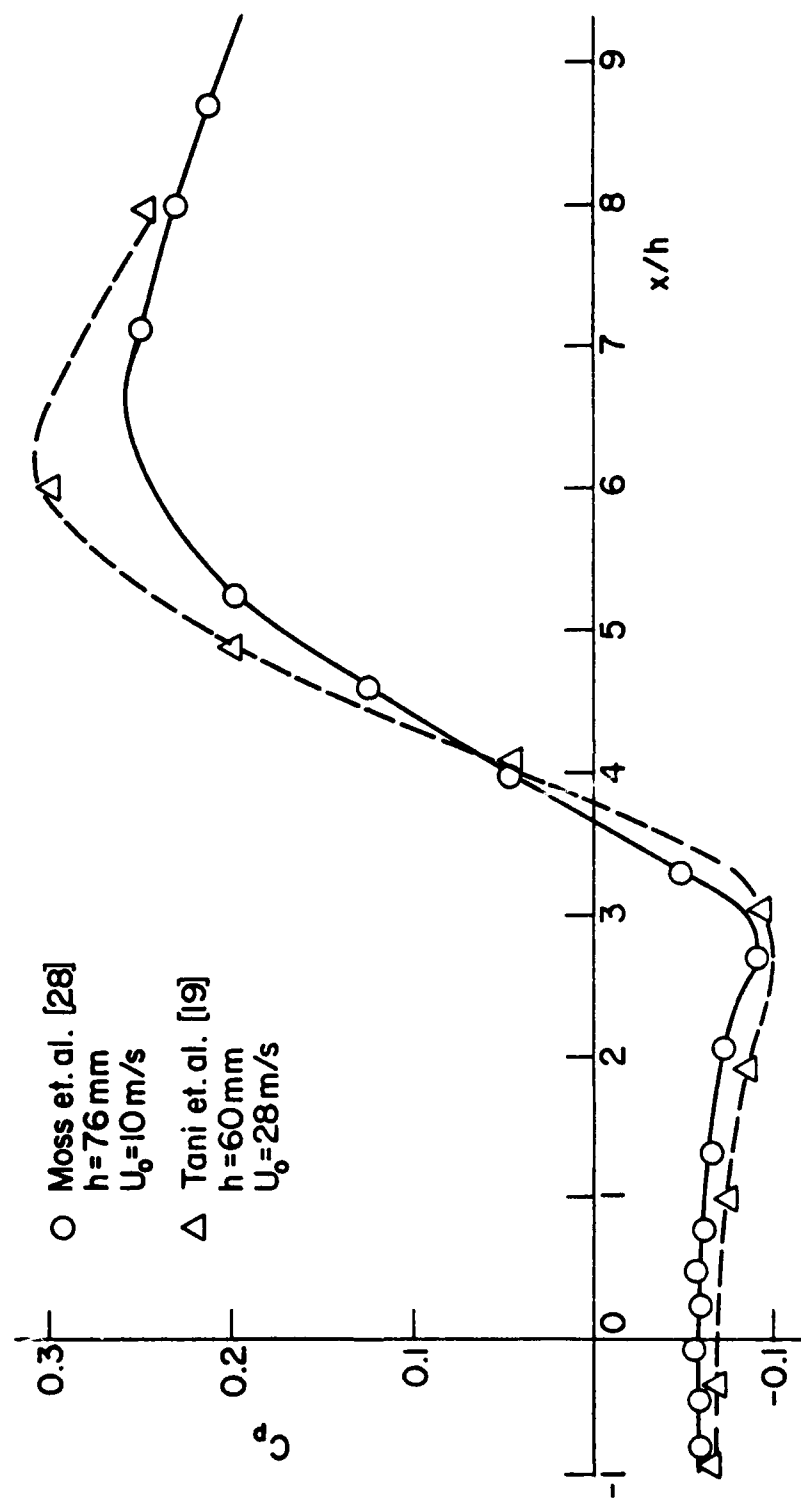


Figure 12. Pressure coefficient distribution (from Tani et al. [19] and Moss et al. [28]).

One of the original and certainly the most common instrument used is the Pitot tube [8,17,19]. Its application is for mean velocity measurements with probe alignment as the significant source of error. It does not allow measurements of the mean velocity in the recirculation region due to the high turbulence intensities and the probe alignment problems associated with the reverse flow. It has been used, however, to identify the outside edge of the recirculation region as well as the boundary layer growth downstream of the reattachment point.

Static pressure taps have been used quite often [8,18,19,28] and provided wall static pressure measurements. This local static pressure, in conjunction with the shear stress distribution, is useful in understanding the balancing forces of the recirculation region. Measurement of the static pressures within the recirculation region of a sudden expansion by using the "static-pressure" holes of a Pitot-static tube is not recommended as the measurement is significantly affected by the turbulence velocities. The measured static pressure would be low mainly because of the lateral turbulence velocities perpendicular to the tube.

One of the most utilized instruments is the hot wire anemometer [10,11,17,25]. It allows the measurement of mean velocity components as well as turbulence intensities for the entire sudden expansion flow field. Its main features are a continuous signal, high sensitivity, and good reliability. Two and three-dimensional hot wires have been used allowing the measurement of all the correlations in the Reynolds stress tensor. A "thermal tuft" hot wire was used by Eaton, Johnston, and Jeans [17] to determine the mean velocity direction in a thin layer of fluid near the wall in the recirculation region. In general, however, reverse flow is a problem for hot wires with rotation of the

wire necessary to determine the flow direction. The hot wire has been used in both cold and hot flow studies with caution having to be taken in the latter case. The hot wire is not without drawbacks. Calibration drift, flow obstruction, and breakage are some of the major concerns.

The latest instrument to be used in sudden expansion flows is the laser Doppler velocimeter (LDV) [12,20,22,27]. The major features of an LDV are: (1) non-obstrusive flow measurements, (2) hot or cold flow applicability, (3) calibration is not required, and (4) the flow direction (if frequency shifting is employed) is known. The LDV makes discrete measurements of the velocity of seeded particles in a flow over a very short time interval (of the order 10^{-6} seconds). The ensemble of these discrete measurements provides mean velocities and turbulence intensities when appropriate statistical formulas are employed. To avoid bias errors in highly turbulent flows, extreme care is required in processing the ensemble of these discrete measurements. LDV systems have been developed to measure two or three mean velocity components as well as their respective turbulence intensities. These systems also allow direct measurement of the Reynolds stress. Since an LDV is a relatively new instrument, its measurements are still subject to controversy. The most significant argument concerns bias errors inherent to measurements in turbulent flows. While one side of the argument deals with the degree of bias error, the other side discounts the existence of bias errors or at least their significance. Another problem in LDV measurements is that to generate a signal, light must be scattered. This is usually done by fine particles seeded into the flow. Whether these particles actually follow the flow,

especially in highly turbulent flows, has been the subject of debate. In general, the LDV is still receiving a great deal of attention directed to refining the instrument and identifying its specific bias errors and their correction.

In any experimental investigation visual observations greatly enhance the understanding of the flow. Smoke [8,10,12,22] and dye [11,15] studies as well as aluminum powder [19,26] and oil droplet [22] techniques have been used to obtain qualitative information for sudden expansion flow fields. The identification of the reattachment point and the observation of two- and three-dimensional effects are the major contributions of this type work.

8. Analytical Models of Sudden Expansions

Sudden expansion flows have received varied analytical treatment dependent on whether the flow studied was laminar or turbulent.

Macagno and Hung [13] demonstrated the ease of solution for the laminar flow case by solving the steady Navier-Stokes equations with the stream function and vorticity as dependent variables and using standard finite difference techniques. They also solved the unsteady equations and found these to exhibit computational stability at higher Reynolds numbers than could be obtained using the steady flow equations. Good agreement existed between the calculations and experimental observations.

Teyssandier and Wilson [29] noted that the equations and techniques used to solve the problem of co-flowing jets was applicable to

-
- [29] Teyssandier, R.G., and Wilson, M.P., "An Analysis of Flow Through Sudden Enlargements in Pipes," Journal of Fluid Mechanics, Vol. 64, pt. 1, pp. 85-95, 3 June, 1974.

the sudden enlargement problem. By dividing the flow field into four axial regions and using empirical relations for the energy transport and dissipation terms they were able to obtain a closed system of four nonlinear differential equations. Their main interest was in pressure results and their method proved fairly accurate, though the modeling of the turbulence phenomenon was crude.

A more complete model of the turbulent flow problem involves the two-equation $k \sim \epsilon$ mode developed by Harlow and Nakayama [30] which also appears in the papers of Launder and Spalding [31] and Launder et al. [32]. Both Gosman, Khalil, and Whitelaw [33] and Moon and Rudinger [20] used this two equation model. The two-dimensional, time-average, conservation equations in elliptic form were solved using refined finite difference techniques. The two-equation turbulence model employed requires "turbulence" coefficients. Usually these become "universal" based on experimental verification. Moon and Rudinger demonstrated that these coefficients indeed were not universal, at least not for recirculating flows. Suitable manipulation had to

-
- [30] Harlow, F.H., and Nakayama, P., "Transport of Turbulence Energy Decay Rate," Los Alamos Science Laboratory, University of California Report LA-3854, 1968.
 - [31] Launder, B.E., and Spalding, D.B., "The Numerical Computation of Turbulent Flows," Computer Methods in Applied Mechanics and Engineering, Vol. 3, pp. 269-289, 1974.
 - [32] Launder, B.E., Morse, A., Rodi, W., and Spalding, D.B., "The Prediction of Free Shear Flows - A Comparison of the Performance of Six Turbulence Models," In: Proceedings of NASA Conference Free Shear Flows, Langley, 1972.
 - [33] Gosman, A.D., Khalil, E.E., and Whitelaw, J.H., "The Calculation of Two-Dimensional Turbulent Recirculating Flows," Turbulent Shear Flows I, Springer-Verlag, New York, pp. 13.35-13.45, 1977.

be done to allow favorable comparison with their experimental results. One coefficient required an eleven per cent change for the reattachment location to agree with their experimental value. Gosman, Khalil, and Whitelaw found that although the $k - \epsilon$ model was adequate for engineering purposes, it did not yield a precise representation of the flow field. They felt that the dissipation (ϵ) equation was at least part of the deficiency of the model. More complex models, however, apparently do not result in any better representation of the flow field. It should be remembered that information is lost in time-averaging the Navier-Stokes equations and the resulting equations are bound to be less than exact.

As previously mentioned, laminar sudden expansion flows are relatively easy to solve with the modeler having various techniques at his disposal. Turbulent solutions, however, begin to involve large amounts of computer time and storage when the time-averaged Navier-Stokes equations are solved along with appropriate turbulence models. Stability of the solution is also a problem with heavy under-relaxation methods being employed.

It is interesting to note that asymmetric flow patterns in two-dimensional double duct step flows have not been predicted by numerical techniques though experimental evidence has shown their existence. Apparently, the turbulence models in use are unable to describe the shear layer interaction that is believed to cause asymmetric vortex shedding and asymmetric flow patterns.

SECTION III

EXPERIMENTAL APPARATUS

The experimental mapping of the flow field in the two-dimensional single duct step required various types of instrumentation and hardware. This section describes the overall experimental apparatus and is divided into three major subsections:

1. The flow system.
2. The laser Doppler velocimeter optical system.
3. The data collection, storage, and processing system.

1. Flow System

The flow system was designed to provide a flexible system allowing easy optical access in which a variety of flow geometries could be modeled. The geometry of this study is a two-dimensional single duct step.

As shown in Figures 13 and 14 the flow system consists of seven parts:

1. A radial blade blower.
2. A convergent adaptor.
3. A flow conditioning section.
4. A connecting duct.
5. A single duct step test section.
6. A duct extension
7. A particle generator for seeding the flow.

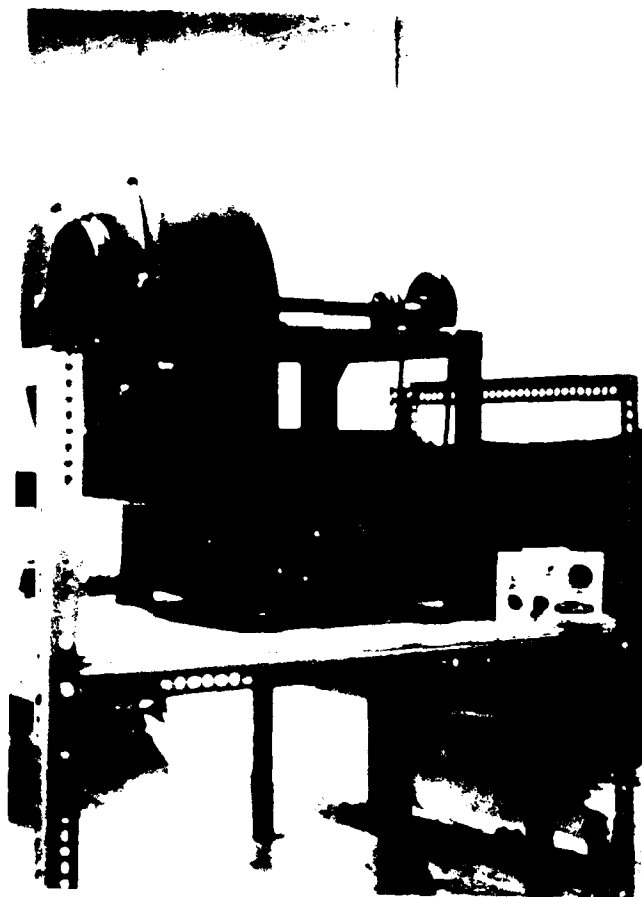


Figure 13. Radial blade blower.

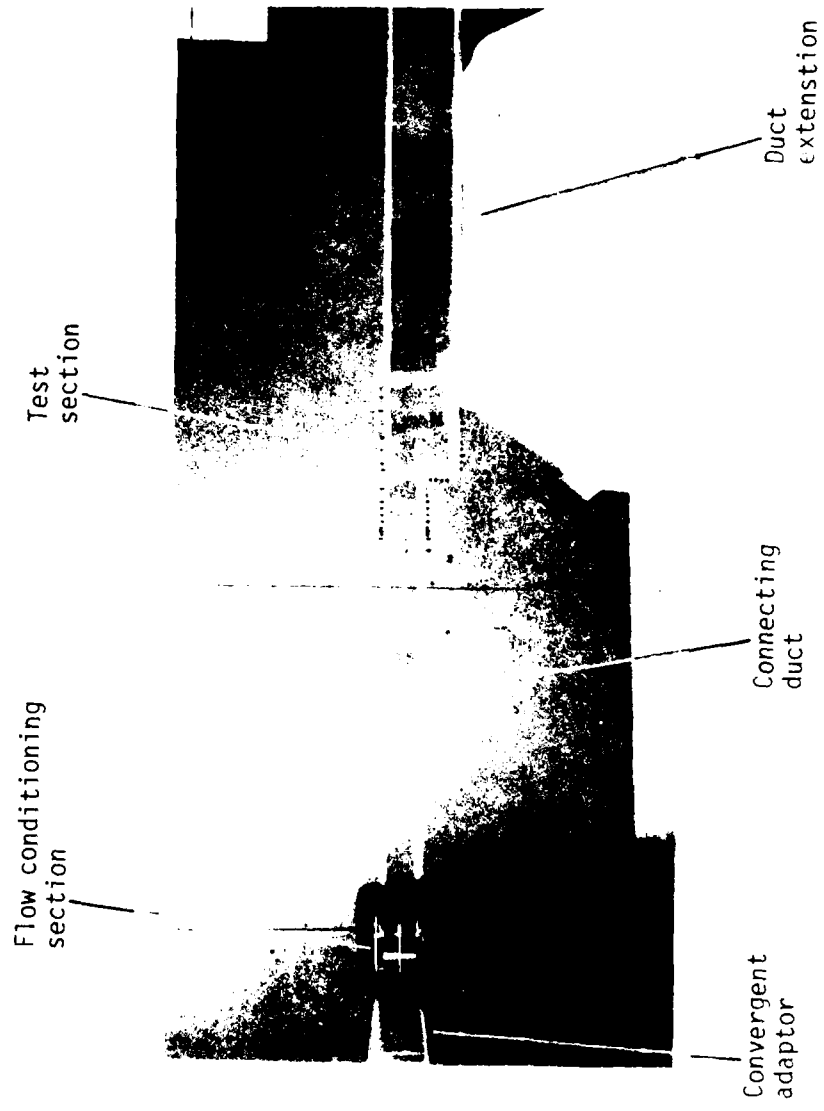


Figure 14. Flow system.

Each part of the flow system will now be discussed.

A Peerless radial blade blower (Model PWB4GA) with a variable speed control is mounted to a 1.22 m (4 ft) high stand as shown in Figure 13. One inch isolators are used to separate the blower from the stand. The blower can be operated over a range of 0 to 0.50 m³/sec (1100 CFM) and provides a flow velocity of up to 50.3 m³/sec (1100 CFM). The exit of the blower is 142.9 mm by 177.8 mm (5.625 in. by 7 in.).

The convergent adaptor section is 0.52 m (20.5 in.) long and is constructed from 1/4 in. Plexiglas. It reduces the exit plane of the blower to a 101.6 mm (4 in.) square.

The flow conditioning section consists of four 25.4 mm (1 in.) Plexiglas blocks connected together as shown in Figure 15. A screen is placed between each block with the entire second block filled with soda straws which serve as a honeycomb mesh.

The connecting 101.6 mm by 101.6 mm duct is 1.21 m (47.5 in.) long and is constructed of 1/2 in. clear Plexiglas. It has two Pitot-static tube mounting holes placed 152.4 mm (6 in.) from the downstream end with one located on the top wall and the other on the side.

The test section is 0.51 m (20 in.) long and is constructed of 1/2 in. clear Plexiglas. The initial 0.22 m (8.5 in.) of the section is a 101.6 mm square duct which changes to a 101.6 mm by 203.2 mm (4 in. by 8 in.) duct over a rearward-facing step ($A_R = 2$, $A_S = 1$). The test section is lined with static pressure taps as shown in Figure 16. The detail of a static pressure tap is shown in Figure 17. The test section also has 3 Pitot-static tube mounting holes. The upstream holes are located 165.1 mm (6.5 in.) ahead of the step; one on the top

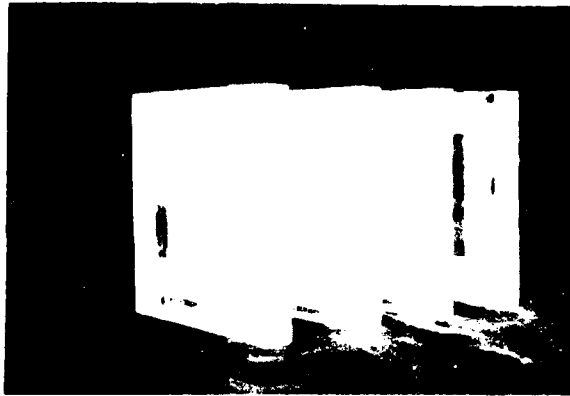


Figure 15. Flow conditioning section.

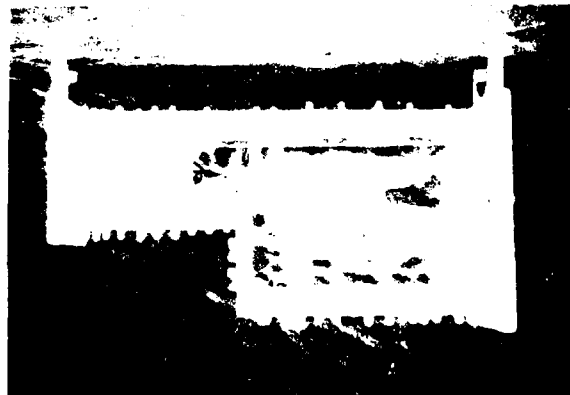


Figure 16. Test section.

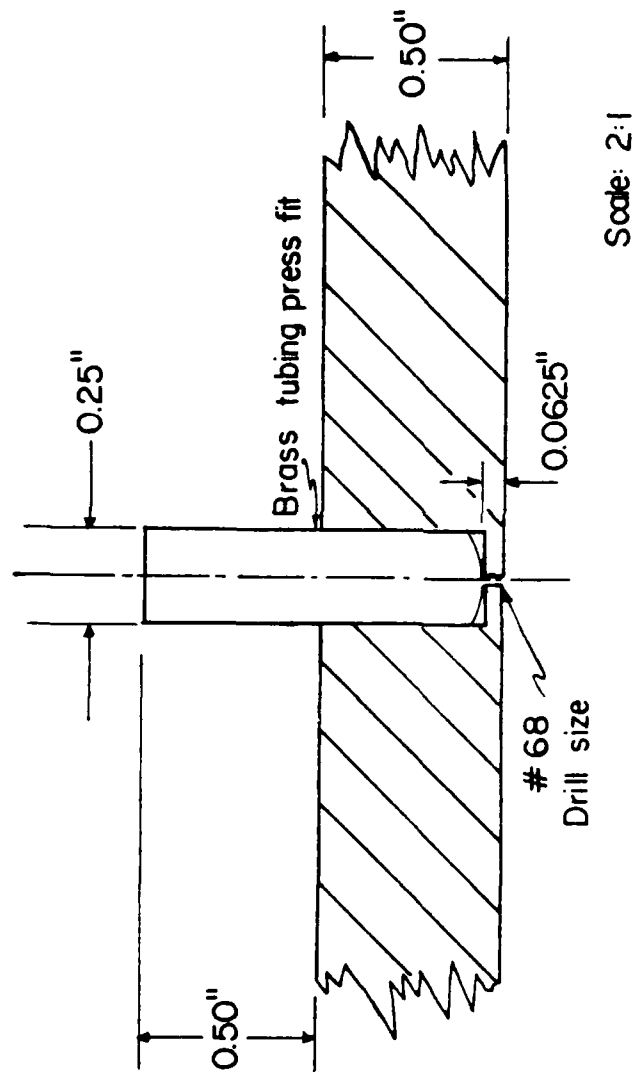


Figure 17. Static pressure tap detail.

and the other on the side. The third hole is located on the top wall 88.9 mm (3.5 in.) downstream of the step.

The 101.6 mm by 203.2 mm duct extension is constructed from 1/2 in. clear Plexiglas and is 1.22 m (48 in.) in length. The initial 0.61 m (24 in.) of the bottom wall is lined with static pressure taps.

The entire flow system is mounted on two concrete pillars with height and leveling adjustments.

The seeding system is a commercial system built by Thermal-Systems Inc. (TSI) and is shown in Figure 18. It consists of an air supply system (Model 3074), a liquid atomizer (Model 3076), and an Evaporation-Condensation Monodisperse Aerosol Generator (Model 3072). Di-octyl Phthalate (DOP) is the fluid used for seeding. The particle size can be varied from 0.4 μm to 1.3 μm .

2. Laser Doppler Velocimeter Optical System

The LDV optical system was designed specifically for studying various bias errors. Thus it has the capability of changing various important optical parameters. This is a very desirable feature as it allows matching of the optical parameters with the specific flow situation. The major LDV optical system features include variable beam diameter in the probe volume, variable fringe spacing, the ability to change the angular orientation of the probe volume, provision for frequency shifting one or both input beams, and the ability to traverse the probe volume in three-dimensional space.

The general layout of the optical system is shown in Figure 19. A 5 watt argon laser (Coherent Radiation, Model 52) operating at the 0.5145 μm wavelength (green line) supplies the laser light. The beam

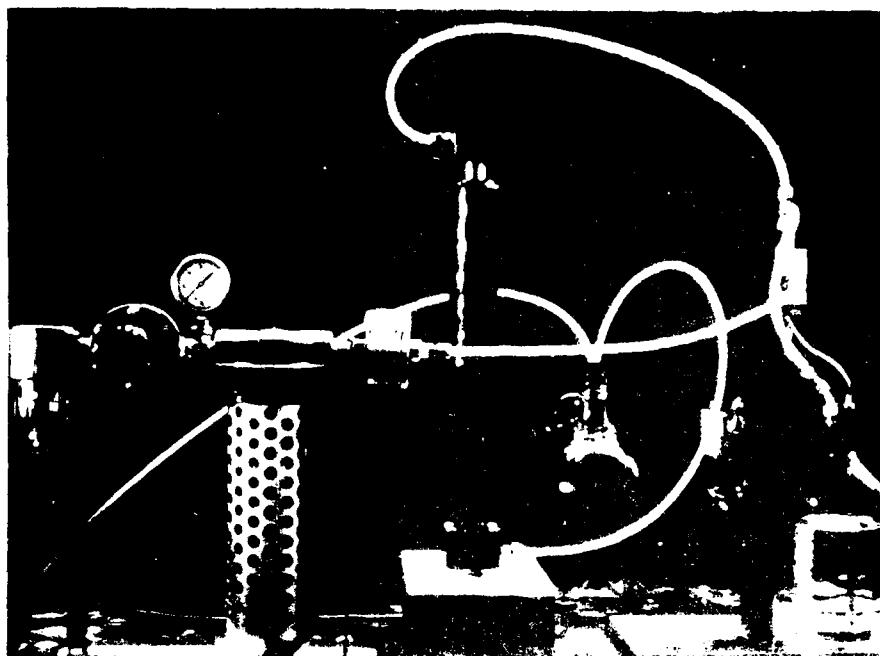
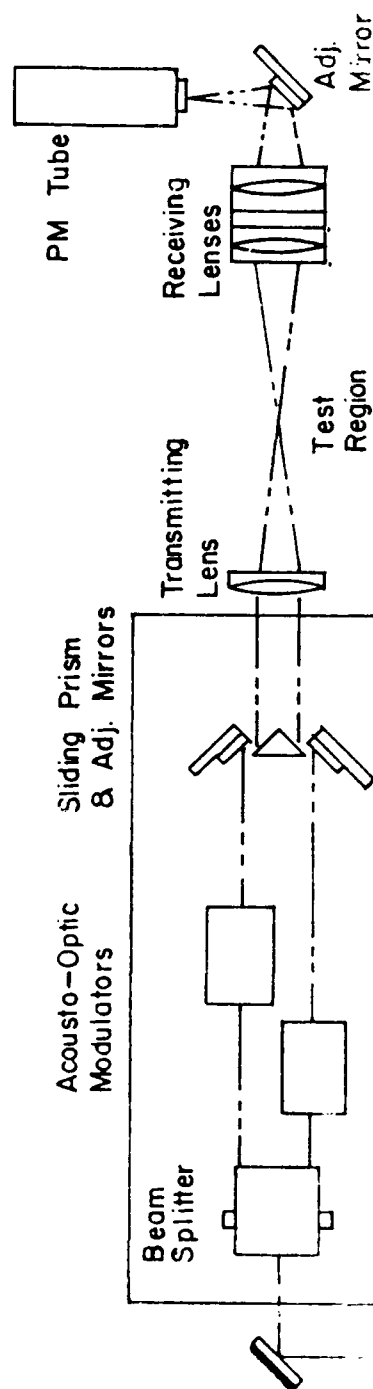


Figure 15. Particle generator system.

UPPER OPTICS PACKAGE



Optics Table

LOWER OPTICS PACKAGE

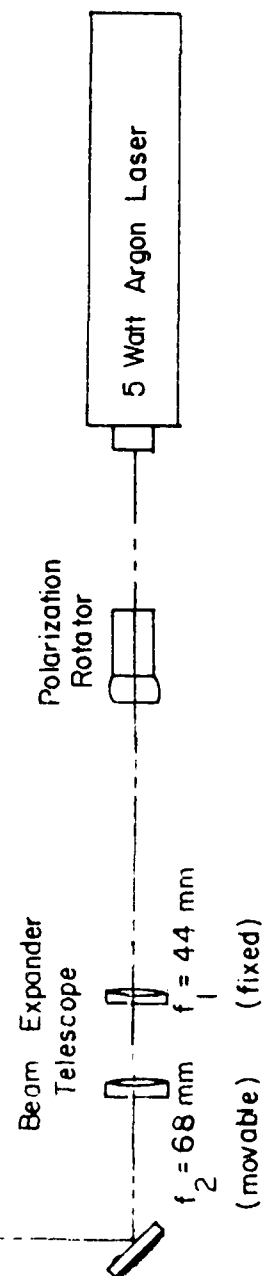


Figure 19. LDV optical system diagram.

exits the laser and enters a polarization rotator (Spectra-Physics, Model 310-21). The polarization rotator allows rotation of the plane of polarization to maintain it perpendicular to the plane of the beam dividing prism. This insures that the beam splitter divides the beam into two equal intensity beams producing a maximum fringe contrast in the probe volume. Upon leaving the polarization rotator the beam passes through a beam expander telescope. The telescope consists of a 44 mm lens (f_1) and a 68 mm lens (f_2). The f_1 lens images the beam waist from the inside of the laser cavity to a point between the two telescope lenses. Then lens f_2 and the transmitting lens image this waist to a location within the test section. By traversing f_2 over a 7.5 mm range waist diameters of 60 to 500 μm can be obtained.

From the telescope, two broadband all-dielectric mirrors (Newport Research Corp.) direct the beam to the beam splitter (TSI, Model #916-1) on the upper part of the optics package. The beam splitter splits the entering beam into two parallel equal intensity beams separated by 50 mm.

Following the beam splitter are two acoustic-optic modulators (Intra-Action Corporation, Model #ADM-40). The modulators shift the frequency of the incoming beam either up or down by an amount equal to the frequency of the driver. Drivers of 30 and either 35 or 40 MHz are available. Various combinations of frequency shifted beams can provide net frequency upshifts or downshifts of 5, 10, 30, 35, 40, 70, or 75 MHz.

After leaving their respective modulators the beams are reflected by adjustable mirrors (Newport Research Corporation, Model #600-2) to a sliding prism. The prism, which has a reflective coating on two

faces, directs the beams to a transmitting lens. Various beam separations can be obtained by translating the prism. The adjustable mirrors serve two purposes. Adjustment about the horizontal axis insures that the focused light beams remain in the same plane as the beams prior to focusing. Adjustment about the vertical axis determines where the point of intersection (probe volume) occurs along the optical axis. The reason for having this flexibility is to insure that the probe volume is located at the waist of the laser beam. Fringe spacing may be changed through proper adjustment of the sliding prism and adjustable mirrors. After reflection by the prism, the beams pass through a transmitting lens (TSI, Model #918) having a focal length of 250 mm which brings them to intersection.

Scattered light from particles passing through the probe volume is collected, collimated, and then focused by a pair of receiving lenses (TSI, Models #917 and #918) mounted several centimeters apart with 250 mm and 120.6 mm focal lengths, respectively. The focused light is reflected by a mirror mounted on an adjustable fixture (Newport Research Corporation, Model #600-2). This allows lateral adjustment of the focused spot, insuring that it is located on the pinhole. The 200 μm pinhole is part of a pinhole-lens-filter combination that is threaded into the front of the photomultiplier tube (RCA, Model #8575). The small positive lens collimates the light passing through the pinhole for improved performance of the PM tube. The optical filter behind the lens allows only light at 0.5145 μm

$\pm .0050 \mu\text{m}$ to reach the PM tube. The receiving lenses and the entire receiving optics package may be moved along the axis of the optical system to allow proper focusing. Beam stops on the initial receiving lens block the direct laser beams, and allow only scattered light to pass into the PM tube.

The upper transmitting optics table is mounted on 4 1/2 in. diameter aluminum journal bearings which rotate inside brass bearing blocks. The bearing blocks are capable of locking the table at any angular position. Rotation of the optics table rotates the probe volume which allows velocity components at various angles to be measured.

Precise positioning of the probe volume at a desired point in the test section is provided by the traversing system (Figure 20). The optical system (including laser) is mounted on a 3-axis mill table. Three Bodine DC gearmotors with variable speed control are used to drive the mill table. Linear potentiometers (New England Instruments) with a linearity of 0.25% are used to obtain an electrical readout of the position on digital panel meters which read directly in millimeters to an accuracy of $\pm 0.1 \text{ mm}$. The circuit design allows for adjustment of the zero position and the span for calibration purposes. The traverse range is 254 mm (10 in.) in the vertical (y) direction and 152 mm (6 in.) in the x and z directions. Also included in the positioning system are two micro switches for each potentiometer. These switches serve as safety devices breaking the power to the gearmotors when triggered.

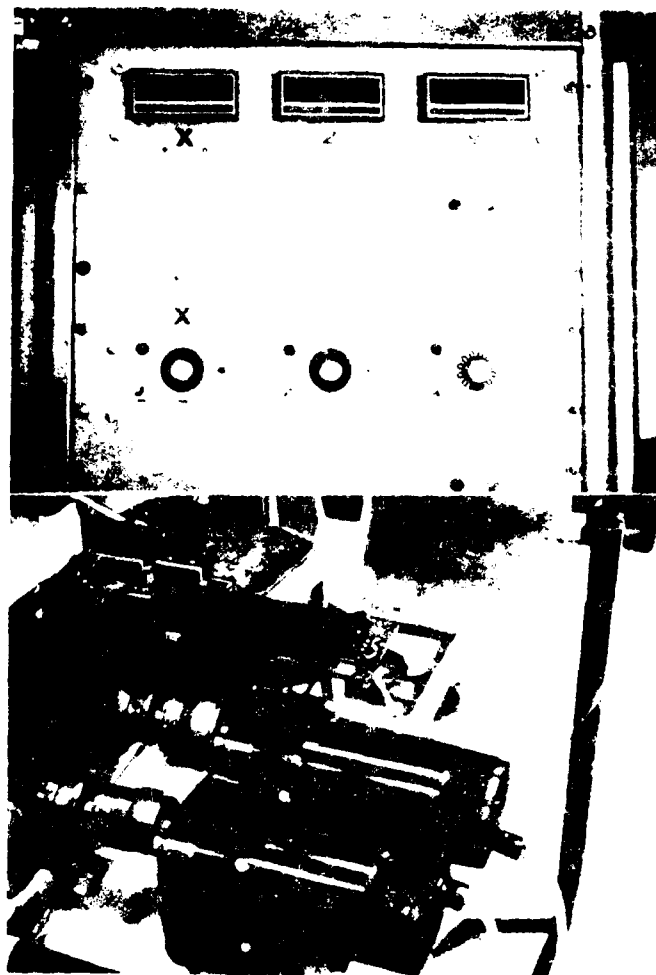


Figure 21. A17 positioning system electronics.

The traversing system allows repetitive positioning of the probe volume to within ± 0.2 mm as defined by the combined accuracy limits of the panel meter and potentiometers. All the controls are rack mounted allowing remote operation of the traversing system.

A more detailed explanation of the entire optical system including the individual components can be found in Ref. [34].

3. Data Collection, Storage, and Processing System

The data collection, storage, and processing system as shown in Figure 21, consists of 5 major units:

1. A TSI Model 1980 signal processor.
2. An IMSAI 8080 microcomputer.
3. A Vistar GTX terminal.
4. A Micropolis floppy disk drive.
5. A CDC 6600 computer (not shown).

A schematic of the system is shown in Figure 22. The output signal from the photomultiplier tube is fed to the TSI Model 1980 signal processor unit. The major features of the TSI processor are a 250 MHz clock with a 2 nanosecond resolution and a digital output. Operation of the TSI processor is described in the Instruction Manual, Ref. [35]. The processor data rate depends on the particle seeding density and the amplifier setting (which effectively sets the trigger level). Data rates may be as low as a few per second to rates in

[34] McVey, R.E., "The Design of a Laser Doppler Velocimeter for Use in Studying Turbulent and Mixing Flows," M.S. Thesis, Purdue University, May, 1979.

[35] Instruction Manual for TSI Model 1980 Counter, Thermo-Systems Incorporated, St. Paul, Minnesota.

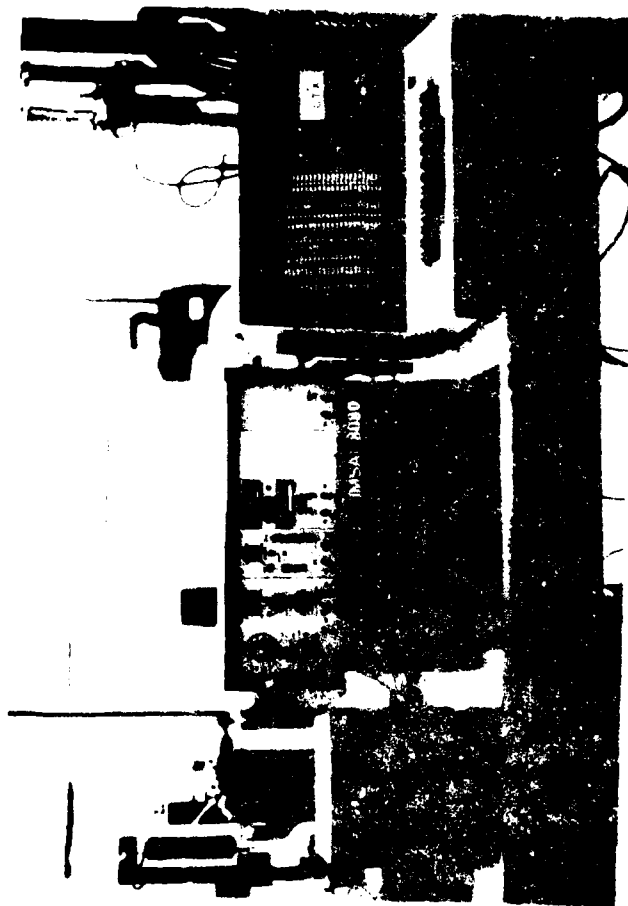


Figure 21. Data collection, storage and processing system.

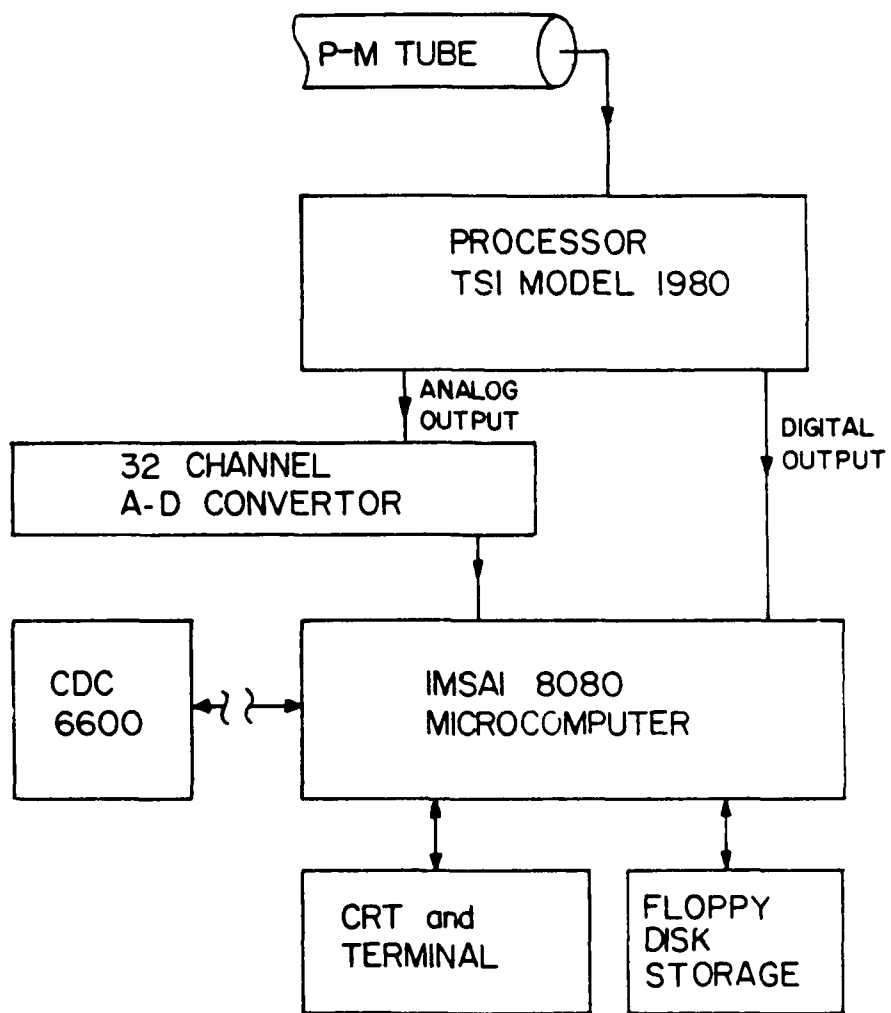


Figure 22. Data collection storage, and processing system schematic.

excess of 20,000 per second. To collect and store this data a dedicated microcomputer (IMSAI 2080) with peripheral equipment is used.

The microcomputer in conjunction with the Vistar GTX terminal and the Micropolis floppy disk drive form the receiving end of the data collection and storage system. When the TSI processor has a data point ready, it sends a data ready pulse to the microcomputer. Upon receiving the pulse, the microcomputer returns a data inhibit to the TSI processor which causes it to hold the data until the microcomputer can process and record it. Once the point is sampled, the microcomputer removes the data inhibit, waits for another data ready pulse, and the process continues. The microcomputer speed is variable with maximum speed of 2748 points per second. The data rate at which velocities are sampled and recorded is dependent on the slowest unit in the system.

The floppy disk drive serves two purposes. It is used to load the data acquisition and storage program (MIDAS) required by the microcomputer and also to store the processor data. A detailed explanation of the data acquisition and storage program (MIDAS) as well as the interaction between the TSI processor and the microcomputer can be found in Ref. [36]. This stored data is then transmitted over phone lines to Purdue's main computer, the CDC 6600. Although some data conditioning is done by the microcomputer, the data analysis is all done through FORTRAN programming of the CDC 6600.

[36] VanFrank, S., "MIDAS-User's and Programmer's Manual," Thermal Sciences and Propulsion Center, Purdue University, 1980.

SECTION IV

EXPERIMENTAL TECHNIQUE

The experimental mapping of the flow field in the two-dimensional single duct step consisted of both direct measurements and correlations of these same measurements. This section presents the techniques used to obtain the following flow field parameters:

1. Pressure coefficient, C_p .
2. Mean velocities and turbulence parameters, \bar{u} , \bar{v} , $\sqrt{\overline{u'^2}}$, $\sqrt{\overline{v'^2}}$, $\frac{1}{2}(\overline{u'^2} + \overline{v'^2})$, $\overline{u'v'}$.
3. Stream function, ψ .
4. Reattachment length, x_r .

Also included in this section are the appropriate values of the various LDV system parameters that were used to obtain the flow field parameters.

1. Pressure Coefficient, C_p

The pressure coefficient, C_p , is defined as

$$C_p \equiv \frac{P - P_0}{\frac{1}{2} \rho U_0^2}, \quad (4)$$

where P is the static pressure, ρ is the air density, and P_0 and U_0 are reference values of static pressure and mean streamwise velocity respectively. The static pressure was measured at a total of 34 stations along the bottom of the duct. Most of the taps were on the centerline of the duct but 9 taps were located 1/2 in. off the centerline to check

for flow uniformity. Three of the static pressure taps are located on the step face. The exact locations of the static pressure taps are listed in Table 7.

The pressure readings were made with a 36 bank manometer (T.E.M. Engineering, Model No. 5585) inclined at 18° with the horizontal. This corresponds to a pressure of 0.785 mm of water per division on the manometer. To record instantaneous pressure measurements 35 mm slides of the manometer bank were taken. Using this method the static pressure measurements can be read to an accuracy of + or - 0.157 mm of water. Because there was some unsteadiness in the flow and to reduce errors in the manometer readings, six measurements were made and the readings at each station were averaged. Before each slide was taken, the reference mean streamwise velocity, U_0 , was measured with a Pitot-static tube and adjusted as necessary to ensure a constant mean velocity. An inclined manometer (The Meriam Instrument Co., Model GP-4) was used for that measurement. The reference velocity, U_0 , was 25.174 m/s (± 0.082 m/s) and was measured at the duct centerline 7 inches upstream of the step ($x/h = -1.75$). The reference static pressure was the static pressure at tap station 1 and was -12.56 mm water gage. An average value of 1.187 kg/m^3 was used for the density, ρ , which corresponded to the typical temperature and barometric pressure for all runs.

Table 7. Static pressure tap locations.

Static Pressure Tap Station	x(in.)	x/h	Static Pressure Tap Station	x(in.)	x/h
1	-7.0	-1.75	18*	9.6	2.4
2	-4.2	-1.05	19*	10.4	2.6
3	-1.8	-0.45	20	13.0	3.25
4	0	0	21	14.5	3.625
5	0	0	22	16.0	4.0
6	0	0	23	17.5	4.375
7	0.8	0.2	24	19.0	4.75
8	1.6	0.4	25	20.5	5.125
9	3.2	0.8	26	22.0	5.5
10	4.0	1.0	27	23.5	5.875
11*	4.8	1.2	28	25.0	6.25
12*	5.6	1.4	29	26.5	6.625
13*	6.4	1.6	30	28.0	7.0
14*	7.2	1.8	31	29.5	7.375
15*	7.6	1.9	32	32.5	8.125
16*	8.0	2.0	33	34.0	8.5
17*	8.8	2.2	34	35.5	8.875

* denotes static pressure tap 1/2 in. off centerline.

2. Mean Velocity and Turbulence Parameters

$$\bar{u}, \bar{v}, \sqrt{\overline{u'^2}}, \sqrt{\overline{v'^2}}, \frac{1}{2}(\overline{u'^2} + \overline{v'^2}), \overline{u'v'}$$

The mean velocities and turbulence parameters are calculated from LDV measurements at various grid points in the flow field. The LDV system used is described in Section III. The system parameters were set to maintain uniformity of measurements and eliminate as many sources of error as possible. Table 8 is a listing of the system parameters used for all measurements.

The waist diameter (probe volume size) was $129 \mu\text{m} \pm 4 \mu\text{m}$ with the position of the waist located $216 \text{ mm} \pm 4 \text{ mm}$ from the face of the transmitting lens. Details of the techniques employed to obtain the waist diameter and position can be found in Ref. [37]. The beam angle was measured by removing the receiving optics (Figure 19) and allowing the two beams to travel to a wall as shown in Figure 23. The probe volume was positioned at the far edge of the test section and the separation between the beams and the distance to the wall was measured. The half angle $\theta/2$ was found to be $3.632^\circ \pm 0.109^\circ$.

The fringe spacing, F_R , can be determined from

$$F_R = \frac{\lambda_0}{2 \sin(\frac{\theta}{2})} \quad (5)$$

-
- [37] Stevenson, W.H., Thompson, H.D., Bremner, R., and Roesler, T., "Laser Velocimeter Measurements in Turbulent and Mixing Flows - Part II," AFAPL-TR-79-2009, Part II, March, 1980.

Table 8. LDV system parameter settings.

<u>Optical System Settings</u>
Telescope setting: 0.200
Prism setting: 10.0
Upstream mirror: upper adjustment: 0.2500 lower adjustment: 0.3905
Downstream mirror: upper adjustment: 0.2400 lower adjustment: 0.3840
λ_0 (laser frequency): 0.5145 μm
$\theta/2$ (beam intersection half angle): $3.632^\circ \pm 0.109^\circ$
F_R (fringe spacing): $4.0606 \mu\text{m} \pm 0.1223 \mu\text{m}$
Probe volume size (waist diameter): $129 \mu\text{m} \pm 4 \mu\text{m}$
f_s (frequency shift): $10 \text{ MHz} \pm 1 \text{ KHz}$
ϕ (rotation of optics): $0^\circ, +30^\circ, -30^\circ$
<u>Data Collection Settings (TSI Processor)</u>
Electronic filter settings: 30 MHz (low pass) 3 MHz (high pass)
N (number of fringes/signal): 16
Comparator: 3 (3.1%)
n (exponent): floating
Data rate: 20,000 samples/sec
Sample rate: 2748 samples/sec
Sample size: 4500 samples
<u>Flow System Settings</u>
Particle size: 1 μm
U_0 (reference velocity at $x/h = -1.75$): $25.174 \text{ m/s} \pm 0.082 \text{ m/s}$
Re_h : 1.68×10^5

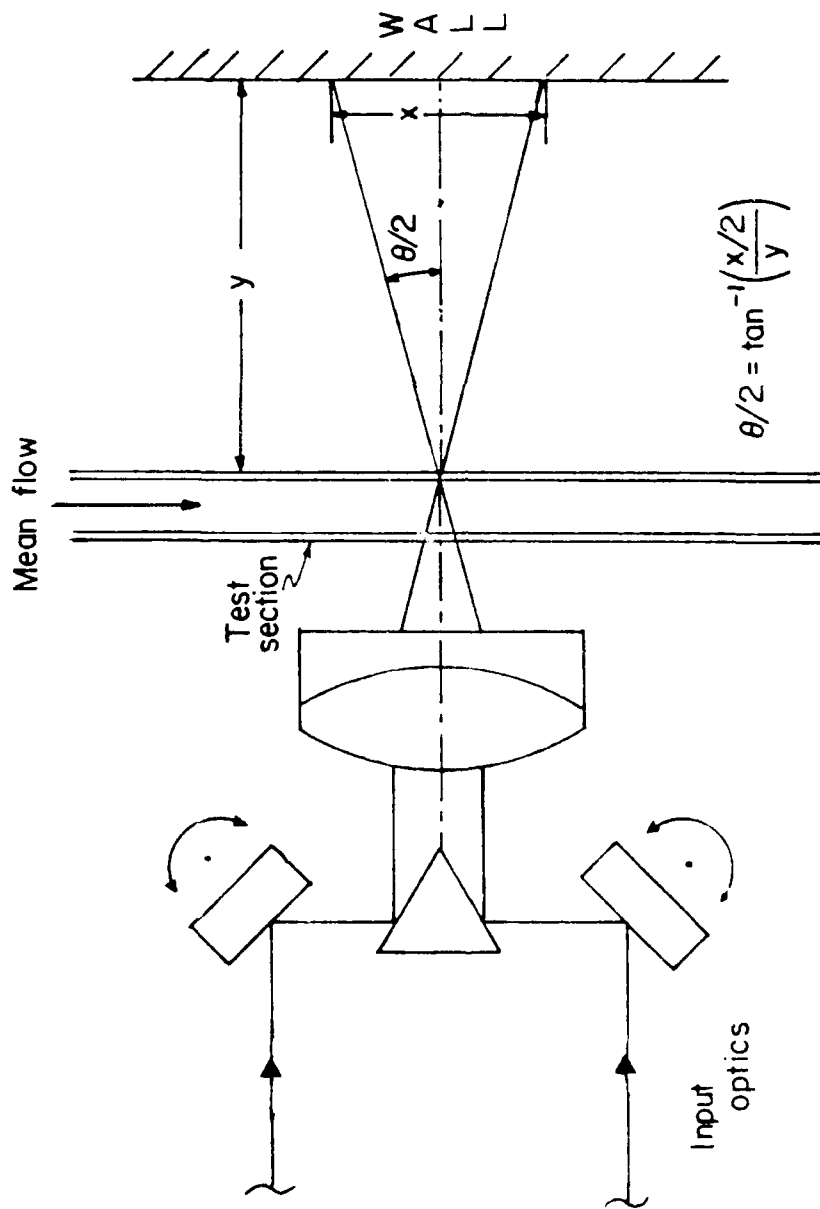


Figure 23. Setup for measuring beam angle

Substitution of the half angle $\theta/2$ into Equation (5) yields a fringe spacing of $4.0606 \mu\text{m} \pm 0.1223 \mu\text{m}$. The seeded particle size was approximately $1 \mu\text{m}$ in diameter.

The net frequency shift employed, f_s , was $10 \text{ MHz} \pm 1 \text{ KHz}$. The frequency shift indicates that the fringes are moving upstream against the mean flow direction and in this case with a velocity of 40.61 m/s .

The output signal of the photomultiplier tube was filtered to remove the "pedestal" and any high frequency noise. A 30 MHz low pass filter and a 3 MHz high pass filter were used. A 16 to 8 fringe comparison ($N = 16$) was used with the accuracy of this comparison set at 3.1 per cent (comparator = 3). This means that the time for a particle to cross 16 fringes is compared with the time for the same particle to cross 8 fringes. An error in the comparison of more than 3.1 per cent results in the measurement being rejected. The value of the allowable comparison error used was the result of preliminary tests. Values above 4 per cent caused the variance of the velocity histogram to be significantly affected by the resulting "bad" data points. The exponent, n , was allowed to float (variable) and was an output of the TSI processor.

The data rate at the TSI processor (number of valid data points per second available for sampling by the microprocessor) was maintained at 20,000 samples per second. This data rate was the result of both seeding DOP particles into the flow through the blower inlet with the seeding system under maximum pressure ($\approx 60 \text{ psi}$) and varying the gain (≈ 5) on the TSI processor slightly. The data rate was maintained by varying the gain with care taken not to distort the signal. The rate

at which the microprocessor was able to sample the available data was at its maximum of 2748 samples per second. Because of the relatively high data rate the actual sampling was at approximately equal time intervals. Each velocity measurement consisted of 4500 samples.

For the data processing each sampled output of the TSI processor, which consists of three digital numbers namely N (cycles/burst), n (exponent) and D_m (digital mantissa), was converted into a frequency f and then a velocity component, V_i , by the following equations

$$f = \frac{N \times 10^9}{D_m \times 2^{n-2}} \quad (6)$$

and

$$V_i = (f - f_s) F_R, \quad (7)$$

where f_s is the frequency shift and F_R is the fringe spacing calculated from Equation (5). The mean and variance of the 4500 individual velocities were then computed from Equations (8) and (9) below.

$$(\bar{V})_\phi = \frac{1}{n} \sum_{i=1}^{4500} (V_i)_\phi, \quad (8)$$

$$(\overline{V^2})_\phi = \frac{1}{n} \sum_{i=1}^{4500} [(V_i)_\phi - (\bar{V})_\phi]^2, \quad (9)$$

where the subscript ϕ denotes the velocity component that is measured, i.e., $\phi = 0^\circ, +30^\circ$, or -30° . In computing the means from Equations (8) and (9) any individual measurements outside a 3σ band were discarded as noise. The number of discarded points was typically about 10 to 15 and consistently less than 50 per data set.

The Appendix describes the flow system coordinates and the method whereby the mean velocities in the streamwise and transverse directions and the turbulence parameters $\sqrt{u'^2}$, $\sqrt{v'^2}$, $\frac{1}{2}(\overline{u'^2} + \overline{v'^2})$, and $\overline{u'v'}$ can be computed from velocity histograms measured in three component directions at each point in the flow. The component directions of 0° , $+30^\circ$, and -30° from the streamwise direction were used. It was found that the data rate drops significantly as the measuring angle increases. The 30° compromise allowed the 20,000 samples per second data rate to be maintained.

Applying the results of the Appendix to the averaged measurements at $\phi = 0^\circ$, $+30^\circ$, and -30° yields

$$\bar{u} = (\bar{V})_{\phi=0} = [(\bar{V})_{\phi=+30} + (\bar{V})_{\phi=-30}]/\sqrt{3}, \quad (10)$$

$$\bar{v} = (\bar{V})_{\phi=+30} - (\bar{V})_{\phi=-30}, \quad (11)$$

$$\sqrt{\overline{u'^2}} = \sqrt{(\overline{V'^2})_{\phi=0}}, \quad (12)$$

$$\sqrt{\overline{v'^2}} = [2(\overline{V'^2})_{\phi=+30} + 2(\overline{V'^2})_{\phi=-30} - 3(\overline{V'^2})_{\phi=0}]^{1/2}, \quad (13)$$

$$\frac{1}{2}(\overline{u'^2} + \overline{v'^2}) = (\overline{V'^2})_{\phi=+30} + (\overline{V'^2})_{\phi=-30} - (\overline{V'^2})_{\phi=0}, \quad (14)$$

and

$$\overline{u'v'} = [(\overline{V'^2})_{\phi=+30} - (\overline{V'^2})_{\phi=-30}]/\sqrt{3} \quad (15)$$

The experimental grid consisted of 180 grid points divided into 10 vertical grid lines (profiles) as shown in Figure 24. Each grid point was spaced approximately 10.1 mm vertically apart while the grid

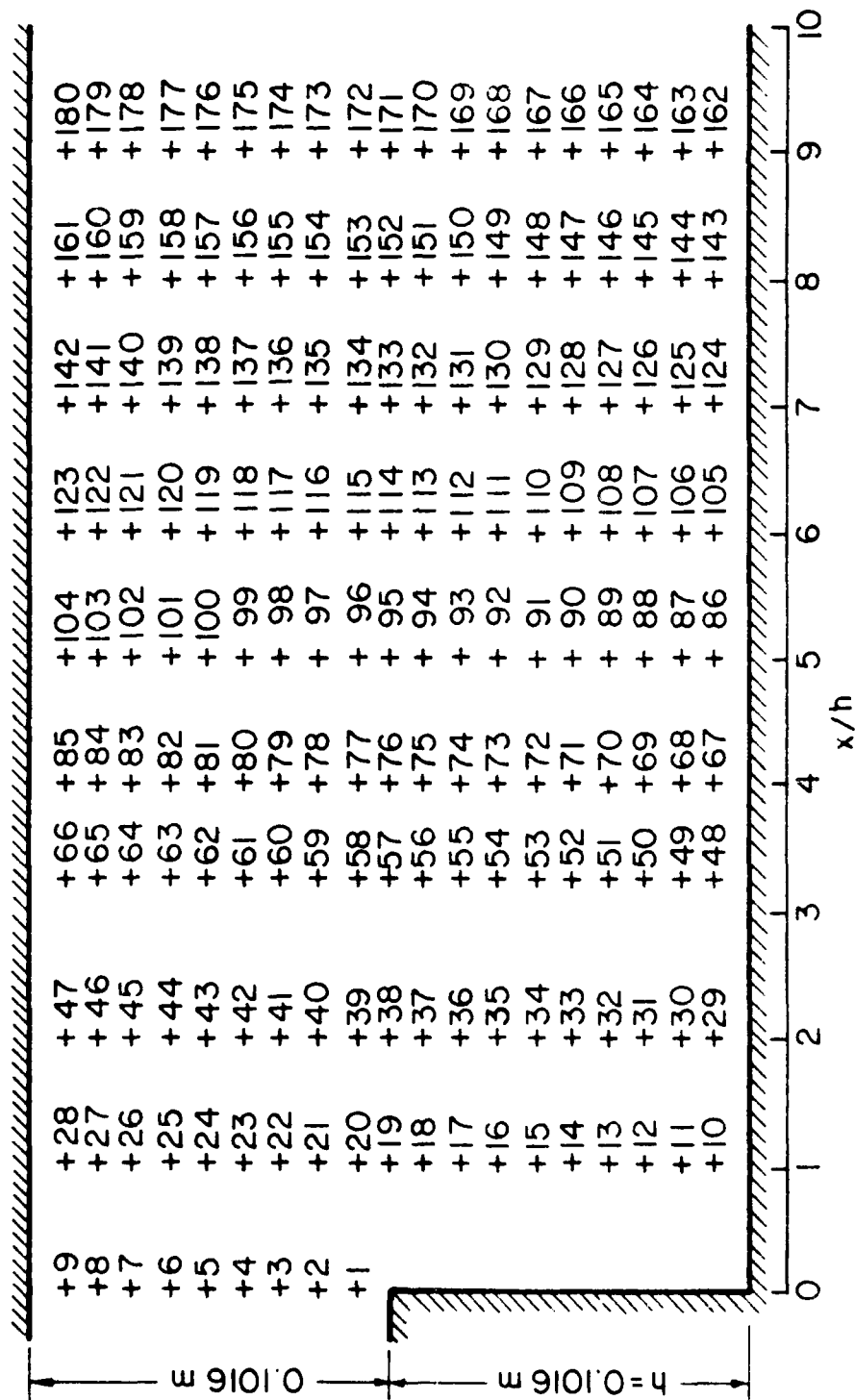


Figure 24. Experimental grid.

line separation was one step height. The exception to this was the grid line at 3.25 step heights. Due to a flange connection optical access was not possible at 3 step heights; therefore that grid line was shifted 0.25 step heights downstream. All measurements were made in the center (spanwise) of the duct, except as noted for the spanwise profiles.

3. Stream Function, ψ

The stream function, ψ , for an incompressible flow is defined by

$$\bar{u} = \frac{\partial \psi}{\partial y} \quad (16)$$

and

$$\bar{v} = - \frac{\partial \psi}{\partial x} . \quad (17)$$

Rearranging Equation (16) and integrating both sides yields

$$\psi = \int_0^y \bar{u}(y) dy + g(x) . \quad (18)$$

By integrating along a vertical line ($x = \text{constant}$) the function $g(x)$ is constant and can be set equal to zero. The integral in Equation (18) was approximated using the trapezoid rule [38]. This yielded a value of ψ at each grid point in the flow field with ψ defined as zero along the step face and bottom wall. Thus,

[38] James, M.L., Smith, G.M., and Woford, J.C., "Applied Numerical Methods for Digital Computation with FORTRAN and CSMP," IEP-A Dun-Donnelly Publisher, New York, Second Edition, 1977.

$$\psi_i = \psi_{i-1} + \frac{y_i - y_{i-1}}{2} (\bar{u}_i + \bar{u}_{i-1}). \quad (19)$$

4. Reattachment Length, x_r

The reattachment length, x_r , was determined by linearly extrapolating a $\bar{u} = 0$ curve to the bottom wall. The $\bar{u} = 0$ curve was located by interpolation between adjacent grid points at which \bar{u} changed sign.

SECTION V

EXPERIMENTAL RESULTS

In this section the results of the pressure and LDV velocity measurements are presented for a Reynolds number (based on step height h and mean streamwise inlet velocity U_m) of 1.68×10^5 . The measured pressure coefficients are compared to the experimental data of Tani et al. [19] ($Re_h = 1.7 \times 10^6$) and Moss et al. [28] ($Re_h = 5 \times 10^4$). The measured reattachment length is also compared with other researcher's measurements. Representative plots of mean velocity and turbulence parameter profiles are presented. The comparison of those measurements with numerical predictions is contained in Section VI. Estimates of measurement uncertainty were made and are discussed.

1. Pressure Coefficient, C_p

a. Pressure Coefficient Distribution

Figure 25 shows the pressure coefficient distribution for six different runs for flow in the two-dimensional single duct step. C_p is defined by Equation (4) and the reference values of P_0 and U_0 are the measured values at $x/h = -1.75$; thus the C_p value is zero there by definition and decreases slightly as the step is approached. The three static pressure measurements on the step face were the same for each run but varied slightly between runs. Therefore, only a single

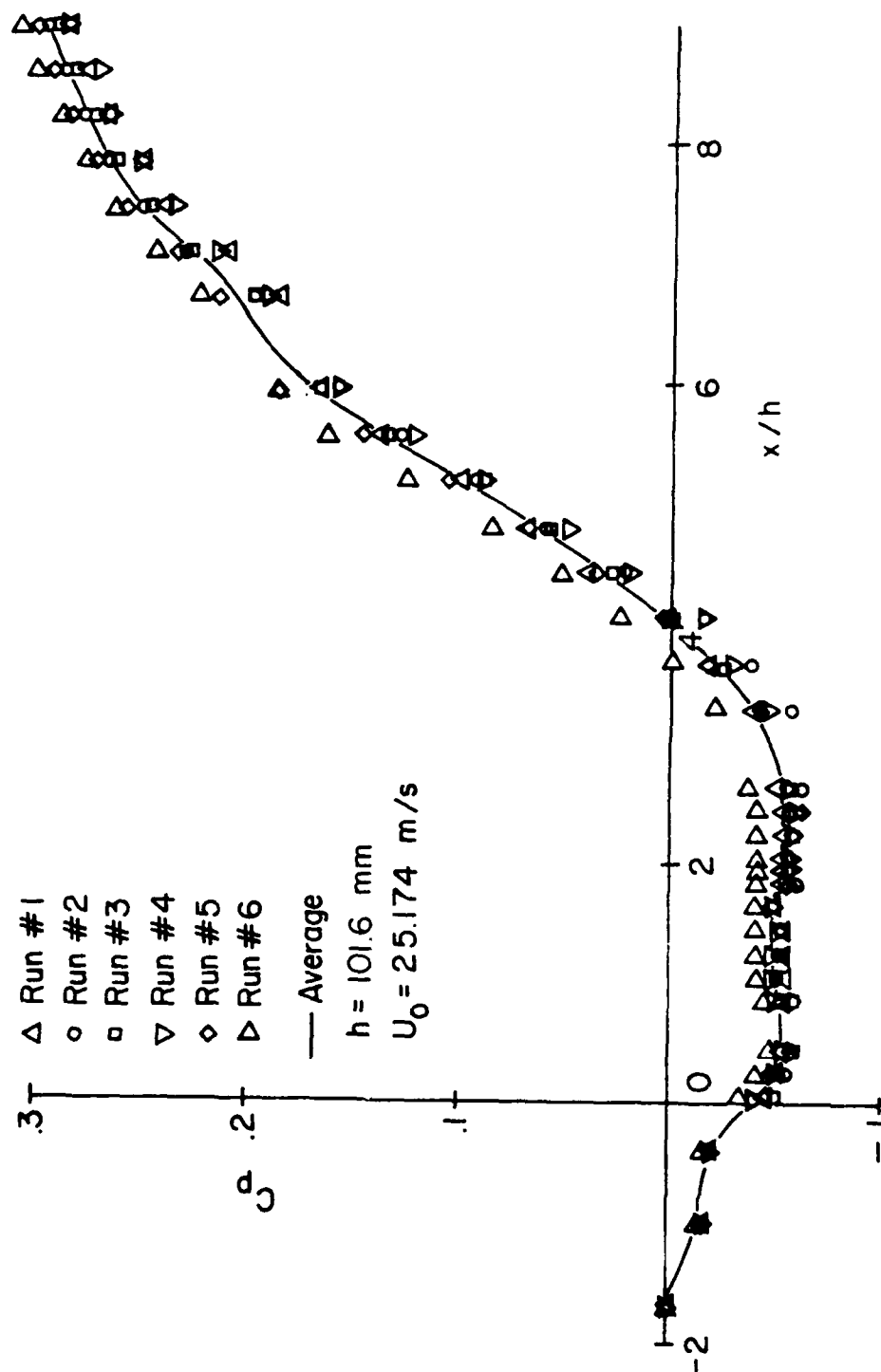


Figure 25. Pressure coefficient distribution for flow over a two-dimensional single duct step.

value is plotted for each run and that value is constant over the step face. Downstream of the step for about three step heights the pressure coefficient is nearly constant at a value of about $-.05$. With the exception of run #6 the slight data scatter is within the accuracy of the manometer readings. Beyond x/h of about 3 the pressure coefficient rises. The spread in the data is a manifestation of the low frequency unsteadiness of the flow, which is directly observable as manometer fluctuations.

Figure 26 is a comparison of the average pressure coefficient for the six runs with the results of Tani et al. [19] and Moss et al. [28]. The absolute values of C_p are expected to be somewhat different since slightly different upstream stations were used to establish reference values of P_o , U_o , and ρ . Qualitatively the results are in fairly good agreement. The peak in the value of C_p that is clearly evident in the works of both Tani et al. and Moss et al. was not reached in the present study. Tani et al. found their reattachment point to be about 7 step heights downstream of the step and just after the maximum value of C_p had been reached. In the present study reattachment occurs at about 7 step heights but is on an increasing C_p curve. The data of Moss et al., however, corresponds to a reattachment location of approximately 5 step heights with the maximum value of C_p occurring at about 6.5 step heights downstream of the step. The differences in the measured results can be partially attributed to the differences in both the step height and the mean streamwise velocity between the experiments. Also, there were significant differences in the flow geometries involved. Both Tani et al. and Moss et al. used channels in which the wall opposite the

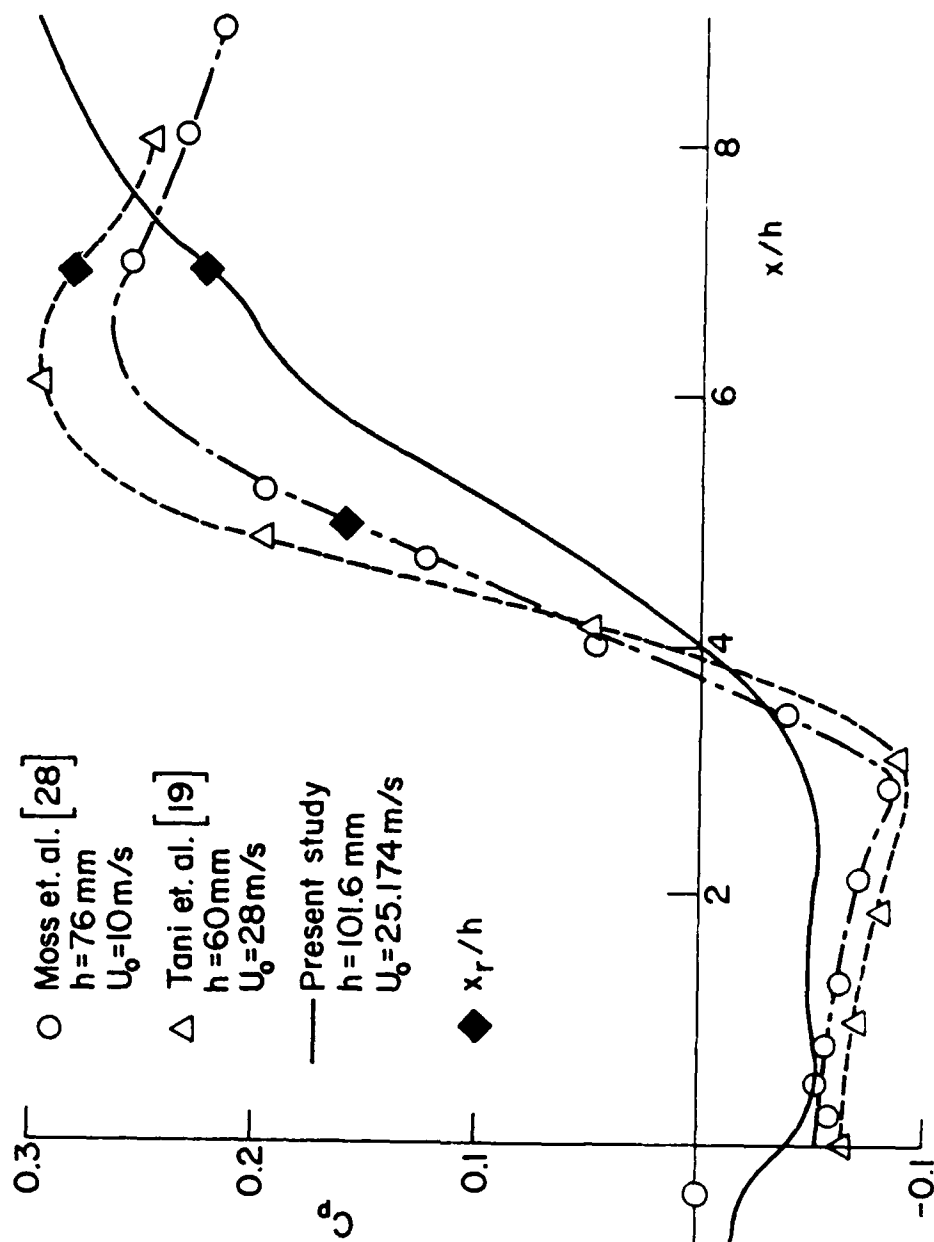


Figure 26. Comparison of measured pressure coefficient distribution with Refs. [19] and [28].

step was a relatively long distance away (9.2 and 11 step heights, respectively). The wall opposite the step in the present study is only one step height away. Also, the width of the channels was different. The present work was in a relatively narrow channel (1 step height) when compared to the models of Tani et al. (16.67 step heights) and Moss et al. (18.05 step heights). Apparently side wall boundary layer growth and more severe three-dimensional effects in the present model slow the rate at which C_p approaches the fully developed value downstream.

Tani et al. [19] found that the effect of the upstream boundary layer thickness on the pressure coefficient was small when $\delta/h \lesssim .3$. In the present case $\delta_s/h \approx .3$ and the effect of the upstream boundary layer thickness on the flow structure is expected to be small.

b. Experimental Error in C_p

The pressure coefficient, C_p , is defined by Equation (4). That is,

$$C_p \equiv \frac{P - P_o}{\frac{1}{2} \rho U_o^2} = \frac{\Delta P}{\frac{1}{2} \rho U_o^2} \quad (20)$$

The analysis of Kline and McClintock [39] provides the following relationship for W_{C_p} , the uncertainty (error) in C_p , as a function of uncertainties in ΔP and U_o ($W_{\Delta P}$ and W_{U_o} , respectively).

[39] Kline, S.J., and McClintock, F.A., "Describing Uncertainties in a Single Sample Experiment," Mechanical Engineering, Vol. 75, pp. 3-8, 1953.

$$W_{C_p} = \left\{ \left[\frac{1}{\frac{1}{2} \rho U_0^2} W_{\Delta P} \right]^2 + \left[- \frac{\Delta P}{\frac{1}{4} \rho U_0^3} W_{U_0} \right]^2 \right\}^{1/2} \quad (21)$$

The uncertainties in the ΔP and U_0 measurements were estimated to be of the order $W_{\Delta P} \approx 0.314$ mm of water and $W_{U_0} \approx 0.082$ m/s so that the uncertainty in C_p is less than ± 0.005 .

2. Mean Velocities \bar{u} and \bar{v} and Streamwise Turbulence Intensity $\sqrt{u'^2}/U_m$

a. Mean Streamwise Velocity, \bar{u}

Figure 27 shows the measured non-dimensionalized mean streamwise velocity profiles at the inlet and four representative locations downstream of the step. The non-dimensionalizing quantity U_m (24.83 m/s) is the average of the nine experimentally measured values of \bar{u} at $x/h = 0$.

The inlet profile ($x/h = 0$) is fairly flat with a maximum velocity of 25.865 m/s. At the final profile ($x/h = 9$) the maximum velocity is 20.966 m/s. This 20 per cent decrease was also observed by Smyth [27] in a similar series of measurements. The maximum reverse flow velocity is -5.8 m/s and occurred 10.1 mm from the bottom wall at $x/h = 4$. This is approximately one-fifth the maximum velocity at the inlet. The profile at $x/h = 9$ is asymmetric indicating that "fully developed" flow has not yet been attained.

Figure 28 is a plot of the integrated mass flow, \dot{m} , for each measured profile. The integration was by the trapezoid rule. The integrated value was approximately the same across the inlet

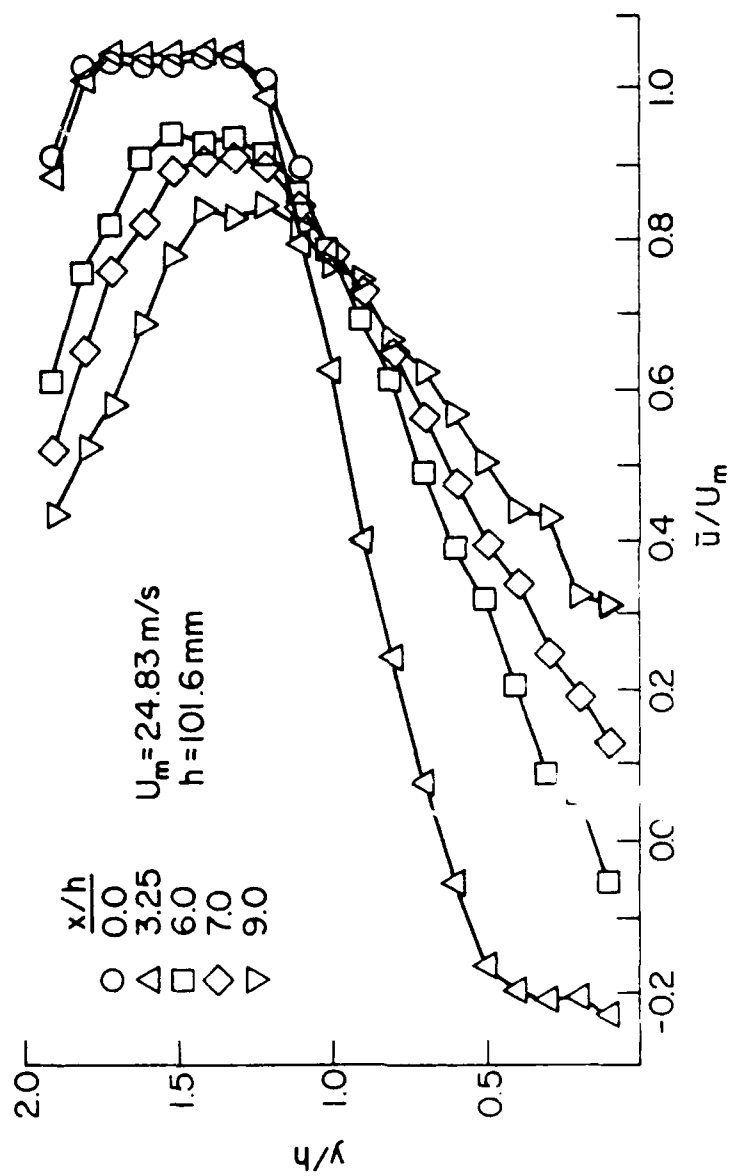


Figure 27. Measured streamwise velocity profiles.

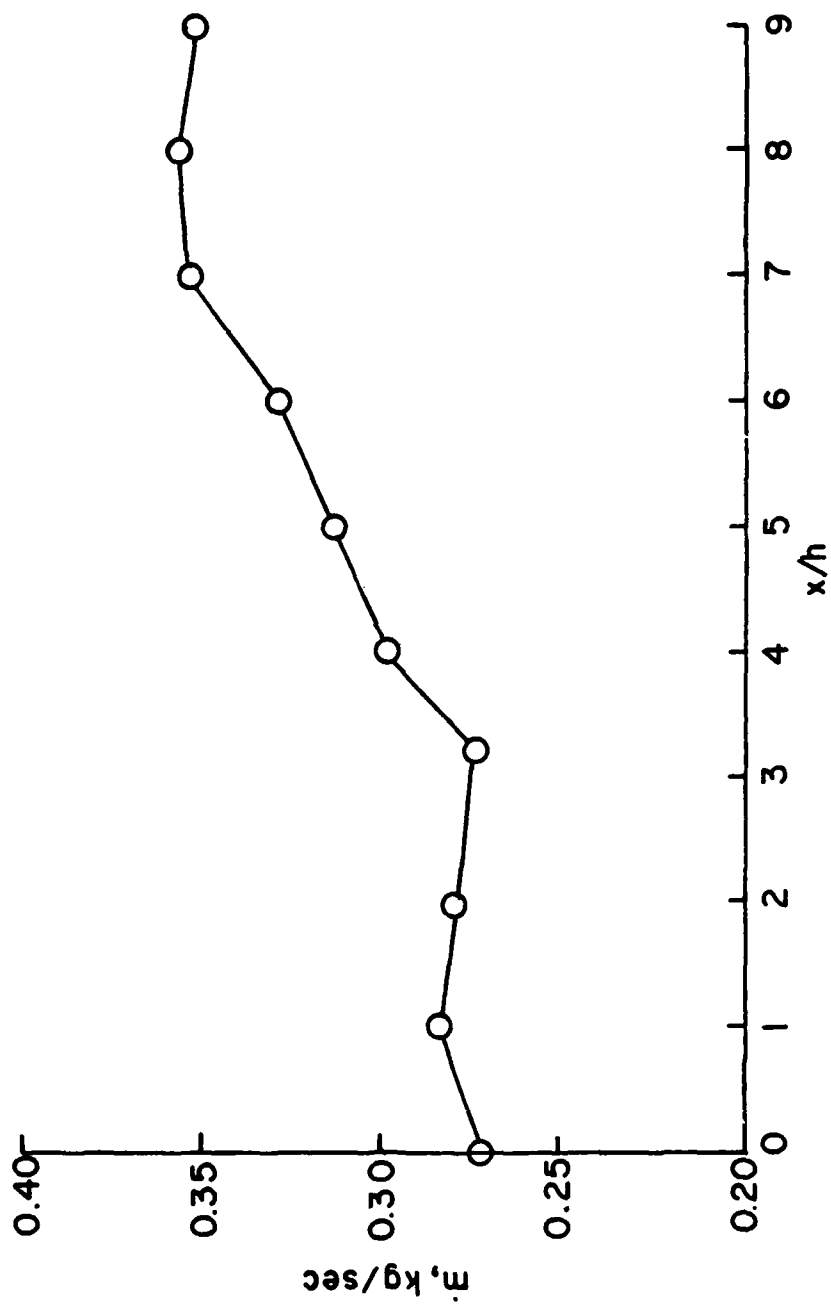


Figure 28. \dot{m} vs. x/h .

(.271 kg/sec) and the first three profiles and then increased substantially to a value of .353 kg/sec at $x/h = 9$. This 30 per cent "increase" in \dot{m} is disturbing. The \bar{u} -profiles presented by Smyth [27] (Figure 8) appear to show a similar "mass flow increase" but integrated mass flow values were not presented.

It has been shown that individual realization LDV measurements as were made in the present study may be subject to certain bias errors. A complete discussion of bias errors is beyond the present work but can be found in Ref. [40]. Suffice it to say that the LDV parameters, that is, frequency shift, data rate, and sample rate were chosen to reduce bias errors as much as possible. Bias errors do not appear to be a significant part of the mass flow discrepancy.

Boundary layer growth along the side walls could contribute to the mass flow discrepancy. Spanwise measurements at three stations in the flow field are presented in Figure 29 and show some sidewall boundary layer growth but not enough to account for the total discrepancy.

Apparently three-dimensional effects are very important in this flow geometry. The visual observations of Goldstein et al. [10] showed the three-dimensional nature of this flow geometry (Figure 3) with entrainment of flow from regions in the flow field other than the plane of the centerline (spanwise).

- [40] Thompson, H.D., and Flack, R., Jr., "An Application of Laser Velocimetry to the Interpretation of Turbulent Structure," Proceedings of the ISL/AGARD Workshop on Laser Anemometry, German-French Research Institute, Pfeifer, H., and Haertig, J., editors, St.-Louis, France, 1976.

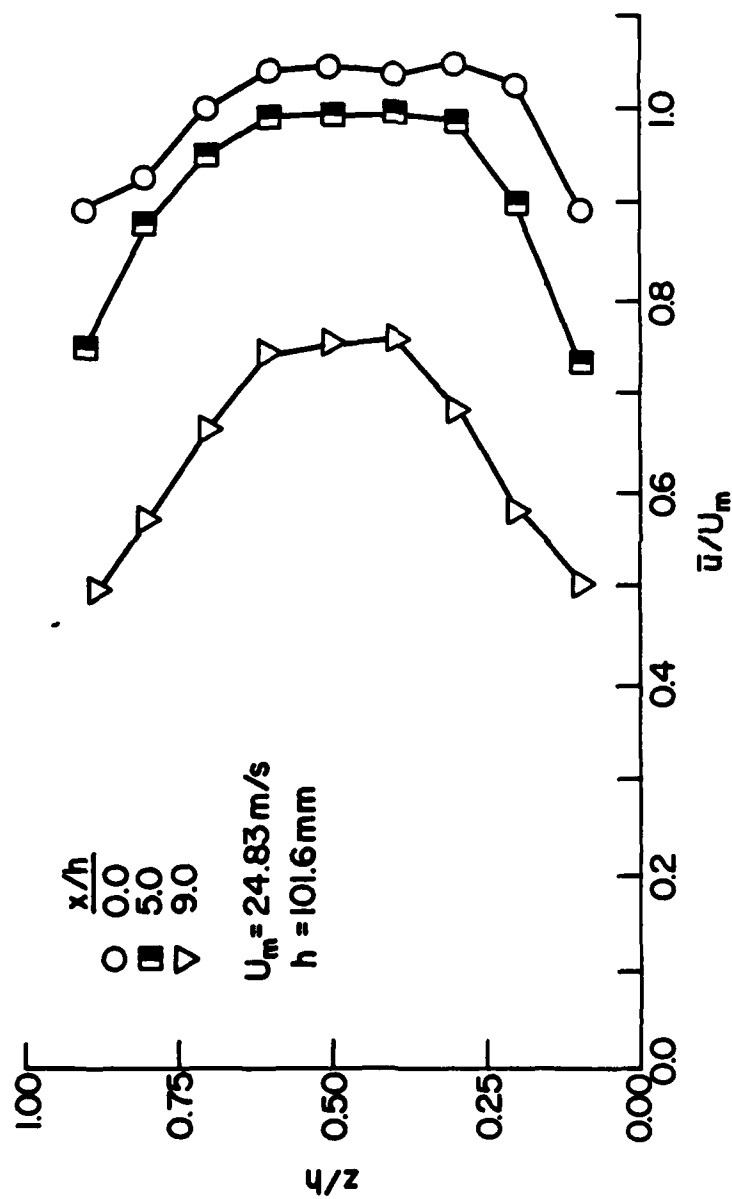


Figure 29. Measured spanwise velocity profiles.

The mean streamwise velocity profiles are found to be in good agreement with the profiles presented by Smyth [27] (shown in Figure 8) and others [11,19].

b. Reattachment Length, x_r

The reattachment point was determined by linearly extrapolating the $\bar{u} = 0$ contour to the lower wall boundary. The measured reattachment was 6.94 step heights downstream from the step face. This is well within the range described by Back and Roschke [15], i.e., 6-8 step heights, and is in generally good agreement with other experimental results.

c. Stream Function, ψ

Figure 30 shows the stream function contours. The reader should note the difference between the horizontal and vertical scales. To partially compensate for the apparent mass flow discrepancy the stream function is non-dimensionalized at each x/h station. That is at each x station

$$\psi^* \equiv \psi / \psi_{TOP} . \quad (22)$$

The recirculation region is clearly defined with the location of the center of recirculating flow at about 3.25 step heights downstream of the step face and .6 step heights above the bottom wall.

d. Mean Transverse Velocity, \bar{v}

The mean velocity measurements at $\phi = \pm 30^\circ$ allow the mean transverse velocity, \bar{v} , to be determined at each grid point. Hence, in combination with \bar{u} the velocity vector can be determined. Figure 31

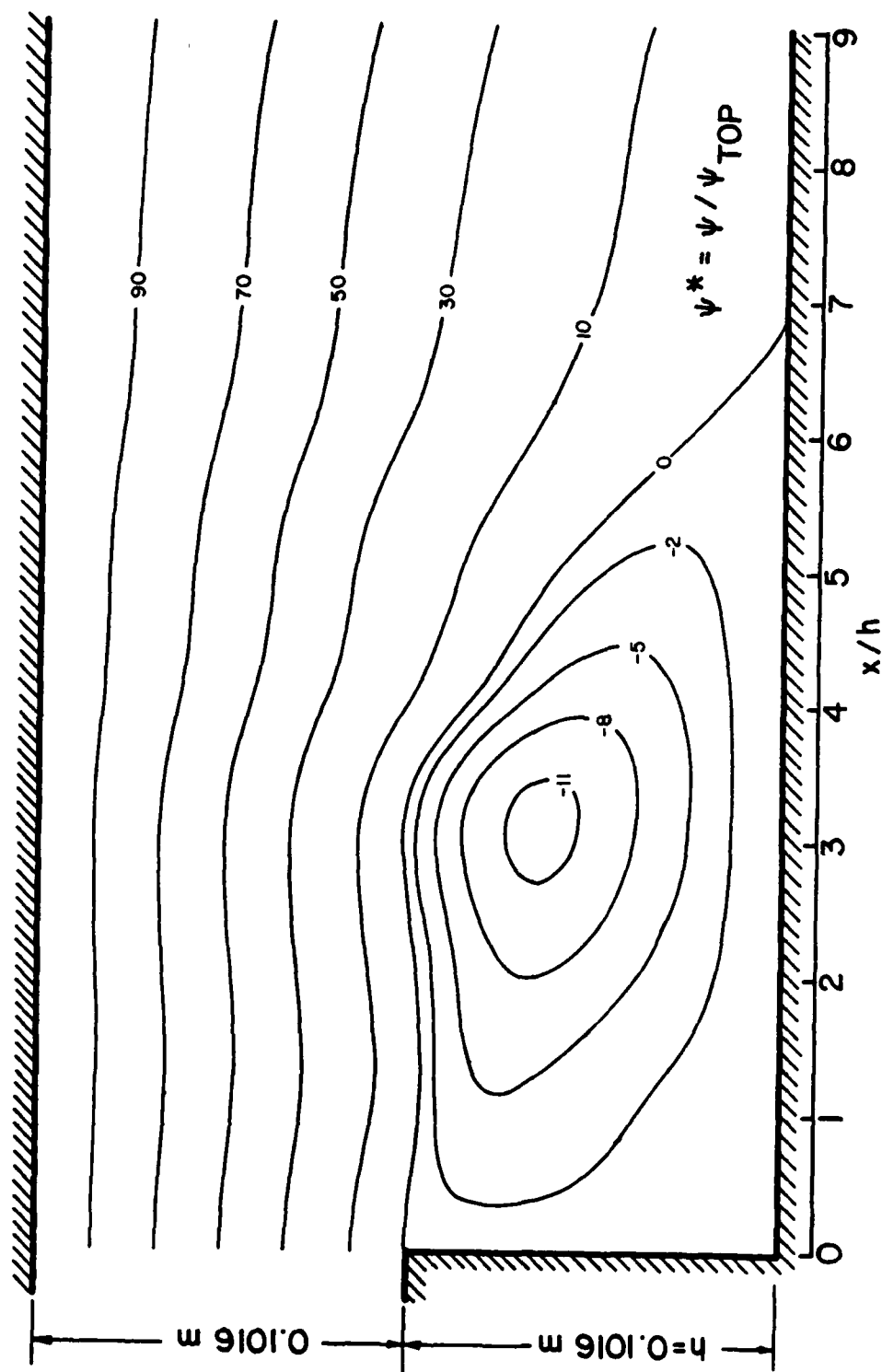


Figure 30. Measured stream function contours.

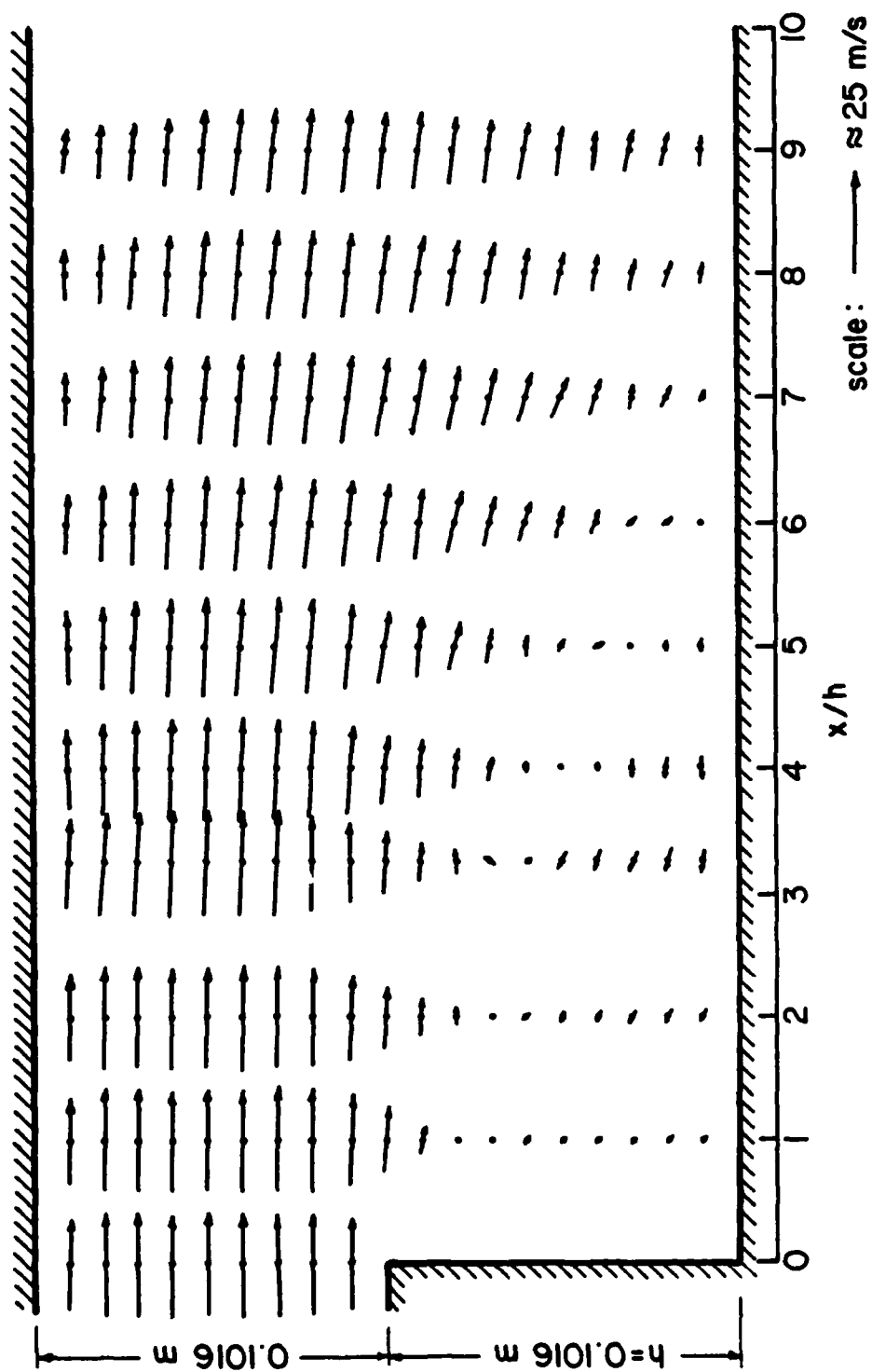


Figure 31. Experimental velocity vector plot.

shows the velocity vectors for the flow field. The magnitude of the reverse flow in relation to the inlet flow can clearly be seen. The flow at $x/h = 9$ is still directed toward the bottom wall and changing in magnitude, indicating that fully developed conditions have not been reached.

e. Streamwise Turbulence Intensity, $\sqrt{u'^2}/U_m$

Figure 32 is a plot of streamwise turbulence intensity profiles, $\sqrt{u'^2}/U_m$, at the inlet and at four streamwise locations. The minimum value occurs at the inlet and is about 1.5 per cent. The increase with x at the top measuring station is an indication of boundary layer growth along the top wall. The intensity in the free shear layer has a maximum value of 19 to 20 per cent over a range from 3.25 step heights to reattachment, Smyth [27] found a free shear layer with the maximum value of about 17.5 per cent (based on U_m of the present study) from a point 1.2 step heights downstream of the step face to reattachment ($x_r/h = 9$). Downstream of reattachment the free shear layer spreads toward the bottom wall with a subsequent decrease in the maximum intensity. The turbulence intensity near the bottom wall reaches a maximum value of 16 per cent just upstream of the reattachment point with a subsequent decrease after reattachment. The overall streamwise turbulence intensity results are in good agreement with the results of Smyth [27] shown in Figure 9.

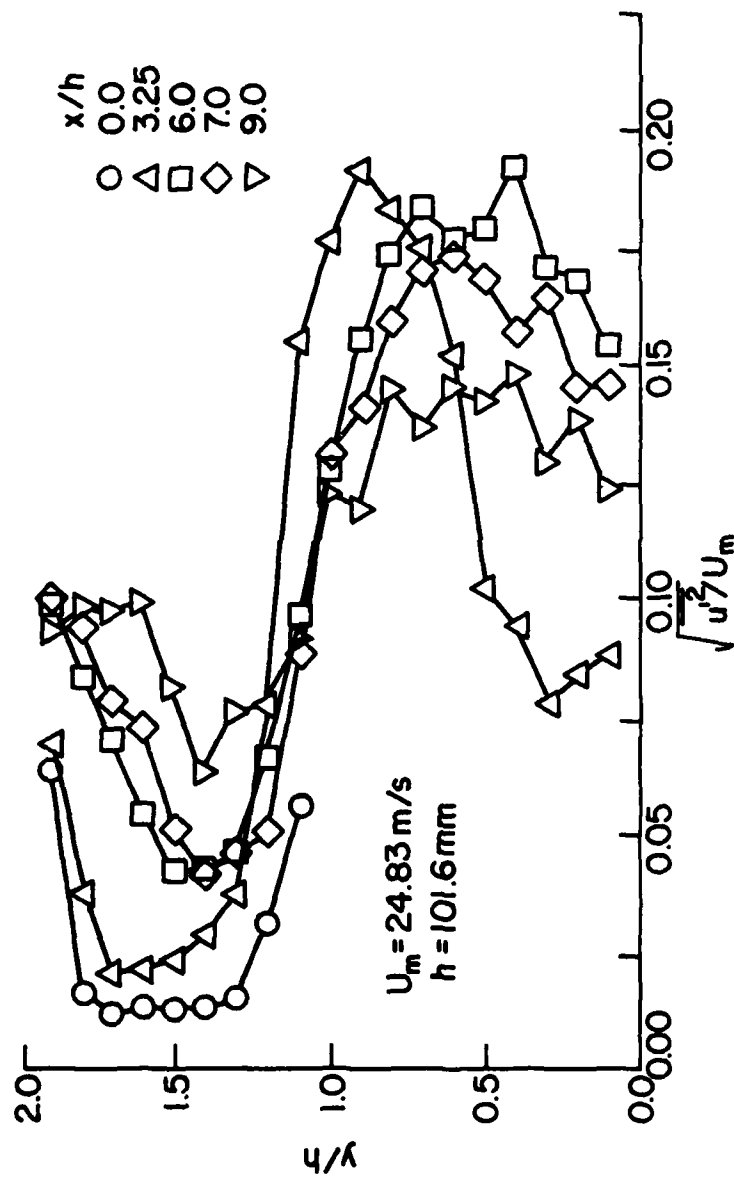


Figure 32. Measured streamwise turbulence intensity profiles.

3. Correlated Turbulence Parameters,

$$\sqrt{v'^2}/U_m, \frac{1}{2}(\overline{u'^2} + \overline{v'^2}), \overline{u'v'}$$

In Figure 33 the inlet and four downstream profiles of the transverse turbulence intensity $\sqrt{v'^2}/U_m$ are shown. The transverse turbulence intensity is calculated from LDV measurements at $\phi = 0^\circ, +30^\circ, \text{ and } -30^\circ$ in accordance with Equation (13). Even though the general trend of the measurements in Figure 33 is in accordance with the expected trend the scatter in the data, particularly in the recirculation region, is very large. In fact, the data is worse than is shown since about 10% of the measurements produced negative values of $\overline{v'^2}$ and those points have been omitted from Figure 33. A discussion of the data scatter as it relates to uncertainty in the measurements and unsteadiness in the flow is presented in Section V-4.

Figure 34 is the turbulent kinetic energy profiles and Figure 35 is a contour map of those profiles for the entire flow. Again the data scatter is large and accounts in large measure for the waviness in the contour plot. Qualitatively, the turbulent kinetic energy profiles appear to be in good agreement with those presented by Smyth [27].

Figure 36 is a plot of selected Reynolds stress ($\overline{u'v'}$) contours for the flows. The Reynolds stress in the core region is negligible while values greater than zero were obtained in the top wall region. This is simply a result of the orientation of the coordinate system relative to the top wall boundary layer. The peak Reynolds stress for each profile upstream of reattachment occurs at the edge of the recirculation zone. This agrees with the data of Smyth [27] shown in

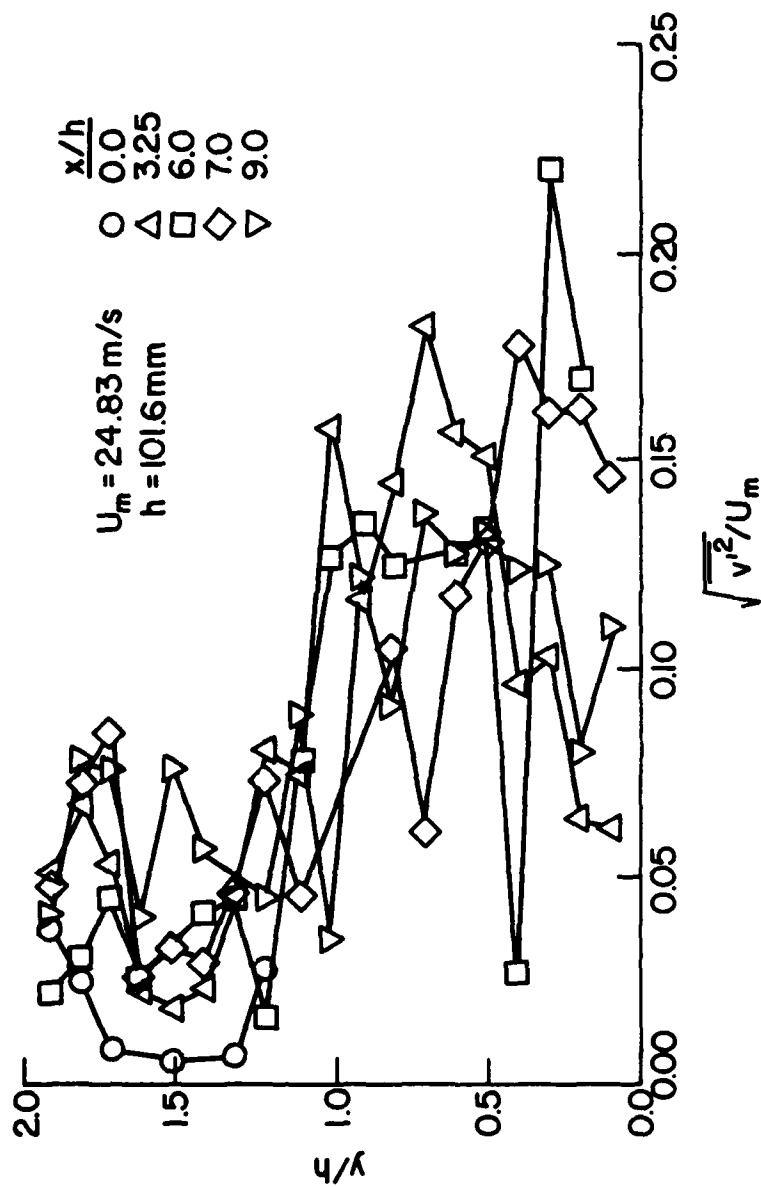


Figure 33. Measured transverse turbulence intensity profiles.

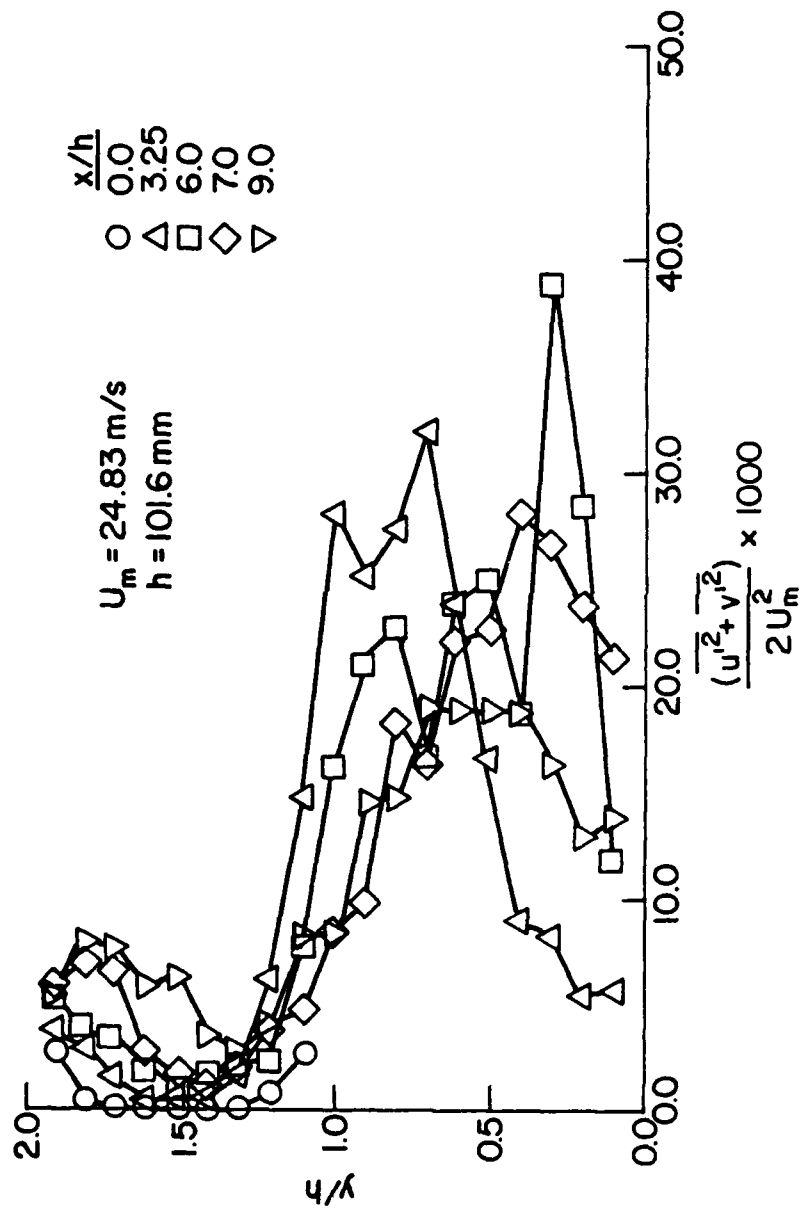


Figure 34. Measured turbulent kinetic energy profiles.

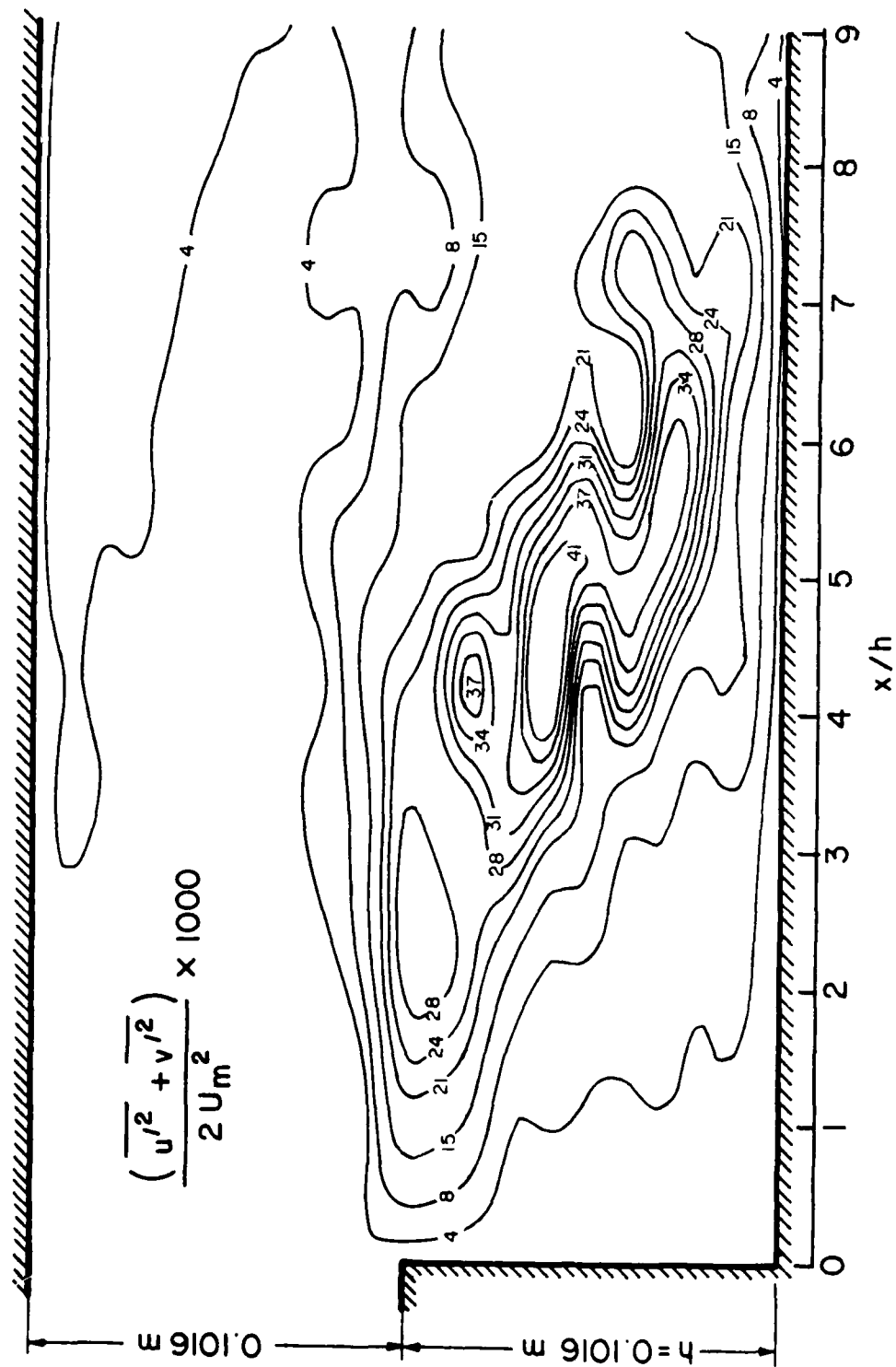


Figure 35. Measured turbulent kinetic energy contours.

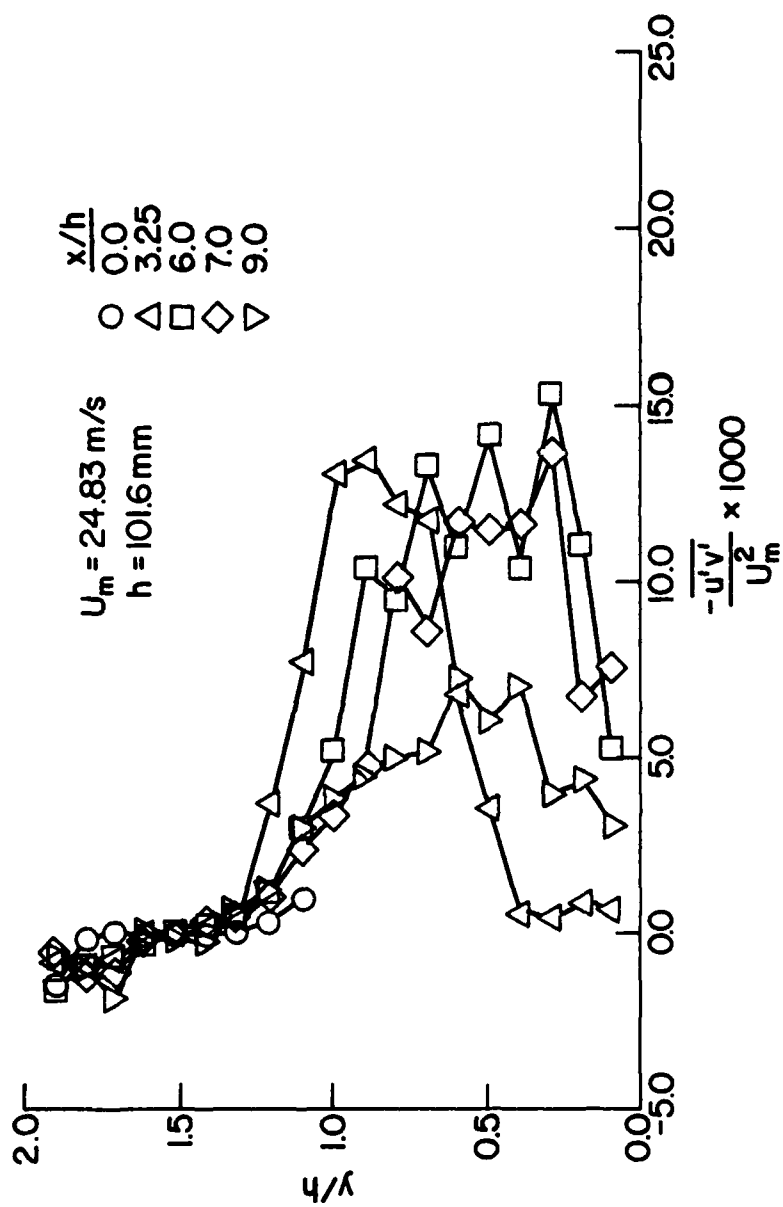


Figure 36. Measured Reynolds stress profiles.

Figure 10. The overall agreement with Smyth's data is good though his maximum value cited is about 40 per cent lower than the maximum value of the present data. The contours of constant Reynolds stress are shown in Figure 37.

4. Data Scatter Due to Uncertainty in LDV Measurements

There are at least three types of error and/or uncertainty that can produce scatter in the LDV derived data. First, there is the absolute error in a single realization measurement resulting from both electronic noise and limitations on measurement accuracy. Second, there is a statistically determined uncertainty in average quantities when a finite number of individual measurements are used. Finally, there is a "scatter" in the measurements due to both low frequency unsteadiness of the flow and errors in repositioning the probe volume for non-simultaneous measurements at $\phi = 0^\circ$, $+30^\circ$, and -30° . This "scatter" is most pronounced in regions of steep gradients.

Additionally, it is well known that small errors are amplified by differencing two or more nearly equal values, as for example in the determination of \bar{v} and $\sqrt{v'^2}$ (see Equations (11) and (13)). These sources of error and/or uncertainty for the present measurements are discussed in more detail below.

a. Single Measurement Error

Errors in the absolute value of velocity from a single LDV measurement could result from electronic noise, uncertainty in setting the upstream reference velocity, uncertainty in measuring the fringe spacing, and clock timing errors in the TSI processor. Other possible

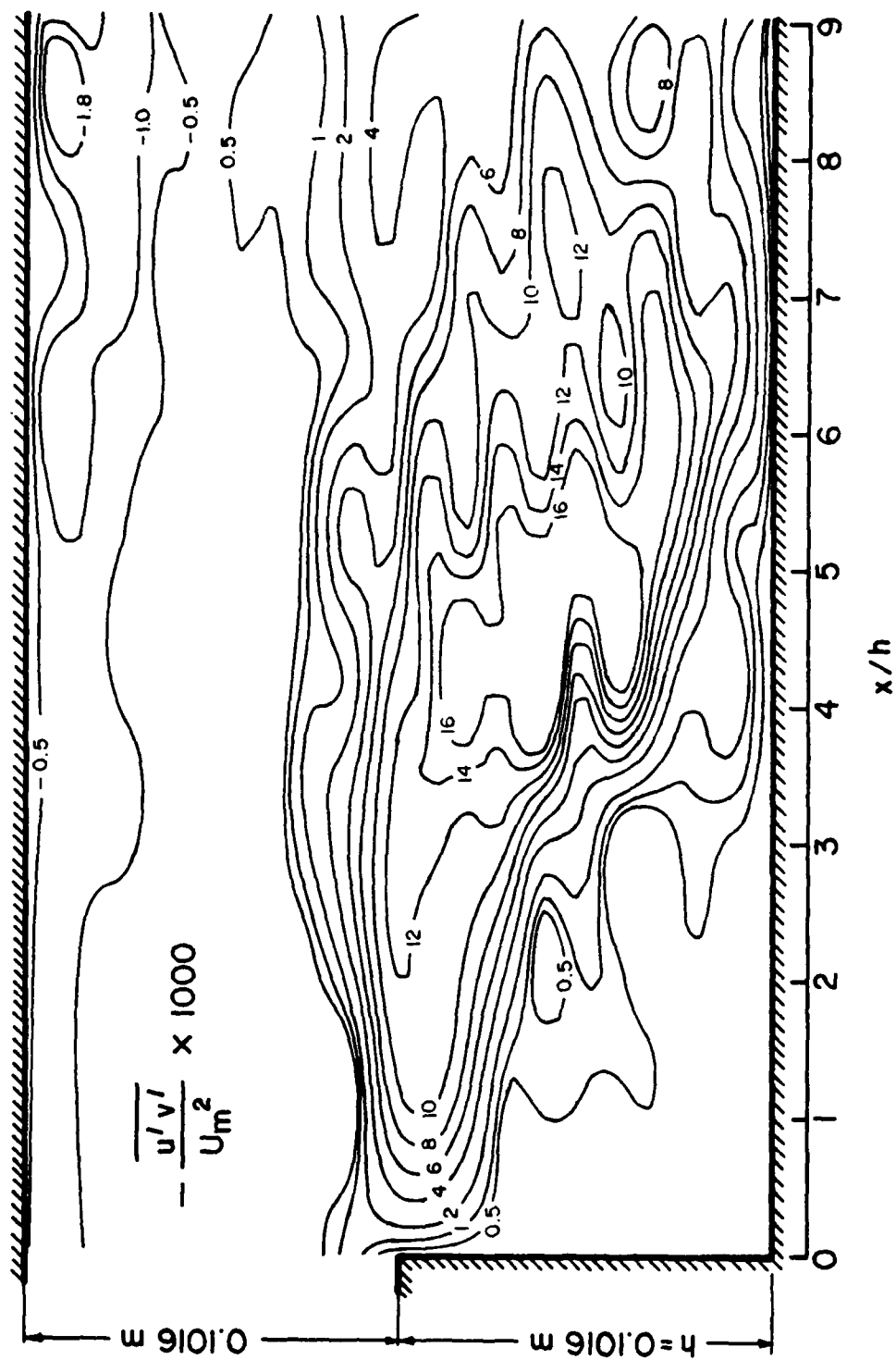


Figure 37. Measured Reynolds stress contours.

sources of error such as uncertainty in the shift frequency were checked and found to be very small.

By proper filtering of the LDV signal the errors from electronic noise are greatly reduced. The measurements in the laminar flow above the step showed a low turbulence intensity (about 1.5%) which indicates that noise is not a problem. In addition, measurements outside a 3σ band were considered to be the result of noise and were discarded.

The upstream reference velocity was adjusted periodically between measurements. It is estimated that the pitot tube monitoring allowed the reference velocity to be adjusted to ± 0.3 per cent for all runs.

Errors in the measurement of fringe spacing could be as much as 3 per cent; this error would produce a constant error in the absolute value of average velocities but would not effect the variance measurements.

Clock resolution could produce an error in the velocity measurement of a particle at 24 m/s with 10 MHz frequency shift and 16 cycles/burst of about .5 per cent. The error is less for lower velocities. Tests of the TSI processor showed that the clock error is not a \pm error but is biased toward longer times or lower velocities.

b. Uncertainty in Ensemble Measurements

Mean velocities and turbulence intensities calculated from a finite number of sampled velocities are subject to statistical sampling uncertainty. Generally, the error in the mean velocity is proportional to the ratio of the rms velocity to the square root of the number of samples. The error in the rms velocity is inversely proportional to the

square root of the number of samples. Results of this type of analysis are provided by Yanta [41] who gave the uncertainties in ensemble measurements for different mean and rms velocities in graphical form.

The uncertainty in mean velocity for 4500 samples and a 95 per cent confidence level is less than 2 per cent for most of the flow field. Note that when the average velocity is zero, as it will be at some points in the recirculation region, a percentage error based on the average velocity is meaningless.

Similarly, an uncertainty of about 2 per cent is present in the measured turbulence intensities for 4500 samples and a 95 per cent confidence level. In terms of the present work, the uncertainty in both a mean velocity and turbulence intensity measurement for $\phi = 0^\circ$, $+30^\circ$, and -30° at any point in the flow field is approximately 2 per cent.

The mean transverse velocity, \bar{v} , is calculated from the difference of the mean velocities at $\phi = +30^\circ$ and $\phi = -30^\circ$ (Equation (11)). Since the value of \bar{v} is determined from the difference in two measurements, the per cent of uncertainty in \bar{v} may be high when the two measurements are nearly equal. To illustrate this point, Table 9 provides representative values of \bar{v} along with corresponding maximum and minimum values based on a 2 per cent uncertainty in the measured mean velocities. As Table 9 illustrates the absolute uncertainties in \bar{v} are twice the average absolute uncertainty in \bar{V}_ϕ , but when the two values of \bar{V}_ϕ are nearly equal the per cent uncertainty in \bar{v} can be very large.

[41] Yanta, W.J., "The Use of the Laser Doppler Velocimeter in Aerodynamic Facilities," AIAA Paper 80-0435, Presented at AIAA Aerodynamic Testing Conference, 18-20 March, 1980.

Table 9. Uncertainty in \bar{v} for 2 per cent uncertainty in $(\bar{V})_{\phi}$.

Grid Point Number	$(\bar{V})_{\phi=+30}$ (m/s)	$(\bar{V})_{\phi=-30}$ (m/s)	Average Absolute Uncertainty in $(\bar{V})_{\phi}$ (m/s)	\bar{v} (m/s)	\bar{v}_{\min} (m/s)	\bar{v}_{\max} (m/s)	Absolute Uncertainty in \bar{v} (m/s)	Per cent Uncertainty
34	-1.282	-3.291	$\pm .046$	2.009	1.918	2.100	$\sim \pm .091$	± 4.5
50	-3.587	-5.558	$\pm .091$	1.991	1.805	2.174	$\sim \pm .184$	± 9.2
49	-4.086	-5.168	$\pm .093$	1.082	.897	1.267	$\sim \pm .185$	± 17.1
58	17.782	17.705	$\pm .355$.077	-.633	.787	$\sim \pm .710$	± 922.1
59	20.864	21.392	$\pm .423$	-.528	.317	-1.373	$\sim \pm .845$	± 160.0
80	21.569	22.615	$\pm .442$	-1.022	-.162	-1.930	$\sim \pm .884$	± 86.5
159	14.413	15.956	$\pm .304$	-1.533	-.926	-2.140	$\sim \pm .607$	± 100.0
96	17.502	19.507	$\pm .370$	-2.005	-1.265	-2.745	$\sim \pm .740$	± 39.6
117	18.662	21.172	$\pm .398$	-2.510	-1.713	-3.307	$\sim \pm .797$	$\pm .318$
111	9.132	12.244	$\pm .214$	-3.112	-2.684	-3.540	$\sim \pm .428$	$\pm .138$

The magnification of the uncertainty in the transverse turbulence intensity values as calculated from Equation (13), (repeated here for convenience) is even more severe.

$$\sqrt{\overline{v'^2}} = [2(\overline{V'^2})_{\phi = +30} + 2(\overline{V'^2})_{\phi = -30} - 3(\overline{V'^2})_{\phi = 0}]^{1/2} \quad (13)$$

In fact the uncertainty of 2 per cent in the $(\sqrt{\overline{V'^2}})_{\phi}$ measurements resulted in $\overline{v'^2}$ values less than zero at approximately 10 per cent of the experimental grid points. There did not appear to be any pattern in the locations for which this occurred and, in fact, the result was not reproducible. That is, $\overline{v'^2} < 0$ occurred at different locations each time a series of measurements was repeated. Table 10 is a tabulation of the measured values for $\overline{V'^2}$ at $\phi = 0^\circ$, $+30^\circ$, and -30° for a portion of the $x/h = 6$ grid line, and further illustrates the range of uncertainty for the $\overline{v'^2}$ determination. Notice that a 2 per cent uncertainty in $(\sqrt{\overline{V'^2}})_{\phi}$ corresponds to a 4 per cent uncertainty in $(\overline{V'^2})_{\phi}$.

Table 10 illustrates that the relatively small uncertainty in the measured values of $(\overline{V'^2})_{\phi}$ can result in very large fluctuations in the derived values of $\sqrt{\overline{v'^2}}$. The scatter is illustrated in Figure 33.

Finally, it should be noted that particularly in regions of steep gradients the "errors" that arise from non-simultaneous measurements at $\phi = 0^\circ$, $+30^\circ$, and -30° are also magnified in the determination of derived quantities such as $\sqrt{\overline{v'^2}}$. These "errors" result from both the flow unsteadiness and the errors in repositioning of the probe volume in the flow field. The extent to which this has effected the data was not determined but it appears to be a problem at a few points in the shear layer.

Table 10. Uncertainty in $\overline{v'^2}$ for 4 per cent uncertainty in $(\overline{v'^2})_\phi$.

Grid Point Number	$\overline{u'^2}$ (m ² /s ²)	$(\overline{v'^2})_{\phi=+30}$ (m ² /s ²)	$(\overline{v'^2})_{\phi=-30}$ (m ² /s ²)	Average Absolute Uncertainty in $(\overline{v'^2})_\phi$ (m ² /s ²)	$\overline{v'^2}$ (m ² /s ²)	$\overline{v'^2}_{\max}$ (m ² /s ²)	$\overline{v'^2}_{\min}$ (m ² /s ²)	Absolute Uncertainty in $\overline{v'^2}$ (m ² /s ²)	Per cent Uncertainty
105	14.659	8.097	13.780	±.487	-.226	3.286	-3.832	~±3.509	1552.6
106	17.463	11.622	23.443	±.700	17.745	22.642	12.840	~±4.901	27.6
107	18.049	12.838	29.219	±.801	29.969	35.497	24.436	~±5.531	18.5
108	22.751	11.622	22.727	±.761	.460	5.923	-5.033	~±5.478	1190.8
109	19.943	10.085	25.207	±.735	11.087	16.259	5.850	~±5.204	46.9
110	19.337	11.137	22.893	±.712	10.033	15.092	5.006	~±5.043	50.3
111	20.827	10.922	22.093	±.717	3.549	8.689	-1.591	~±5.140	144.8

SECTION VI

NUMERICAL ANALYSIS AND COMPARISON

To provide a basis for comparison the CHAMPION 2/E/FIX computer code of Pun and Spalding [42] was adapted to the problem geometry and run. This code uses the $k \sim \epsilon$ turbulence model of Launder and Spalding [31] as well as a modified version of the SIMPLE algorithm as described by Patankar and Spalding [43].

1. Background

The 2/E/FIX code computes the solution of elliptic partial differential equations of the form

$$\frac{\partial}{\partial x} (\rho \bar{u} \Phi) + \frac{1}{r} \frac{\partial}{\partial r} (\rho r \bar{v} \Phi) = S_{\Phi} + \frac{\partial \Phi}{\partial x} \left(\Gamma_{\Phi} \frac{\partial \Phi}{\partial x} \right) + \frac{1}{r} \frac{\partial \Phi}{\partial r} \left(\Gamma_{\Phi} r \frac{\partial \Phi}{\partial r} \right) \quad (23)$$

where $r = 1$ converts the equation from cylindrical to rectangular Cartesian form, Φ is the dependent variable, Γ_{Φ} is the exchange

-
- [42] Pun, W.M., and Spalding, D.B., "A General Computer Program for Two-Dimensional Elliptic Flows," Imperial College Mechanical Engineering Department Report No. HTS/76/2.
 - [43] Patankar, S.V., and Spalding, D.B., "A Calculation Procedure for Heat, Mass and Momentum Transfer in Three-Dimensional Parabolic Flows," International Journal of Heat and Mass Transfer, Vol. 15, pp. 1787-1806, Pergamon Press, 1972.

coefficient, and S_ϕ is the source term. Equation (23) represents a two-dimensional time-averaged form of the Navier-Stokes equations and the supplementary transport equation. The turbulent nature of the flow is described by the $k \sim \epsilon$ model of Launder and Spalding [31]. This model assumes isotropic diffusion with the effective viscosity, μ_{eff} , being the sum of the laminar and turbulent contributions. That is,

$$\mu_{eff} = \mu_{lam} + \mu_t . \quad (24)$$

The dependent variables, ϕ , and the corresponding values of S_ϕ and Γ_ϕ for the governing conservation equations are listed in Table 11. These, when substituted into Equation (26), yield the continuity, axial and radial momentum, turbulent kinetic energy, and energy dissipation rate equations. The 2/E/FIX codes solves this set of equations with appropriate boundary conditions and auxiliary algebraic equations.

The finite difference equations as well as the solution algorithm are described in Ref. [42]. Upwind differencing is employed and the solution of the finite difference equations is accomplished by a tri-diagonal matrix algorithm. In order to achieve numerical stability under relaxation is used.

Five "constants" are required for the numerical implementation of Equation (23) including a value for C_D from which the turbulent viscosity is evaluated.

$$\mu_t = C_D \rho k^2 / \epsilon . \quad (25)$$

Table 11. Conservation equations corresponding to Equation (23).

Conservation of	ϕ	Γ_ϕ	S_ϕ
Mass	1	0	0
Axial momentum	\bar{u}	μ_{eff}	$\frac{\partial}{\partial x} (\mu_{\text{eff}} \frac{\partial \bar{u}}{\partial x}) + \frac{1}{r} \frac{\partial}{\partial r} (\mu_{\text{eff}} r \frac{\partial \bar{v}}{\partial x}) - \frac{\partial p}{\partial x}$
Radial momentum	\bar{v}	μ_{eff}	$\frac{\partial}{\partial x} (\mu_{\text{eff}} \frac{\partial \bar{v}}{\partial x}) + \frac{1}{r} \frac{\partial}{\partial r} (\mu_{\text{eff}} r \frac{\partial \bar{v}}{\partial r}) - 2\mu_{\text{eff}} \frac{\bar{v}}{r^2} - \frac{\partial p}{\partial r}$
Turbulent kinetic energy	k	$\frac{\mu_{\text{eff}}}{\sigma_k}$	$G_k - \rho \epsilon$
Turbulent dissipation rate	ϵ	$\frac{\mu_{\text{eff}}}{\sigma_\epsilon}$	$\frac{\epsilon}{k} (C_1 G_k - C_2 \rho \epsilon)$

$$G_k = \mu_{\text{eff}} \left\{ 2 \left[\left(\frac{\partial \bar{u}}{\partial x} \right)^2 + \left(\frac{\partial \bar{v}}{\partial r} \right)^2 + \frac{\bar{v}^2}{r^2} \right] + \left(\frac{\partial \bar{u}}{\partial r} + \frac{\partial \bar{v}}{\partial x} \right)^2 \right\}$$

The values for the five constants recommended by Launder and Spalding [31] are tabulated in Table 12.

Table 12. $k \sim \epsilon$ turbulence model constants from Ref. [31].

<u>Constant</u>	<u>Value</u>
C_D	0.09
C_1	1.43
C_2	1.92
σ_K	1.00
σ_ϵ	1.30

The dependent variables at the wall are linked to those at the first grid node from the wall by equations representing a "modified log-law" expression. Thus, the velocity parallel to the wall and at a distance y_1 from it is assumed to be represented by

$$\bar{u} C_D^{1/4} k^{1/2} / (\tau_w / \rho) = \frac{1}{\kappa} \ln(EC_D^{1/4} k^{1/2} y_1 \rho / \mu_{lam}) \quad (26)$$

where κ is a constant equal to 0.4, E is a constant equal to 9 for smooth walls, and τ_w is the wall shear stress obtained in solving the momentum equations. The calculations of the turbulent kinetic energy, k , and the rate of dissipation, ϵ , at the first grid node are determined in a manner consistent with Equation (26).

The 2/E/FIX code was modified for the single step problem by incorporating the solid wall boundary condition, Equation (26) at the

upper wall in place of the axis of symmetry condition. In addition the option to accept tabular (experimental) data as initial conditions was added; the array sizes were increased to accept a 41 x 41 grid; and a restart capability was added. This latter modification also allowed the relaxation parameter to become variable; that is, its value could be changed after a prescribed number of iterations providing an increased rate of convergence and a decreased execution time.

The program was run on Purdue's CDC 6600 computer for three grid sizes, namely 11 x 11, 21 x 21, and 41 x 41. The 21 x 21 grid was used for the comparison calculations and is the same as the experimental grid with the exception that in the streamwise direction it is twice as fine and one step height longer. The solution was subject to a 10^{-3} convergence criterion and relaxation parameter values of 0.3 - 0.6 were used. The stream function, ψ , and the reattachment length, x_r , were calculated from the numerical results in the same manner as the experimental results.

The storage requirements for the 11 x 11, 21 x 21, and 41 x 41 grids were 20k, 37k, and 70k words, respectively, and the corresponding calculation times were approximately 50, 200, and 5000 seconds.

2. Matching Reattachment Length

In order to compare the numerical solution to the experimental results, the reattachment length was chosen as the common flow field characteristic. Moon and Rudinger [20] "matched" their numerical solution with their experimental results in terms of reattachment length with the values of $C_1 = 1.43$ and $C_2 = 1.70$. The recirculation

zone thickness and mean streamwise centerline velocity decay in their axisymmetric annular step were, however, incorrectly predicted.

The turbulent dissipation rate coefficient, C_2 , was varied in the present work over a wide range. A 21 x 21 grid was used and the reattachment location was determined for each value of C_2 . As shown in Figure 38, the reattachment length (non-dimensionalized with the step height, h) was significantly altered. A least squares fit [38] was applied to the data resulting in the following functional relationship

$$C_2 = -0.0548 \left(\frac{x_r}{h} \right) + 2.2648 . \quad (27)$$

The experimentally measured reattachment length was 6.94 step heights and proper substitution into Equation (27) yields $C_2 = 1.88$ which was used for the numerical calculations and comparisons. The remaining turbulence constants were not changed and appear in Table 12.

3. Mean Velocities

a. Numerical Results and Comparisons

Figure 39 shows the calculated non-dimensionalized mean streamwise velocity profiles at the inlet and four representative locations downstream of the step. Figures 40 and 41 present the calculated non-dimensionalized stream function contours and the calculated velocity vector plot, respectively. Again, the reader should note the difference in the horizontal and vertical scales.

A representative comparison of three calculated mean streamwise velocity profiles with experimental profiles is shown in Figures 42, 43,

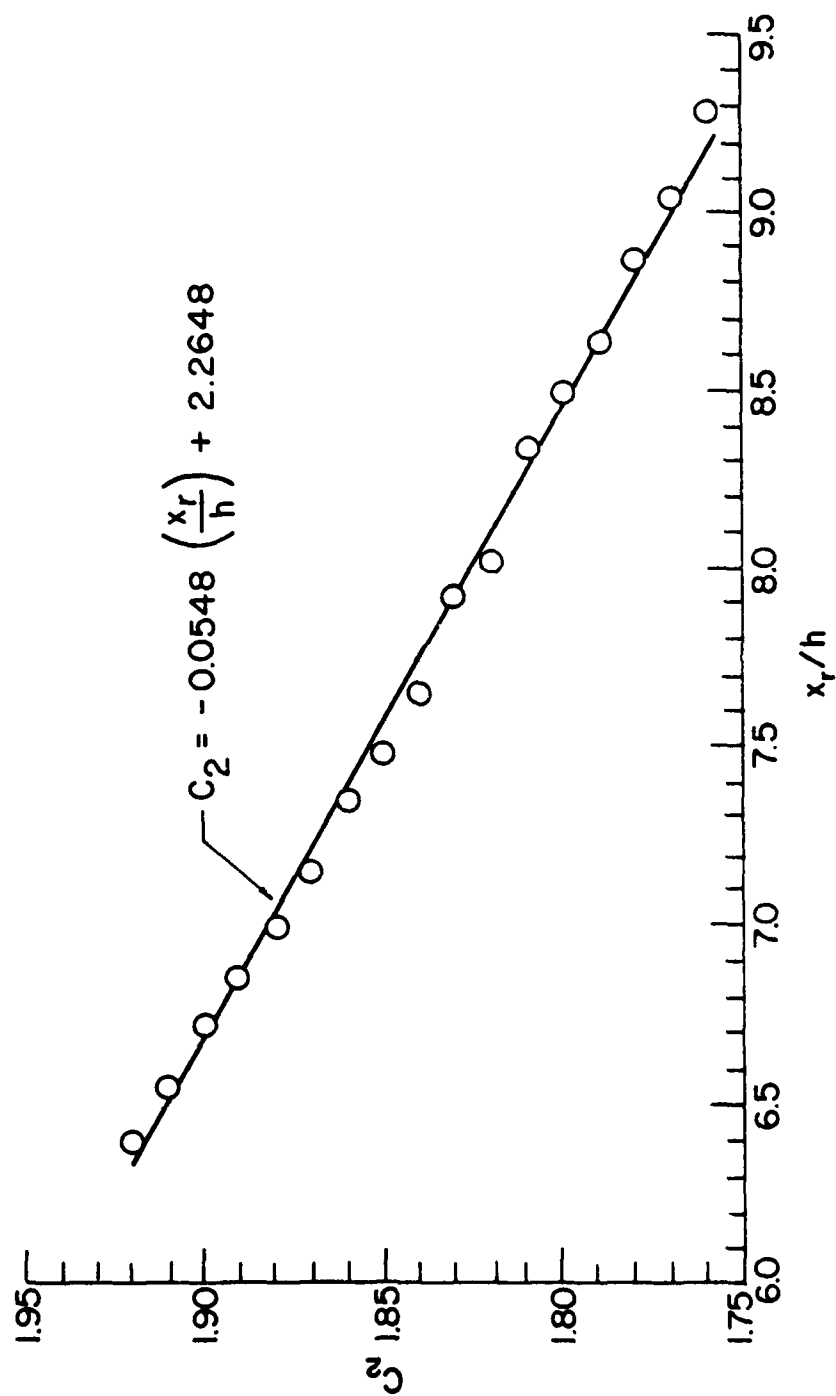


Figure 38. Turbulent dissipation rate coefficient, C_2 , vs. reattachment length.

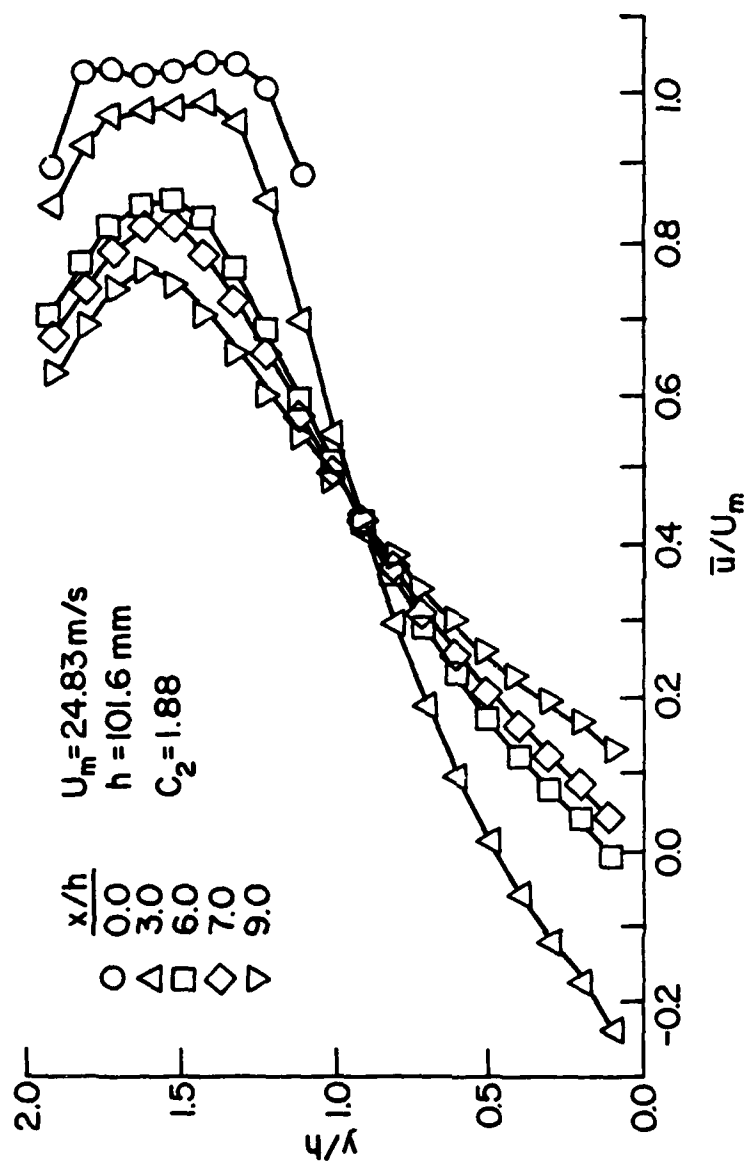


Figure 39. Calculated streamwise velocity profiles.

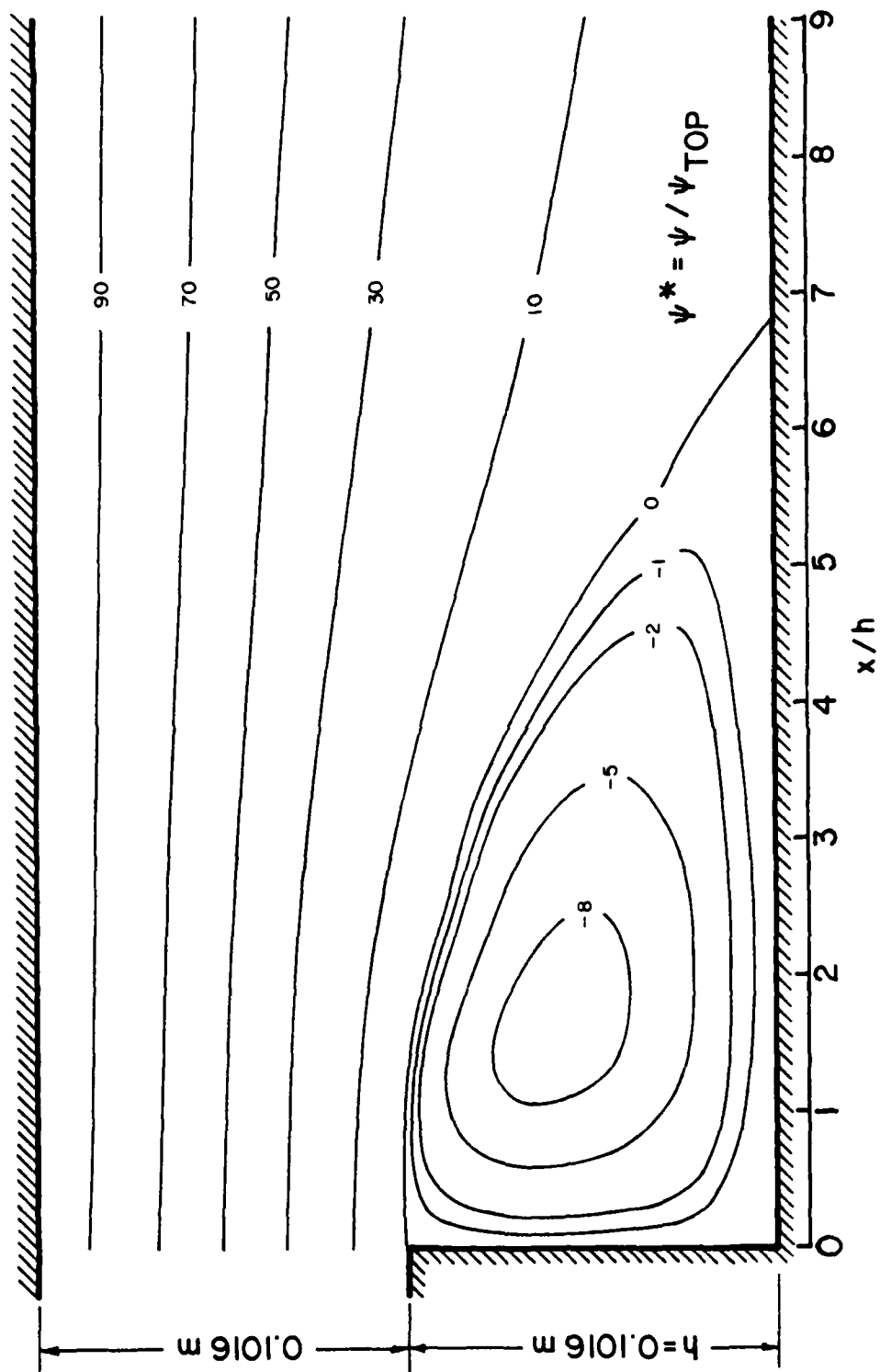


Figure 40. Calculated stream function contours.

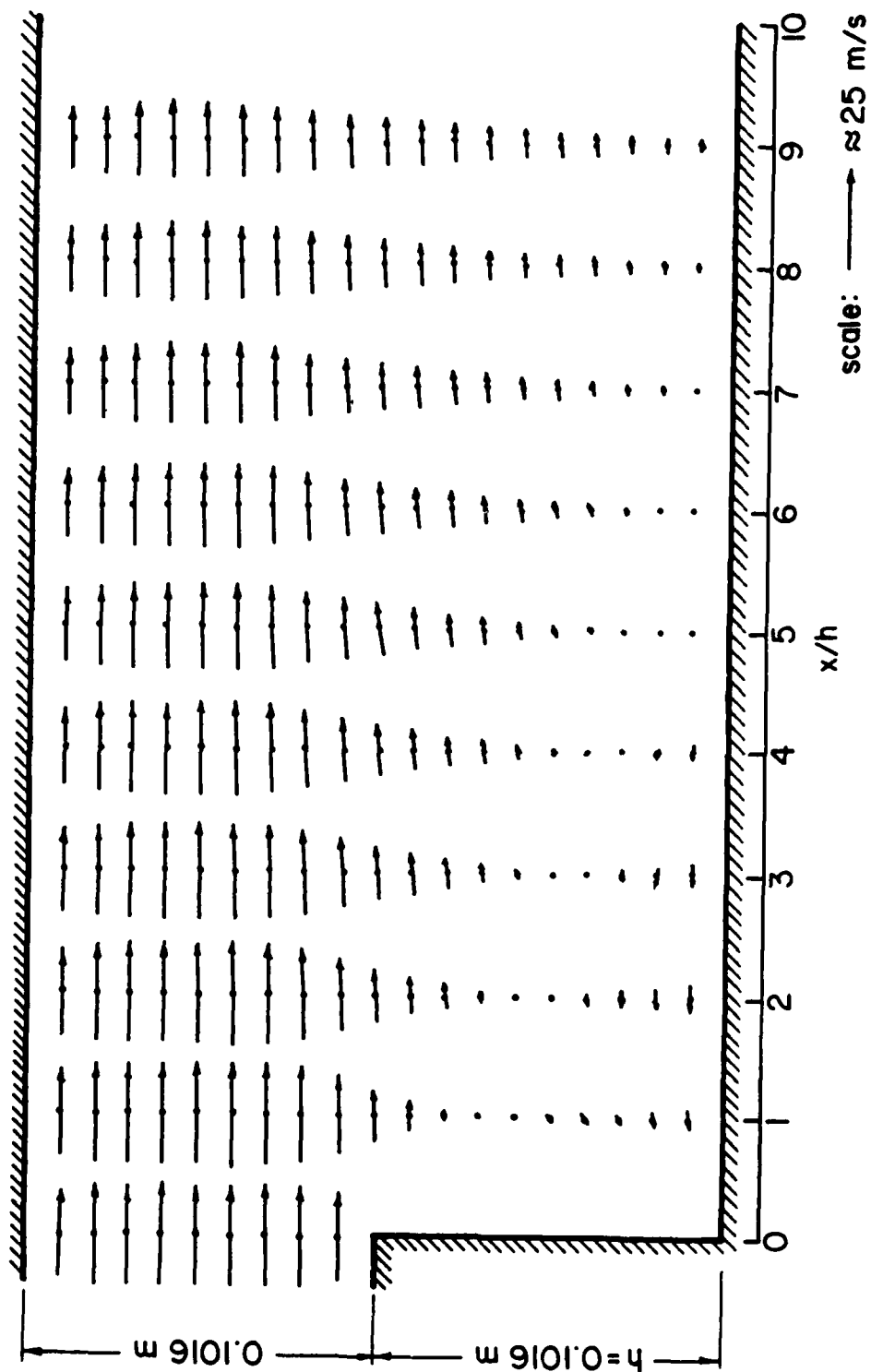


Figure 41. Calculated velocity vector plot.

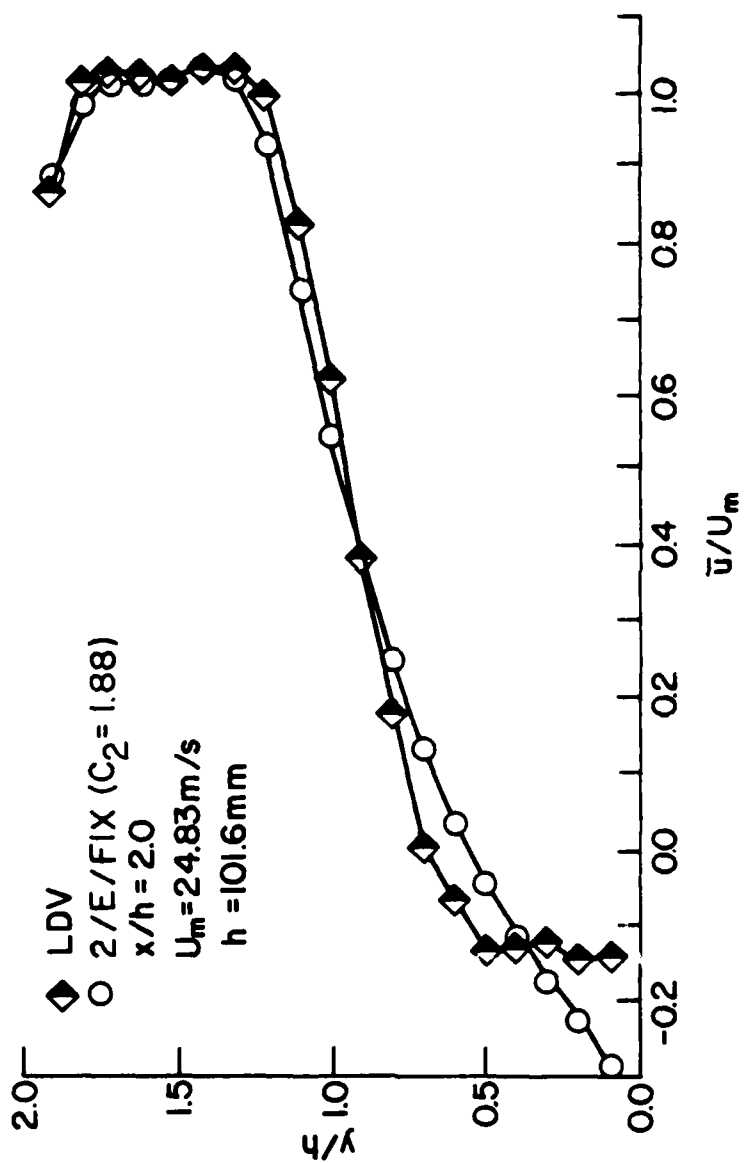


Figure 42. Comparison of calculated and measured streamwise velocity profiles at $x/h = 2$.

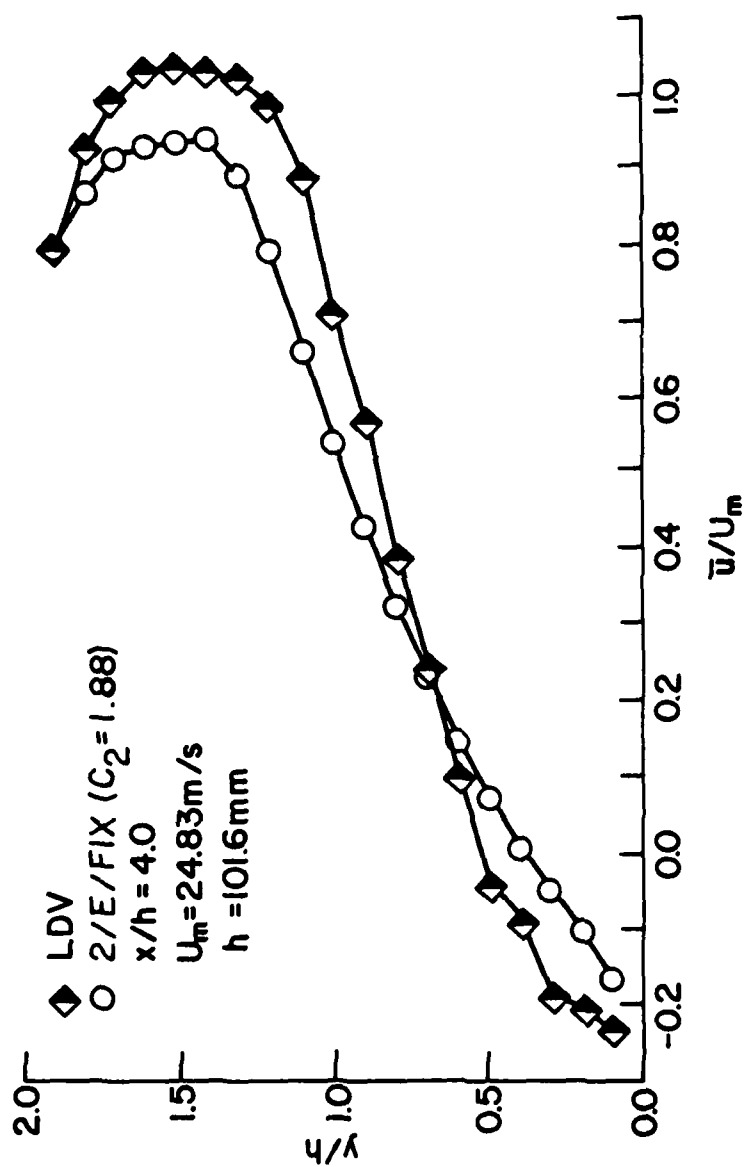


Figure 43. Comparison of calculated and measured streamwise velocity profiles at $x/h = 4$.

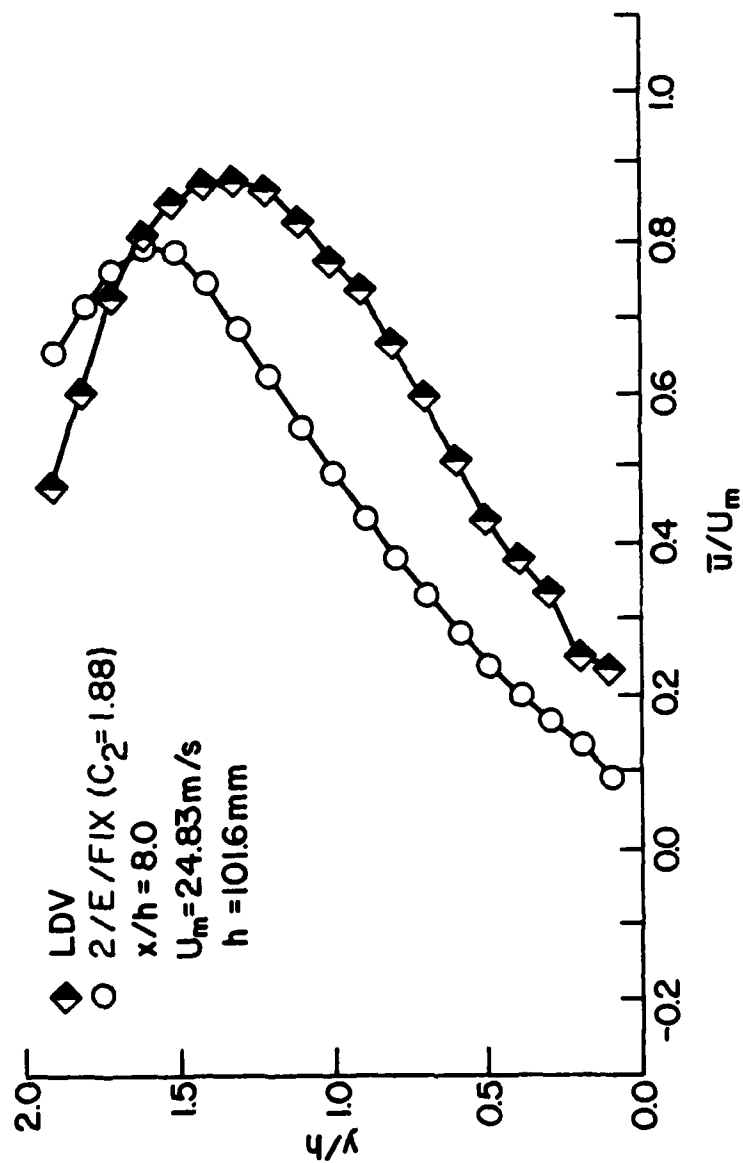


Figure 44. Comparison of calculated and measured streamwise velocity profiles at $x/h = 8$.

and 44. The three-dimensional flow influence does not appear in the calculated results. This influence is apparent in the reverse flow region shown in Figure 42 and in the profiles shown in Figures 43 and 44.

b. Grid Dependence

The numerical solution should be invariant with respect to an increase in the number of grid nodes before it can be considered a valid solution. In order to check the validity (grid dependence) of the 21 x 21 solution a coarser and finer grid were selected; 11 x 11 and 41 x 41, respectively. If the results of the three grid sizes are in good agreement, or at least the latter two, then the results of the 21 x 21 grid can be considered valid. All grid dependence tests were run prior to the reattachment length investigation ($1.70 \leq C_2 \leq 1.92$) and hence a value of $C_2 = 1.92$ was used. Though the numerical solution that was compared with the experimental results was for $C_2 = 1.88$ it is felt that no significant differences in the grid dependence results exist with $C_2 = 1.92$. Computer execution time (money) for the 41 x 41 grid made running more grid dependence tests prohibitive.

Figures 45, 46, and 47 are a comparison of the numerical solution for the mean streamwise velocity profiles for the three grid spacings at x/h of 1, 5, and 10 respectively. At $x/h = 5$ (Figure 46) the finer grid shows a larger boundary layer growth which can also be seen at $x/h = 10$ (Figure 47). The wall function employed appears to be dependent on the location of the first grid node normal to the wall. The overall agreement is very good.

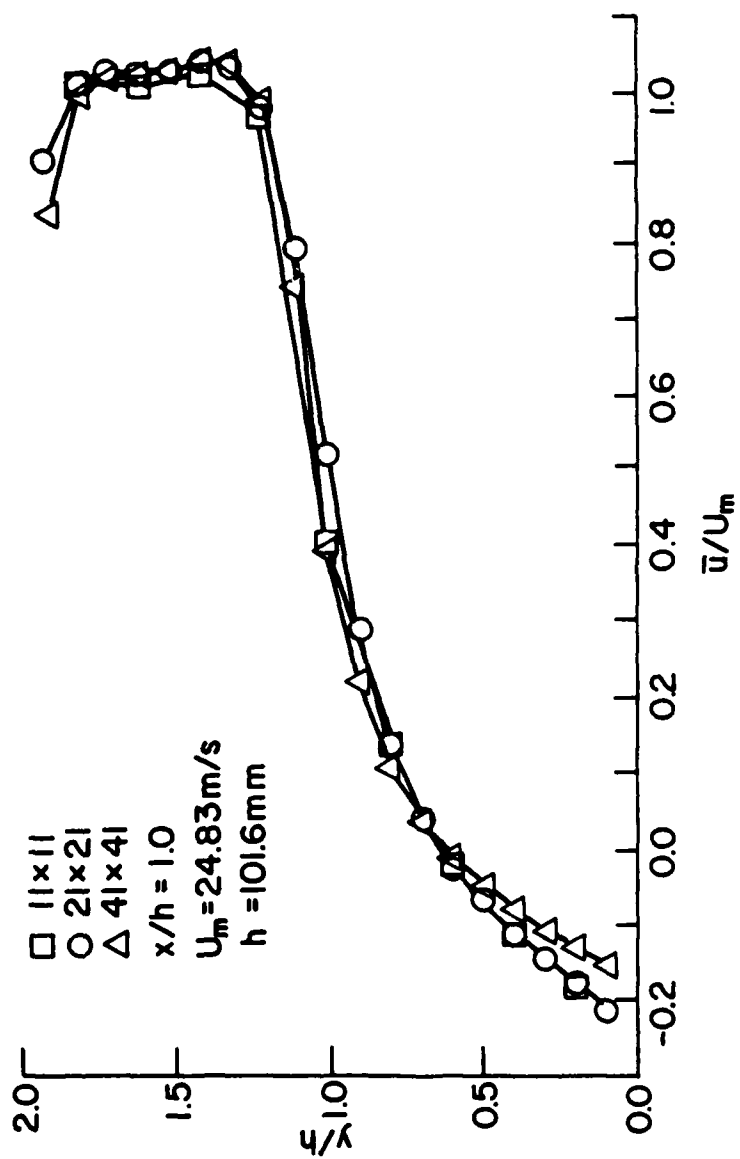


Figure 45. Grid dependence for calculated streamwise velocity profiles at $x/h = 1.0$.

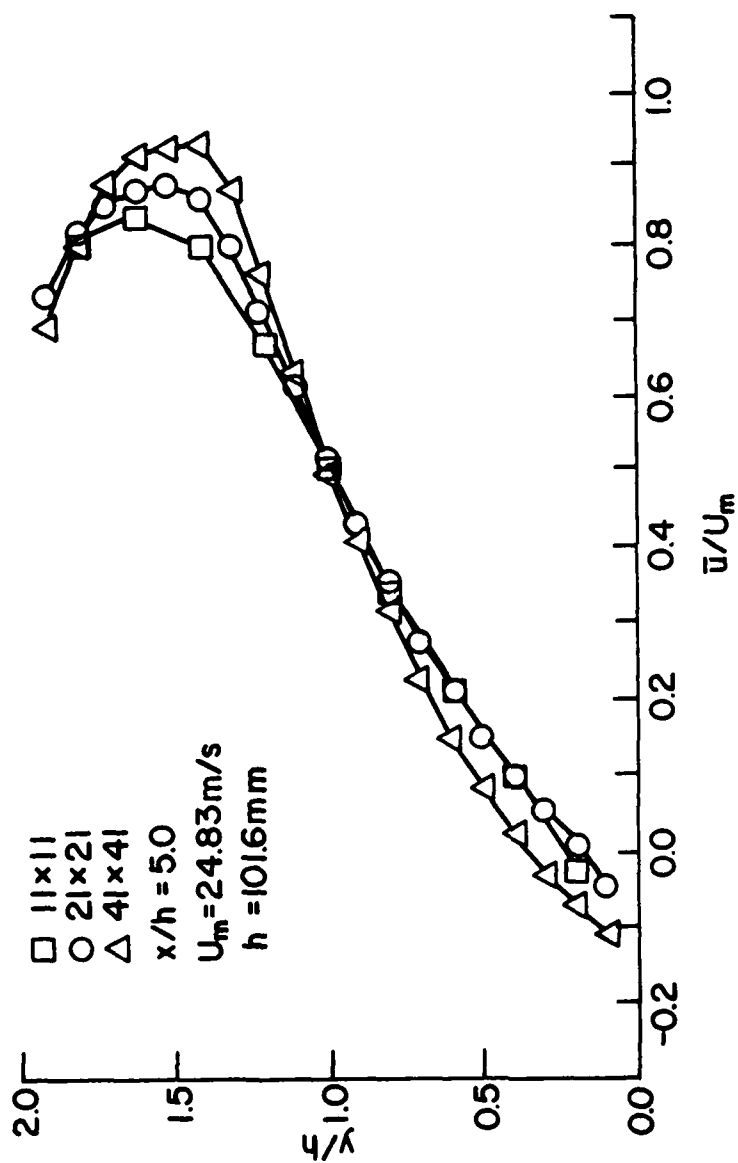


Figure 46. Grid dependence for calculated streamwise velocity profiles at $x/h = 5.0$.

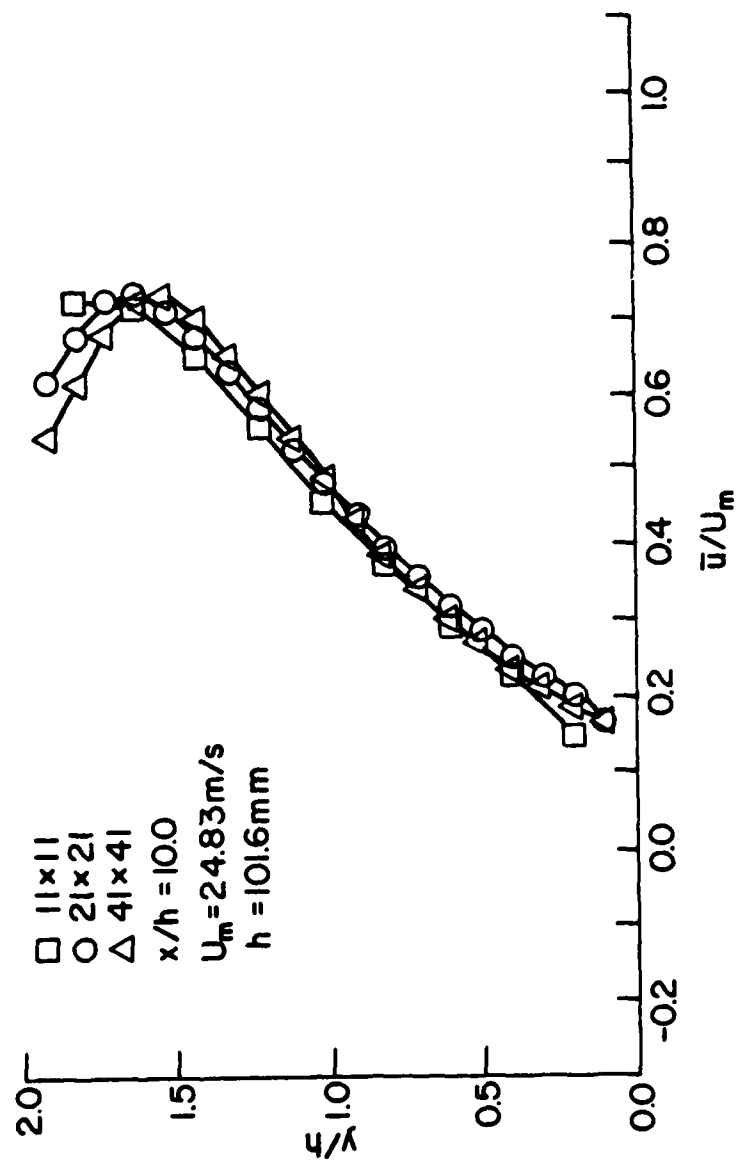


Figure 47. Grid dependence for calculated streamwise velocity profiles at $x/h = 10.0$.

The validity of the transverse mean velocity solution, \bar{v} , was found to be good to the same degree as the mean streamwise velocity solution.

4. Turbulence Parameters

a. Numerical Results and Comparisons

The comparison of turbulence parameters is limited to the turbulent kinetic energy, $\frac{1}{2}(\overline{u'^2} + \overline{v'^2})$. The streamwise and transverse turbulence intensities as well as the Reynolds stress are not calculated by the program.

Figure 48 presents the calculated turbulent kinetic energy profiles at the inlet and four representative stations downstream of the step. Figure 49 shows the contours of constant turbulent kinetic energy. A representative comparison of three calculated profiles with experimental profiles is shown in Figures 50, 51, and 52.

The comparison of the calculated with measured profiles shows an over prediction by the 2/E/FIX code with a generally fair qualitative comparison.

b. Grid Dependence

Results of the kinetic energy grid dependence tests are shown in Figures 53, 54, 55. The discrepancies shown in Figure 53 indicate that a finer grid is needed near the step face to accurately compute the turbulent kinetic energy. The validity of the 21 x 21 profile at $x/h = 1$ (Figure 53) is very questionable. Figures 54 and 55 show that downstream the grid size influences the magnitude of the turbulent

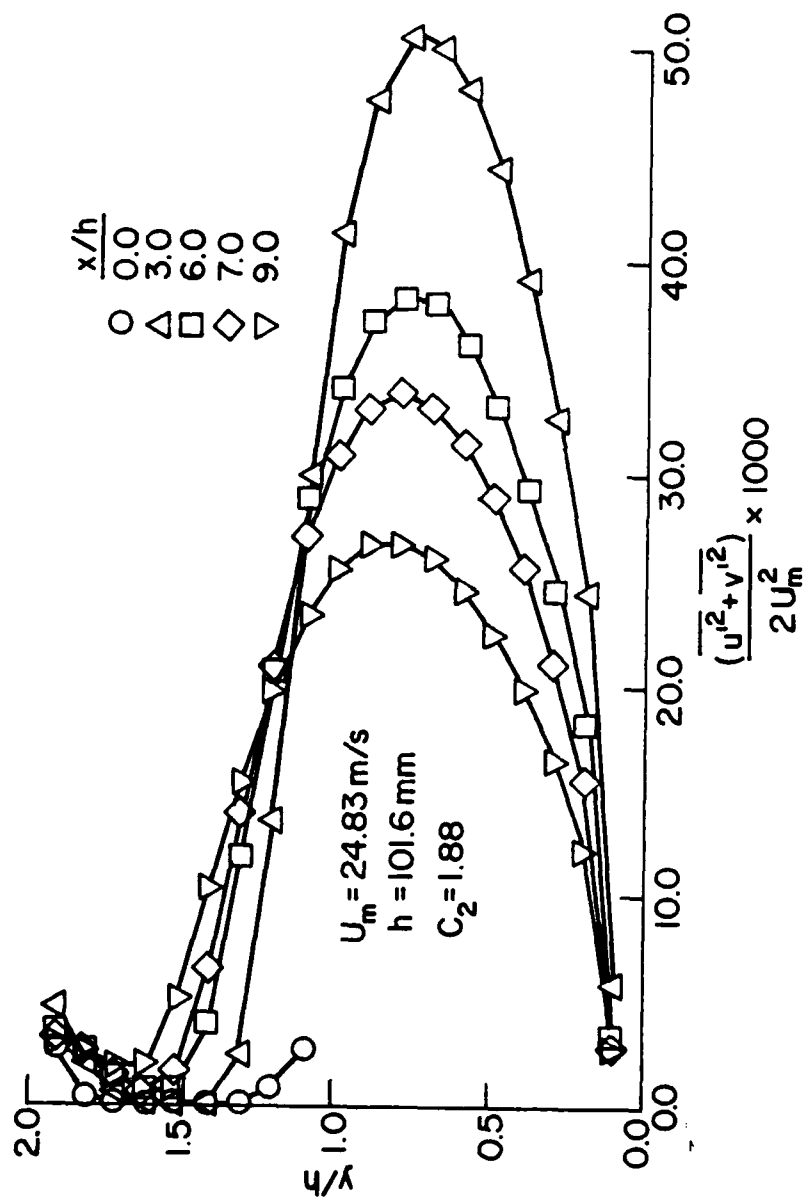


Figure 48. Calculated turbulent kinetic energy profiles.

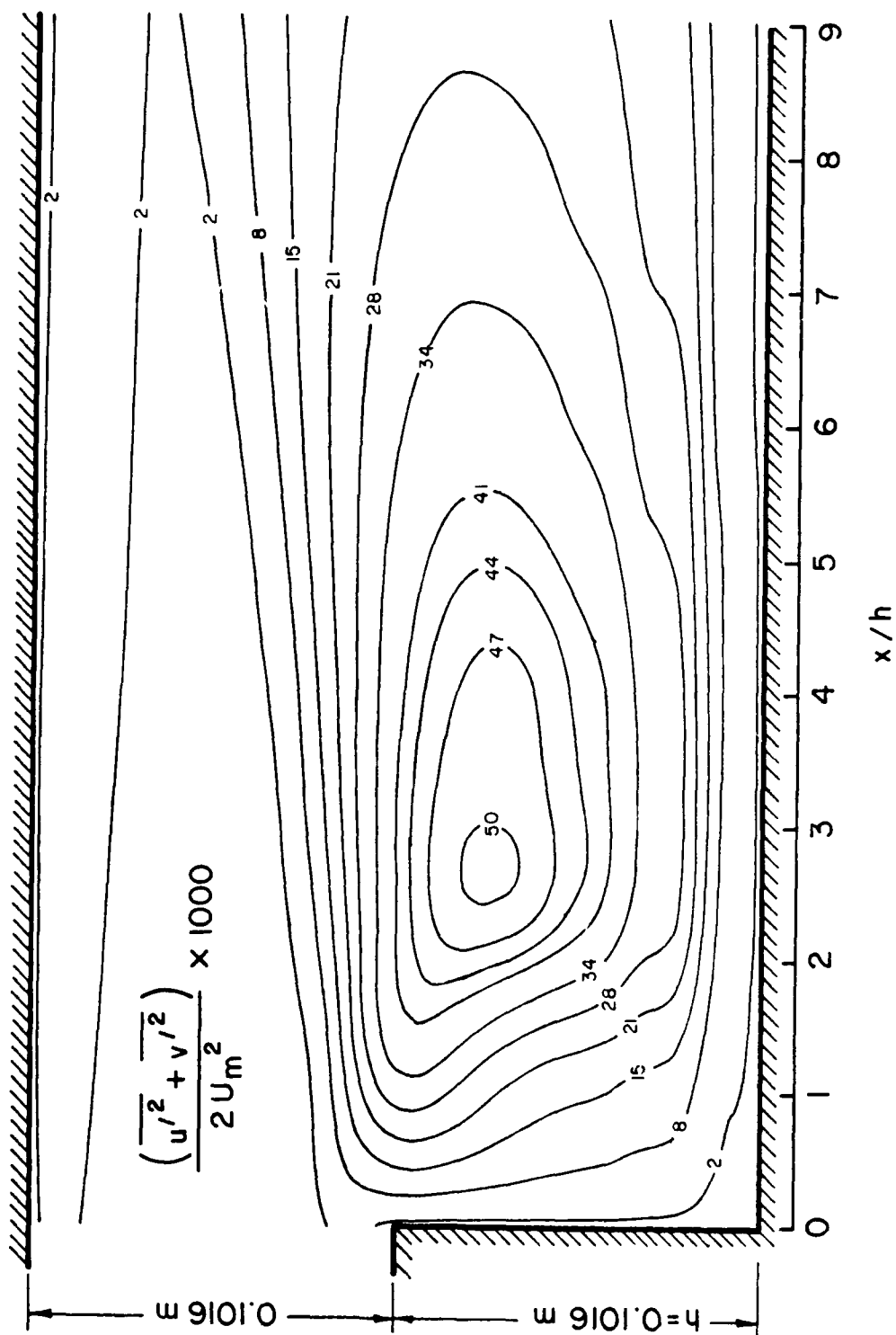


Figure 49. Calculated turbulent kinetic energy contours.

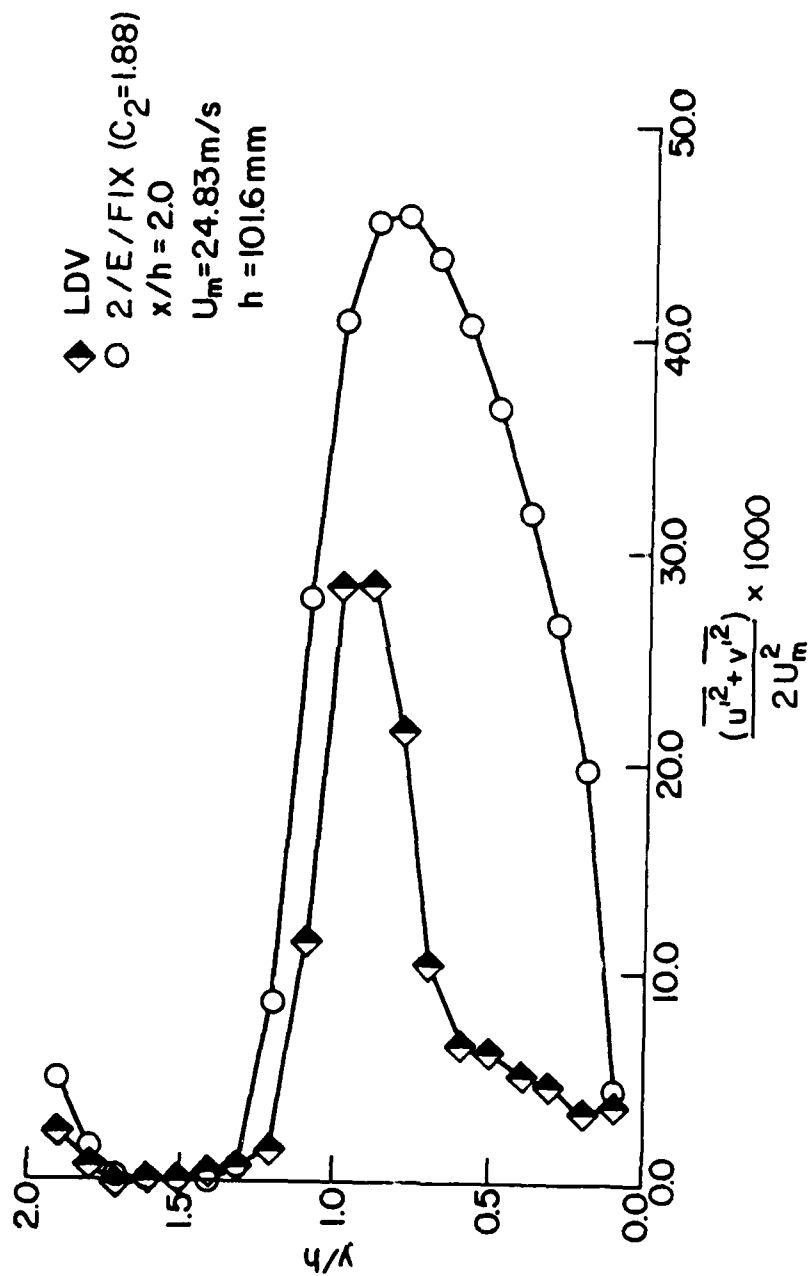


Figure 50. Comparison of calculated and measured turbulent kinetic energy profiles at $x/h = 2.0$.

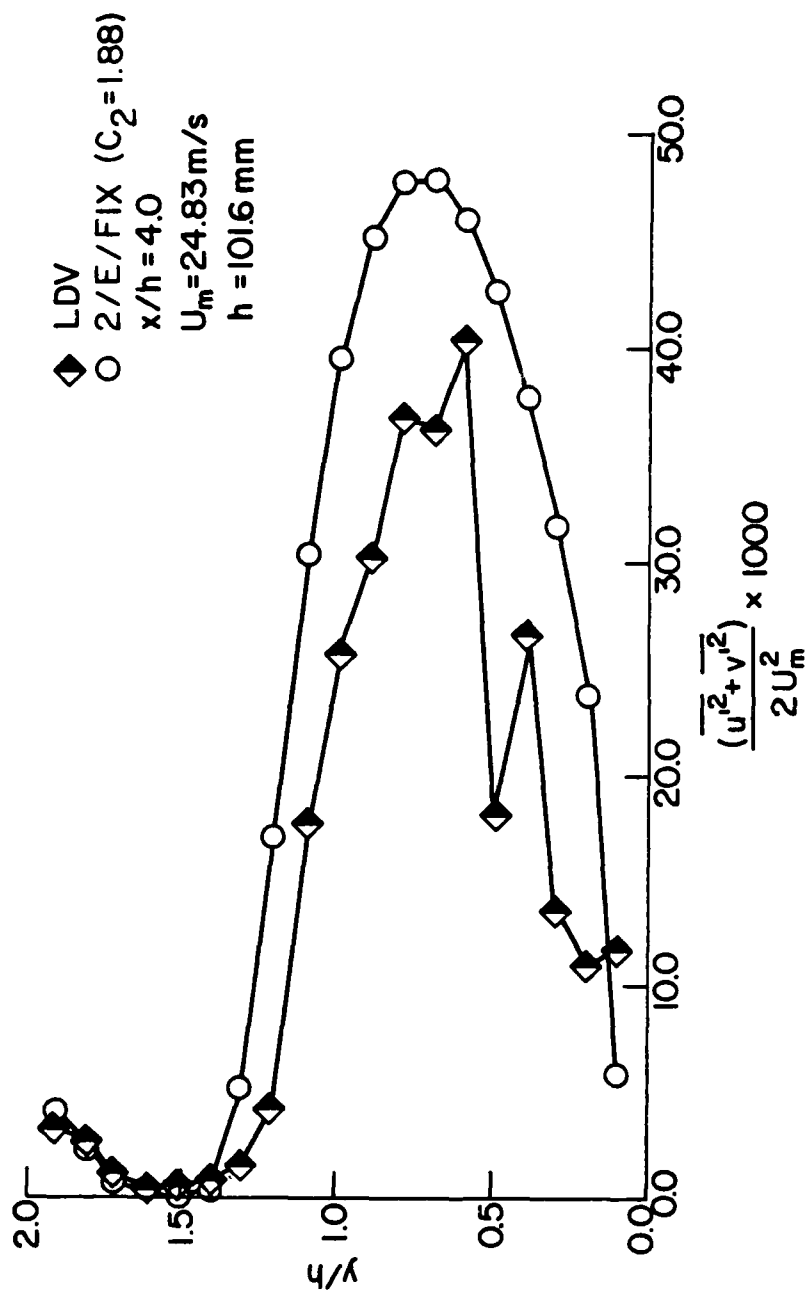


Figure 51. Comparison of calculated and measured turbulent kinetic energy profiles at $x/h = 4.0$.

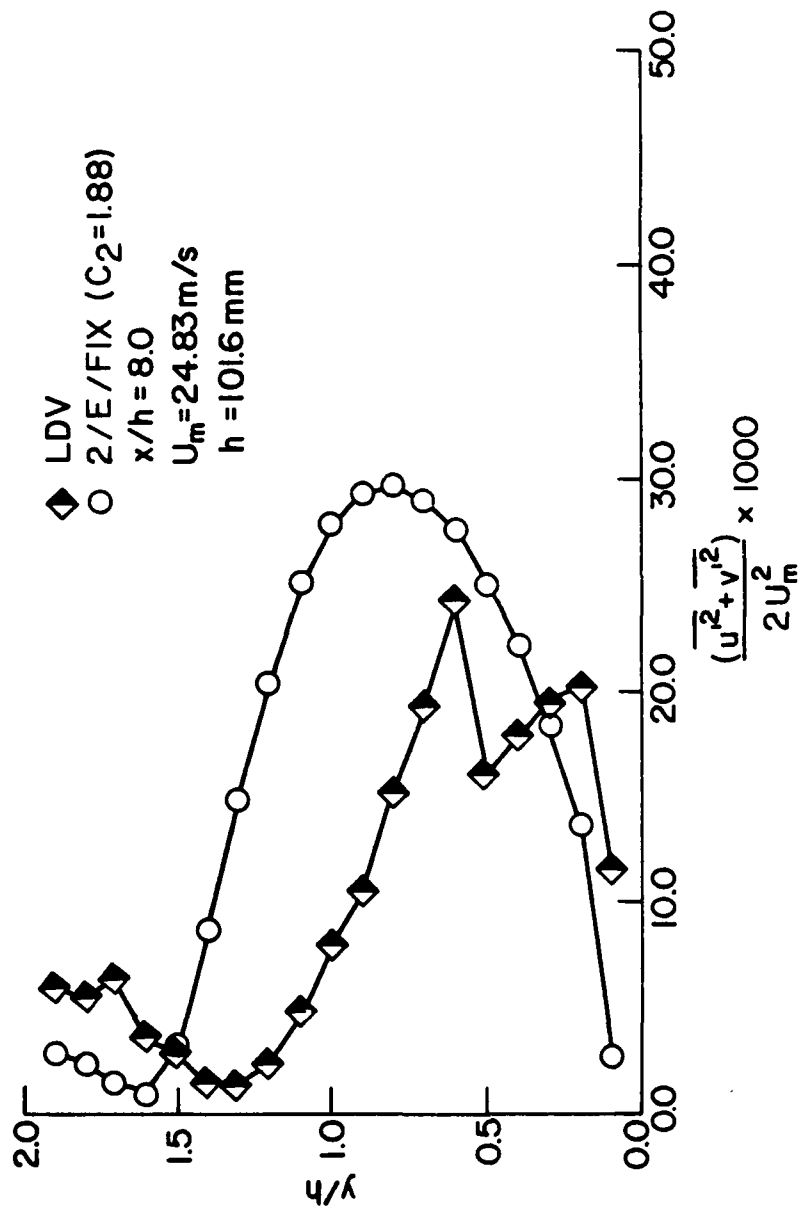


Figure 52. Comparison of calculated and measured turbulent kinetic energy profiles at $x/h = 8.0$.

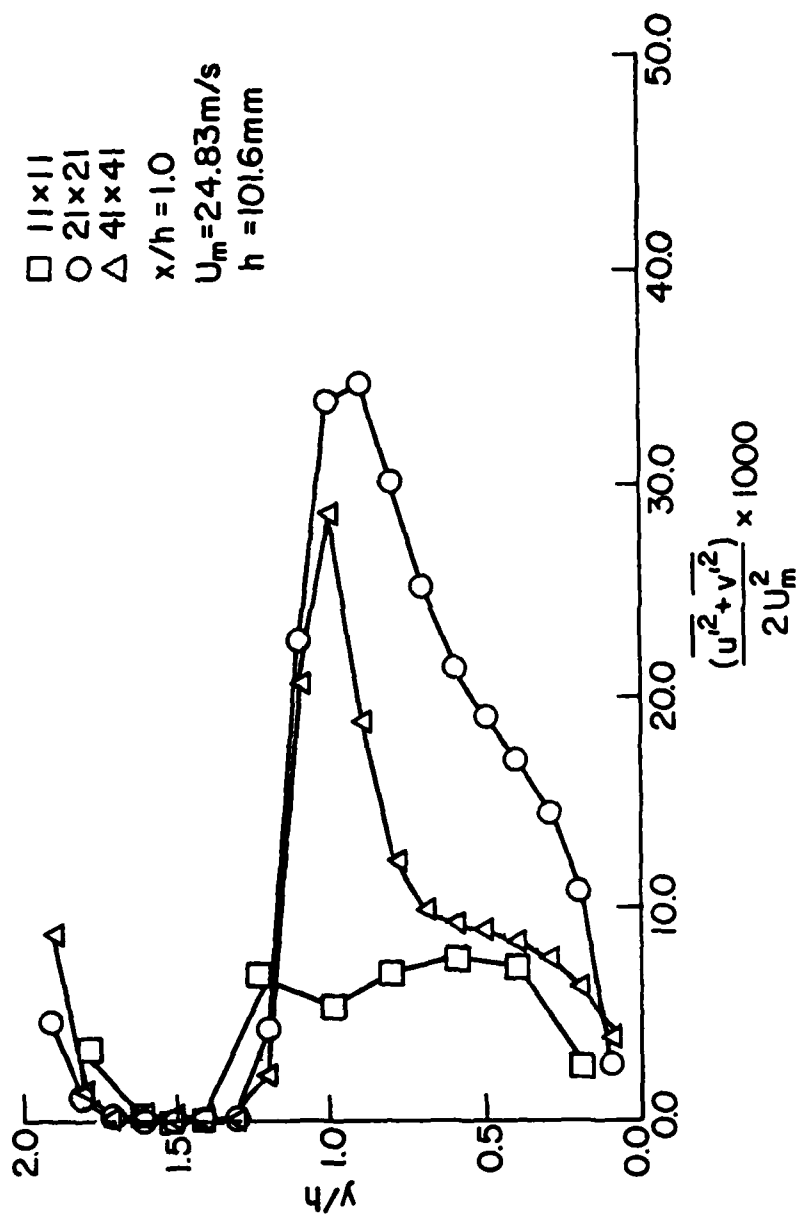


Figure 53. Grid dependence for calculated turbulent kinetic energy profiles at $x/h = 1.0$.

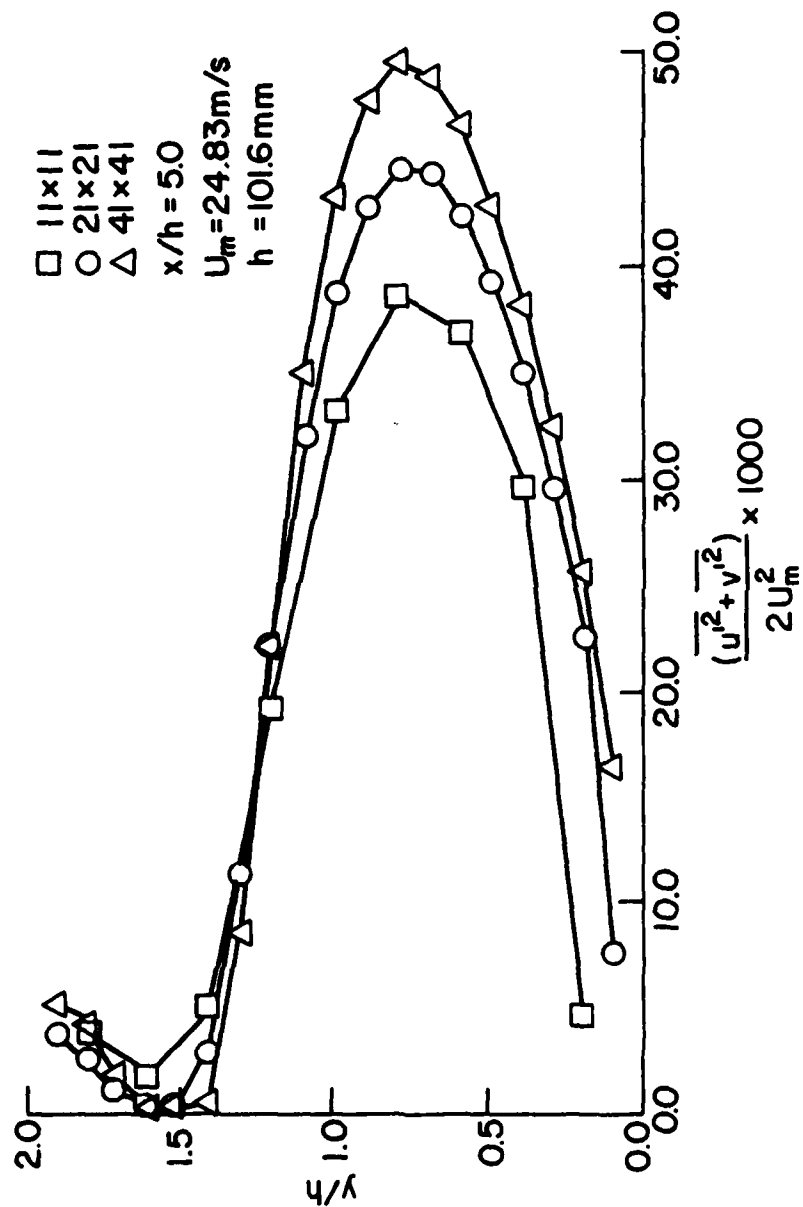


Figure 54. Grid dependence for calculated turbulent kinetic energy profiles at $x/h = 5.0$.

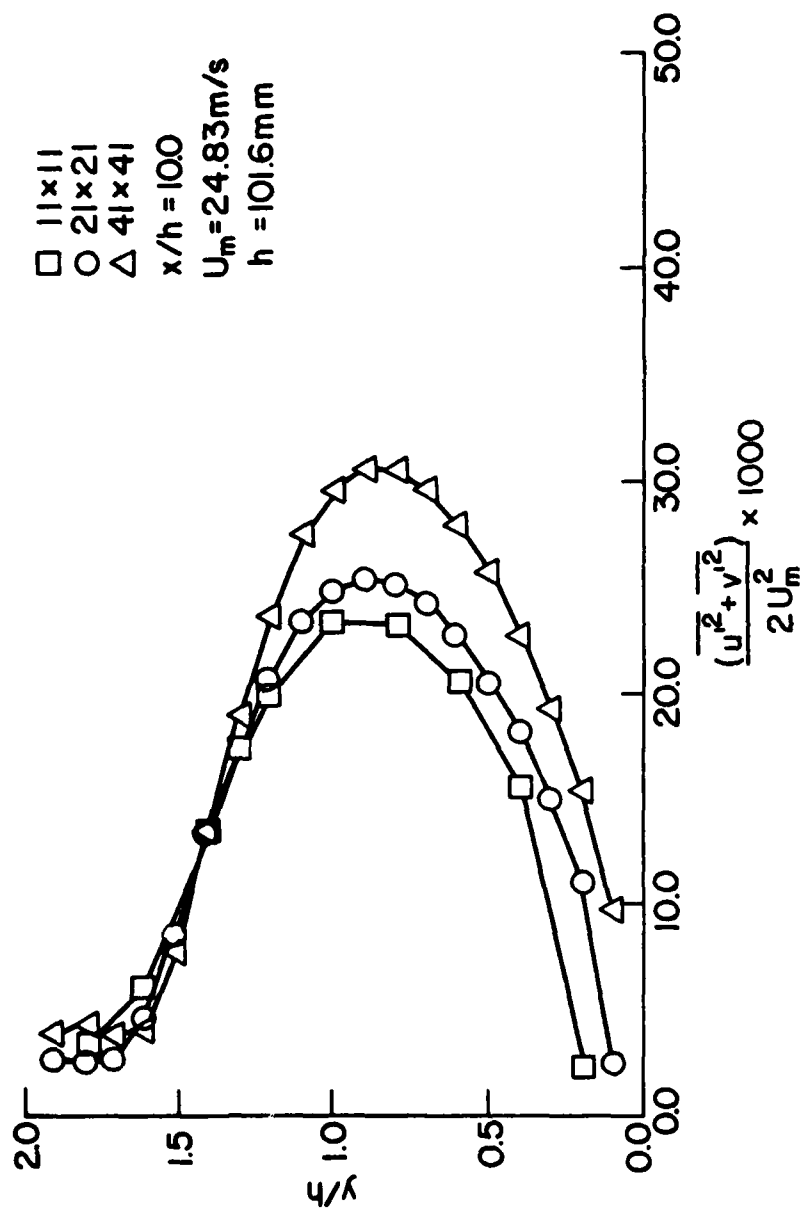


Figure 55. Grid dependence for calculated turbulent kinetic energy profiles at $x/h = 10.0$.

kinetic energy but not the qualitative profile. In general, the turbulent kinetic energy solution is qualitatively valid, but not to the same degree as the momentum results (\bar{u} and \bar{v}). In general, a finer grid is needed to accurately calculate turbulence quantities.

SECTION VII

CONCLUSIONS AND RECOMMENDATIONS

Several conclusions are drawn from the results of this investigation.

First, it is apparent that although the geometry is two-dimensional the flow field is three-dimensional.

Second, although the approach flow is "steady", manometer observations indicate some unsteadiness in the downstream flow field, particularly in the recirculation region.

Third, the mean velocities and turbulence parameters that are determined by correlating the results of two or three angular measurements have an inherent large uncertainty associated with them. This is due to the differencing of quantities that are nearly equal in magnitude.

Fourth, the nonintrusive character and directional capability of the laser Doppler velocimeter make it a unique instrument for making mean velocity and turbulence measurements in recirculating flows. The extension to accurate simultaneous two component measurements, to three component measurements (not simultaneous) and to combusting flow measurements is completely feasible; and, in fact, has been demonstrated to some degree by other researchers.

Fifth, the two-dimensional $k \sim \epsilon$ model provides a computationally good prediction of the mean streamwise velocity, \bar{u} , in the flow field. The model provides qualitative turbulence parameter information, even

though the computed values tend to be too high.

As in most investigations of this sort there remains a number of unanswered questions. It is felt that further work in the following areas could prove fruitful:

1. A more detailed investigation of the flow unsteadiness.
2. A three-dimensional mapping of the entire flow field. The measurements should be extended downstream to the fully developed region, and should include an investigation of both flow asymmetry and spanwise flows. Some form of flow visualization may be very useful here.
3. Experimental measurements in an axisymmetric geometry.
4. Modification of the numerical code to include three-dimensional flows.
5. Modification of the $k \sim \epsilon$ model to better represent the recirculating flow region.

REFERENCES

- [1] Bowyer Jr., J.M., and Carter, W.V., "Separated Flow Behind a Rearward-Facing Step with and without Combustion," AIAA Journal, Vol. 3, No. 1, pp. 181-183, January, 1965.
- [2] Burggraf, O.R., "Computational Study of Supersonic Flow over Backward-Facing Steps at High Reynolds Number," ARL-70-0275, Aerospace Research Laboratories, Wright-Patterson Air Force Base, Ohio, November, 1970.
- [3] Sfeir, A., "Supersonic Flow Separation on a Backward Facing Step," University of California, Berkeley, Report No. AS-66-18, December, 1966.
- [4] Chapman, D.R., Kuehn, D.M., and Larson, H.K., "Investigation of Separated Flows in Supersonic and Subsonic Streams with Emphasis on the Effect of Transition," NACA TN-3869, 1957.
- [5] Owen, P.R., and Kanfer, L., "On the Laminar Boundary Layer Separation From the Leading Edge of a Thin Aerofoil," Royal Aircraft Establishment Report No. Aero. 2508, October, 1953.
- [6] Crabtree, L.F., "Effects of Leading-Edge Separation on Thin Wings in Two-Dimensional Incompressible Flow," Journal of the Aeronautical Sciences, Vol. 24, No. 8, pp. 597-604, August, 1957.
- [7] Schubauer, G.B., and Klebanoff, P.S., "Contributions to the Mechanics of Boundary Layer Transition," NACA TN-3489, 1955.
- [8] Moore, T.W.F., "Some Experiments on the Reattachment of a Laminar Boundary Layer Separating From a Rearward Facing Step on a Flat Plate Aerofoil," Journal of the Royal Aeronautical Society, Vol. 64, pp. 668-672, November, 1960.
- [9] Roshko, A., and Lau, J.C., "Some Observations on Transition and Reattachment of a Free Shear Layer in Incompressible Flow," Proceedings of the 1965 Heat Transfer and Fluid Mechanics Institute, edited by A.F. Charwat, Stanford University Press, Stanford, pp. 157-167.

- [10] Goldstein, R.J., Erickson, V.L., Olson, R.M., and Eckert, E.R.G., "Laminary Separation, Reattachment, and Transition of the Flow Over a Downstream-Facing Step," Journal of Basic Engineering, Vol. 92, pp. 732-741, December, 1970.
- [11] Abbott, D.E., and Kline, S.J., "Experimental Investigation of Subsonic Flow Over Single and Double Backward Facing Steps," Journal of Basic Engineering, Vol. 84, pp. 317-325, September, 1962.
- [12] Durst, F., Melling, A., and Whitelaw, J.H., "Low Reynolds Number Flow Over a Plane Symmetric Sudden Expansion," Journal of Fluid Mechanics, Vol. 64, pt. 1, pp. 111-128, 3 June, 1974.
- [13] Macagno, E.O., and Hung, T.K., "Computational and Experimental Study of a Captive Annular Eddy," Journal of Fluid Mechanics, Vol. 28, pt. 1, pp. 43-64, 12 April, 1967.
- [14] Zemanick, P.P., and Dougall, R.S., "Local Heat Transfer Downstream of an Abrupt Circular Channel Expansion," ASME Journal of Heat Transfer, Vol. 92, pp. 53-60, February, 1970.
- [15] Back, L.H., and Roschke, E.J., "Shear-Layer Flow Regimes and Wave Instabilities and Reattachment Lengths Downstream of an Abrupt Circular Channel Expansion," ASME Journal of Applied Mechanics, Vol. 94E, pp. 677-681, September, 1972.
- [16] Cramer, K.R., "On Laminar Separation Bubbles," Journal of the Aeronautical Sciences, Vol. 25, No. 2, pp. 143-144, February, 1958.
- [17] Eaton, J.K., Johnston, J.P., and Jeans, A.H., "Measurements in a Reattachment Turbulent Shear Layer," 2nd Symposium on Turbulent Shear Flows, Imperial College, London, 2-4 July, 1979.
- [18] Seban, R.A., Emery, A., and Levy, A., "Heat Transfer to Separated and Reattached Subsonic Turbulent Flows Obtained Downstream of a Surface Step," Journal of the Aero/Space Sciences, Vol. 26, No. 12, pp. 809-814, December, 1959.
- [19] Tani, I., Iuchi, M., and Komoda, H., "Experimental Investigation of Flow Separation Associated with a Step or a Groove," Aeronautical Research Institute, University of Tokyo, Report No. 364, pp. 119-137.
- [20] Moon, L.F., and Rudinger, G., "Velocity Distribution in an Abruptly Expanding Circular Duct," ASME Journal of Fluids Engineering, Vol. 99, pp. 226-230, March 1977.

- [21] Durst, F., Melling, A., and Whitelaw, J.H., "Optical Anemometer Measurements in Recirculating Flows and Flames," In: Proceedings DISA Conference, Vol. 1, paper II, Leicester University Press, 1972.
- [22] Cherdron, W., Durst, F., and Whitelaw, J.H., "Asymmetric Flows and Instabilities in Symmetric Ducts with Sudden Expansions," Journal of Fluid Mechanics, Vol. 84, pt. 1, pp. 13-31, 16 January, 1978.
- [23] Winant, C.D., and Browand, F.K., "Vortex Pairing: The Mechanism of Turbulent Mixing Layer Growth at a Moderate Reynolds Number," Journal of Fluid Mechanics, Vol. 63, pt. 2, pp. 237-255, 3 April, 1974.
- [24] Rothe, P.F. and Johnston, J.P., "Free Shear Layer Behavior in Rotating Systems," ASME Journal of Fluids Engineering, Vol. 101, pp. 117-120, March, 1979.
- [25] Davies, T.W., and Snell, D.J., "Turbulent Flow Over a Two-Dimensional Step and Its Dependence Upon Upstream Flow Conditions," Turbulent Shear Flows I, Springer-Verlag, New York, pp. 13.29-13.33, 1977.
- [26] Etheridge, D.W., and Kemp, P.H., "Measurements of Turbulent Flow Downstream of a Rearward-Facing Step," Journal of Fluid Mechanics, Vol. 86, pt. 3, pp. 545-566, 14 June, 1978.
- [27] Smyth, R., "Turbulent Flow Over a Plane Symmetric Sudden Expansion," ASME Journal of Fluids Engineering, Vol. 101, pp. 348-353, September, 1979.
- [28] Moss, W.D., Baker, S., and Bradbury, L.J.S., "Measurements of Mean Velocity and Reynolds Stresses in Some Regions of Recirculating Flow," Turbulent Shear Flows I, Springer-Verlag, New York, pp. 13.1-12.7, 1977.
- [29] Teyssandier, R.G., and Wilson, M.P., "An Analysis of Flow Through Sudden Enlargements in Pipes," Journal of Fluid Mechanics, Vol. 64, pt. 1, pp. 85-95, 3 June, 1974.
- [30] Harlow, F.H., and Nakayama, P., "Transport of Turbulence Energy Decay Rate," Los Alamos Science Laboratory, University of California Report LA-3854, 1968.
- [31] Launder, B.E., and Spalding, D.B., "The Numerical Computation of Turbulent Flows," Computer Methods in Applied Mechanics and Engineering, Vol. 3, pp. 269-289, 1974.

- [32] Launder, B.E., Morse, A., Rodi, W., and Spalding, D.B., "The Prediction of Free Shear Flows - A Comparison of the Performance of Six Turbulence Models," In: Proceedings of NASA Conference on Free Shear Flows, Langley, 1972.
- [33] Gosman, A.D., Khalil, E.E., and Whitelaw, J.H., "The Calculation of Two-Dimensional Turbulent Recirculating Flows," Turbulent Shear Flows I, Springer-Verlag, New York, pp. 13.35-13.45, 1977.
- [34] McVey, R.E., "The Design of a Laser Doppler Velocimeter in Studying Turbulent and Mixing Flows," M.S. Thesis, Purdue University, May, 1979.
- [35] Instruction Manual for TSI Model 1980 Counter, Thermo-Systems Incorporated, St. Paul, Minnesota.
- [36] VanFrank, S., "MIDAS - User's and Programmers Manual," Thermal Sciences and Propulsion Center, Purdue University, 1980.
- [37] Stevenson, W.H., Thompson, H.D., Bremmer, R., and Roesler, T., "Laser Velocimeter Measurements in Turbulent and Mixing Flows - Part II, AFAPL-TR-2009, Part II, March, 1980.
- [38] Janus, M.L., Smith, G.M., and Wolford, J.C., "Applied Numerical Methods for Digital Computation with FORTRAN and CSMP," IEP-A Dun - Donnelly Publisher, New York, Second Edition, 1977.
- [39] Kline, S.J., and McClintock, F.A., "Describing Uncertainties in a Single Sample Experiment," Mechanical Engineering, Vol. 75, pp. 3-8, 1953.
- [40] Thompson, H.D., and Flack, R., Jr., "An Application of Laser Velocimetry to the Interpretation of Turbulent Structure," Proceedings of the ISL/AGARD Workshop on Laser Anemometry, German-French Research Institute, Pfeifer, H., and Haertig, J., editors, St.-Louis, France, 1976.
- [41] Yanta, W.J., "The Use of the Laser Doppler Velocimeter in Aerodynamic Facilities," AIAA Paper 80-0435, Presented at AIAA Aerodynamic Testing Conference, 18-20 March, 1980.
- [42] Pun, W.M., and Spalding, D.B., "A General Computer Program for Two-Dimensional Elliptic Flows," Imperial College Mechanical Engineering Department Report No. HTS/76/2.
- [43] Patankar, S.V., and Spalding, D.B., "A Calculation Procedure for Heat, Mass, and Momentum Transfer in Three-Dimensional Parabolic Flows," International Journal of Heat and Mass Transfer, Vol. 15, pp. 1787-1806, Pergamon Press, 1972.

- [44] Logan, S.E., "A Laser Velocimeter for Reynolds Stress and Other Turbulence Measurements," AIAA Journal, Vol. 10, No. 7, pp. 933-935, 1972.
- [45] Logan, S.E., "A Laser Velocimeter Measurement of Reynolds Stress and Turbulence in Dilute Polymer Solutions," Ph.D. Thesis, California Institute of Technology, 1972.
- [46] Freeman, A.R., "Laser Anemometer Measurements in the Recirculating Region Downstream of a Sudden Pipe Expansion," In: Proceedings of the LDA-Symposium Copenhagen, pp. 704-709, 1975.
- [47] Drewry, J.E., "Fluid Dynamic Characterization of Sudden-Expansion Ramjet Combustor Flowfields," AIAA Journal Vol. 16, No. 4, pp. 313-319, April, 1978.
- [48] Kangovi, S., and Page, R.H., "Subsonic Turbulent Flow Past a Downstream Facing Annular Step," ASME Journal of Fluids Engineering, Vol. 101, pp. 230-236, June, 1979.
- [49] Bradshaw, P., and Wong, F.Y.F., "The Reattachment and Relaxation of a Turbulent Shear Layer," Journal of Fluid Mechanics, Vol. 52, pt. 1, pp. 113-135, 14 March, 1972.
- [50] Restivo, A., and Whitelaw, J.H., "Turbulence Characteristics of the Flow Downstream of a Symmetric, Plane Sudden Expansion," ASME Journal of Fluids Engineering, Vol. 100, pp. 308-310, September, 1978.
- [51] Smyth, R., "Experimental Study of Turbulence in Plane Separated Flows," In: Proceedings of the ISL/AGARD Workshop on Laser Anemometry, pp. 233-244, 5-7 May, 1976.

APPENDIX

Derivation of the Mean Velocity and Turbulence Parameter Equations

The radiation scattered from a particle passing through the common intersection of two incident coherent beams from the same laser source can be mixed on a photodetector to yield a beating or Doppler frequency which is directly proportional to a component of the velocity of the scattering particle. If the two beams have an initial wavelength λ_0 in the directions \hat{e}_1 and \hat{e}_2 , and the forward beam is upshifted by a known frequency, f_s , the collected radiation will heterodyne with the beat frequency f given by

$$f = \frac{n\vec{V}}{\lambda_0} \cdot (\hat{e}_1 - \hat{e}_2) + f_s, \quad (A1)$$

where \vec{V} is the velocity of the scattering particles and n is the refractive index of the medium. The dot product $\vec{V} \cdot (\hat{e}_1 - \hat{e}_2)$ defines the velocity component in the plane of the intersecting beams and in the \hat{e}_n direction (see Figure A-1). The frequency, f , is independent of the scattering direction.

From vector algebra,

$$\hat{e}_1 - \hat{e}_2 = 2 \sin\left(\frac{\theta}{2}\right) \hat{e}_n \quad (A2)$$

where θ is the angle between the incident beams.

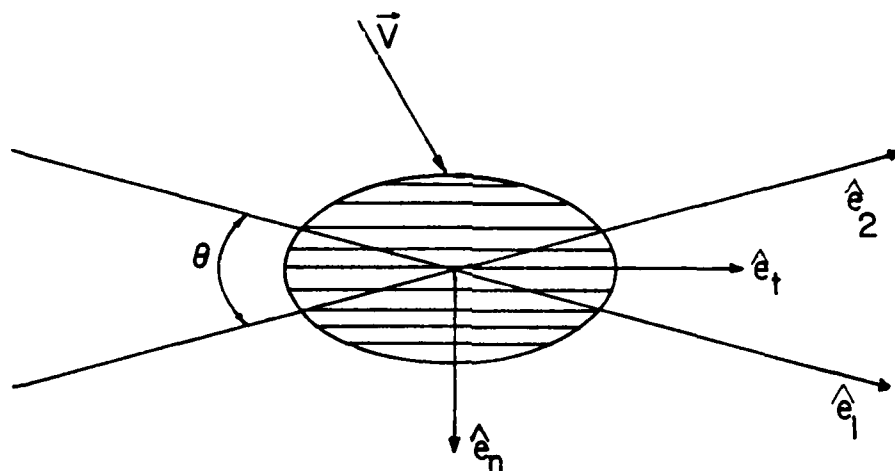


Figure A-1. Probe volume geometry.

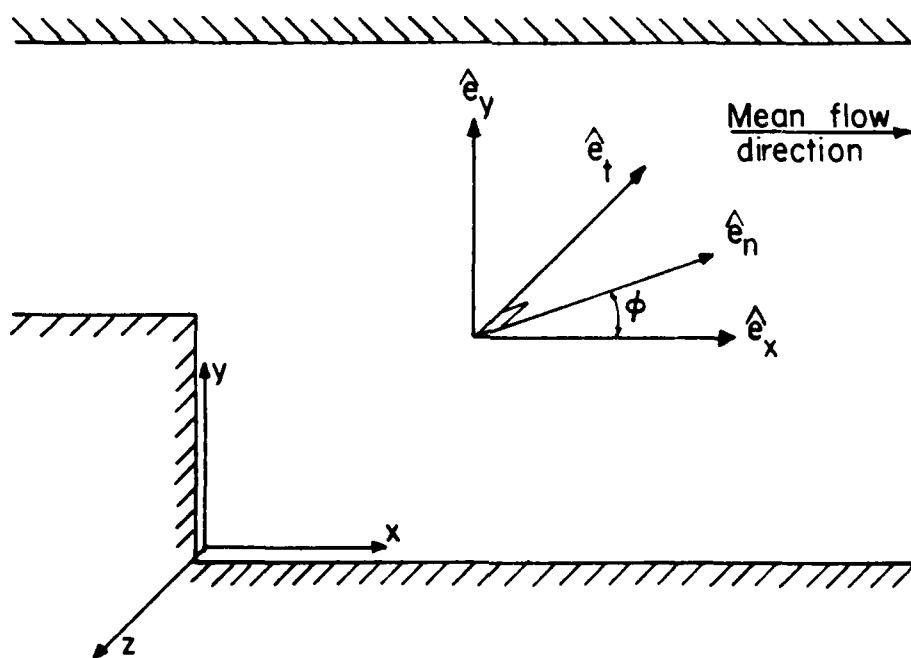


Figure A-2. Flow system geometry.

For convenience the LDV system can be aligned so that the (x,y)-laboratory coordinates are in the plane perpendicular to the \hat{e}_t direction (see Figure A-1). Then

$$\hat{e}_n = \cos \phi \hat{e}_x + \sin \phi \hat{e}_y , \quad (A3)$$

where ϕ is the angle between the \hat{e}_n direction and x-axis as illustrated in Figure A-2.

To support a turbulent flow model, let

$$\vec{V} = (\bar{u} + u')\hat{e}_x + (\bar{v} + v')\hat{e}_y + (\bar{w} + w')\hat{e}_z , \quad \text{and} \quad (A4)$$

$$f = \bar{f} + f' \quad (A5)$$

where the bar indicates a time average quantity and the prime indicates an instantaneous fluctuation above or below the time average. Substituting Equation (A3) into Equation (A2) yields

$$\hat{e}_1 - \hat{e}_2 = 2 \sin\left(\frac{\theta}{2}\right) \cos \phi \hat{e}_x + 2 \sin\left(\frac{\theta}{2}\right) \sin \phi \hat{e}_y . \quad (A6)$$

Substituting Equations (A4), (A5), and (A6) into Equation (A1) yields

$$\bar{f} + f' = A[(\bar{u} + u') \cos \phi + (\bar{v} + v') \sin \phi] + f_s , \quad (A7)$$

where

$$A \equiv \frac{2n}{\lambda_0} \sin\left(\frac{\theta}{2}\right) . \quad (A8)$$

Time averaging Equation (A7) yields

$$\bar{f} - f_s = A[\bar{u} \cos \phi + \bar{v} \sin \phi] . \quad (A9)$$

Squaring both sides of Equation (A7), time averaging, and using Equation (A9) to eliminate \bar{f}^2 yields

$$\overline{f'^2} = A^2[\overline{u'^2} \cos^2 \phi + 2\overline{u'v'} \cos \phi \sin \phi + \overline{v'^2} \sin^2 \phi] . \quad (A10)$$

Equations (A9) and (A10) represent two equations in five unknowns, namely, \bar{u} , \bar{v} , $\overline{u'^2}$, $\overline{v'^2}$, and $\overline{u'v'}$. Logan [44,45] pointed out that by measuring the time average Doppler frequency, \bar{f} , and its variance, $\overline{f'^2}$, at three different angles, a set of measurements for the five unknowns could be obtained. Measuring \bar{f} and $\overline{f'^2}$ at $\phi = 0^\circ, +30^\circ, -30^\circ$ yields

$$\bar{u} = [(\bar{f})_{\phi=0} - f_s]/A , \quad (A11)$$

$$\overline{u'^2} = (\overline{f'^2})_{\phi=0}/A^2 , \quad (A12)$$

$$\bar{v} = [(\bar{f})_{\phi=+30} - (\bar{f})_{\phi=-30}]/A , \quad (A13)$$

$$\overline{v'^2} = [2(\overline{f'^2})_{\phi=+30} + 2(\overline{f'^2})_{\phi=-30} - 3(\overline{f'^2})_{\phi=0}]/A^2 , \quad (A14)$$

[44] Logan, S.E., "A Laser Velocimeter for Reynolds Stress and Other Turbulence Measurements," AIAA Journal, Vol. 10, No. 7, pp. 933-935, 1972.

[45] Logan, S.E., "A Laser Velocimeter Measurement of Reynolds Stress and Turbulence in Dilute Polymer Solutions," Ph.D. Thesis, California Institute of Technology, 1972.

$$\overline{u'v'} = [(\overline{f'^2})_{\phi = +30} - (\overline{f'^2})_{\phi = -30}] / A^2 \sqrt{3} , \quad (\text{A15})$$

and

$$\overline{u} = [(\overline{f})_{\phi = +30} + (\overline{f})_{\phi = -30} - 2f_s] / A\sqrt{3} . \quad (\text{A16})$$

Notice that Equations (A11) and (A16) are redundant for the determination of \overline{u} . If there is no bias error in the measurement then Equations (A11) and (A16) yield the same result [37].

If the sampling rate of the Doppler frequency f is at even time increments, then

$$\overline{f} = \frac{1}{n} \sum_{i=1}^n f_i . \quad (\text{A17})$$

The fringe spacing, F_R , is inversely related to A , that is,

$$F_R = \frac{\lambda_0}{2n \sin(\frac{\theta}{2})} = \frac{1}{A} \quad (\text{A18})$$

Substitution of Equations (A17) and (A18) into Equation (A11) yields

$$\overline{u} = \left[\frac{1}{n} \sum_{i=1}^n (f_i)_{\phi=0} - f_s \right] (F_R) . \quad (\text{A19})$$

But the velocity is related to the frequency and fringe spacing by

$$V = (f - f_s) F_R . \quad (\text{A20})$$

Therefore, substitution of Equation (A20) into Equation (A19) yields the expression for \bar{u} , that is,

$$\bar{u} = \frac{1}{n} \sum_{i=1}^n (V_i)_{\phi=0} . \quad (A21)$$

Substitution of Equations (A17), (A18), and (A20) into Equation (A13) yields the expression for \bar{v} ,

$$\bar{v} = (\bar{V})_{\phi=30} - (\bar{V})_{\phi=-30} . \quad (A22)$$

Substitution of Equations (A5), (A17), and (A18) into Equation (A12) yields

$$\overline{u'^2} = \left\{ \frac{1}{n} \sum_{i=1}^n [(f_i)_{\phi=0} - \frac{1}{n} \sum_{i=1}^n (f_i)_{\phi=0}]^2 \right\} (F_R)^2 . \quad (A23)$$

Substitution of Equations (A19) and (A20) into Equation (A23) yields

$$\overline{u'^2} = \frac{1}{n} \sum_{i=1}^n [(V_i)_{\phi=0} - (\bar{V})_{\phi=0}]^2 . \quad (A24)$$

Taking the square root of both sides of Equation (A24) yields the expression for $\sqrt{\overline{u'^2}}$, that is,

$$\sqrt{\overline{u'^2}} = \frac{1}{n} \sum_{i=1}^n [(V_i)_{\phi=0} - (\bar{V})_{\phi=0}]^2{}^{1/2} . \quad (A25)$$

Substitution of Equations (A5), (A7), and (A18) into Equation (A14) yields

$$\begin{aligned} \overline{v'^2} = & \left[\left\{ \frac{2}{n} \sum_{i=1}^n [(f_i)_{\phi=+30} - \frac{1}{n} \sum_{i=1}^n (f_i)_{\phi=+30}]^2 \right\} \right. \\ & + \left\{ \frac{2}{n} \sum_{i=1}^n [(f_i)_{\phi=+30} - \frac{1}{n} \sum_{i=1}^n (f_i)_{\phi=-30}]^2 \right\} \\ & \left. - \left\{ \frac{3}{n} \sum_{i=1}^n [(f_i)_{\phi=0} - \frac{1}{n} \sum_{i=1}^n (f_i)_{\phi=0}]^2 \right\} \right] (F_R)^2. \quad (A26) \end{aligned}$$

From Equations (A23) and (A20)

$$(\overline{v'^2})_{\phi} = \frac{1}{n} \sum_{i=1}^n [(v_i)_{\phi} - (\bar{v})_{\phi}]^2 = \frac{1}{n} \sum_{i=1}^n [(f_i)_{\phi} - (\bar{f})_{\phi}]^2 (F_R). \quad (A27)$$

Substitution of Equation (A27) into Equation (A26) and taking the square root of both sides yields the expression for $\sqrt{\overline{v'^2}}$, that is

$$\sqrt{\overline{v'^2}} = [2(\overline{v'^2})_{\phi=+30} + 2(\overline{v'^2})_{\phi=-30} - 3(\overline{v'^2})_{\phi=0}]^{1/2}. \quad (A28)$$

Substitution of Equations (A5), (A7), (A18), and (A27) into Equation (A15) yields the expression for $\overline{u'v'}$, that is,

$$\overline{u'v'} = [(\overline{v'^2})_{\phi=+30} - (\overline{v'^2})_{\phi=-30}]/\sqrt{3}. \quad (A29)$$